DISSERTATION / DOCTORAL THESIS

Titel der Dissertation /Title of the Doctoral Thesis

„(Conductive) Imprinted Polymers for Sensing Volatile Disease Biomarkers"

verfasst von / submitted by

Adriana Katharina Feldner, BSc MSc

angestrebter akademischer Grad / in partial fulfilment of the requirements for the degree of

Doktorin der Naturwissenschaften (Dr. rer. nat.)

Wien, 2024/ Vienna 2024

Acknowledgements

Abbreviations

μm	Micrometre
AA	Acrylamide
AFM	Atomic force microscope
AIBN	Azobisisobutyronitrile
BPA	Bisphenol A
cMIP	Conductive molecularly imprinted polymer
cNIP	Conductive non-imprinted polymer
DABCO	1,4-Diazabicyclo[2.2.2]octane
DMAA	N,N-Dimethylacrylamide
DMSO	Dimethyl sulfoxide
DPDI	4,4'-Diphenylmethane diisocyanate
DPM	Diphenylmethane
EDX	Energy-dispersive X-ray
EGDMA	Ethylene glycol dimethacrylate
GC-MS	Gas chromatography-mass spectrometry
Hz	Hertz
IDE	Interdigitated electrode
IUPAC	International Union of Pure and Applied Chemistry
MAA	Methacrylic acid
MIP	Molecularly imprinted polymer
MOX	Metal oxide
NH_3	Ammonia
NIP	Non-imprinted polymer
nm	Nanometre
P3HT	Poly(3-hexylthiophen-2,5-diyl)
PG	Phloroglucinol
ppb	Parts per billion
ppm	Parts per million
PU	Polyurethane

PVD	Physical vapour deposition
QCM	Quartz crystal microbalance
QNM	Quantitative nanomechanics
ROS	Reactive oxygen species
rpm	Revolutions per minute
SAW	Surface acoustic wave
SEM	Scanning electron microscope
THF	Tetrahydrofuran
UV	Ultraviolet
VOC	Volatile organic compound

Table of Contents

1. Introduction

Molecularly imprinted polymers (MIPs) are synthetic materials that contain imprints of certain analytes. During polymerisation functional monomers interact with a template. A crosslinker promotes the formation of a stable polymer matrix. After complete polymerisation and template removal, binding sites that are complementary to the template remain in the material. In their function MIPs mimic bioreceptors and are often referred to as plastic antibodies. The synthetic materials present several advantages over biomolecules, such as higher stability in various media and at non-physiological conditions. Additionally, they are cheaper to produce. [1]

MIPs are popular receptors on sensors. Often they are implemented onto quartz crystal microbalance (QCM) which is a mass-sensitive sensor. [2–5] This type of sensor consists of a thin quartz plate with gold electrodes on both sides. Due to the piezoelectric properties of quartz, the material between the electrodes oscillates at its resonance frequency when alternating voltage is applied. Mass deposition on the electrodes induces a decrease of the frequency. [6]

Polymer-based chemiresistors are resistive sensors that detect the target analyte through conductive polymer films. They are mainly used for detecting gaseous compounds. The films swell upon analyte adsorption which changes the electrical resistance of the material. The swelling is reversible which allows for reusing of the sensors. [7] In comparison to QCM, chemiresistors require less complex measuring electronics and can easily be measured simultaneously. As stated above, chemiresistors require conductive polymers as sensing layers. Conventional MIPs are often based on acrylic polymers, because they offer a wide range of different functionalities. However, those materials are electric insulators. In order to prepare conductive MIPs (cMIPs) one can either electropolymerise suitable monomers, or add additives to the non-conductive polymer. [8]

Diseases often affect the metabolism, which leads to the production of specific compounds, so-called biomarkers. Among others, some biomarkers are emitted via the exhaled air. In this case they are small volatile organic compounds (VOCs). Monitoring breath biomarkers offers a valuable tool for non-invasive early detection of diseases. [9] Breath analysis as diagnostic tool is already in use for certain diseases: for example, ^{13}C-urea for helicobacter pylori or nitric oxides for asthma. A similar application is the ethanol breath test. [10]

Philipps et al. identified a number of biomarkers in the exhaled breath of breast cancer patients. [11] Even though breath analysis is a growing field in research, most applications lack simple and portable test devices.

The aim of this thesis is to develop sensing devices for several breath biomarkers related to breast cancer. More precisely, the analytes are 2-propanol, heptanal and acetophenone. For this task MIPs are used as sensing layers on both QCM and chemiresistors. Based on the functional groups of the templates, suitable monomers are chosen; MIPs are developed and optimised. For the use on chemiresistors, the MIPs must be conductive. Within this project, this is achieved by blending the non-conductive MIPs with a conductive polymer. The ability of the non-conductive MIPs and their respective conductive blends to rebind the target analyte in comparison to non-imprinted polymers (NIPs) is assessed by QCM. The performance of the blends is also tested in chemiresistor measurements. Furthermore, the thesis comprises selectivity and surface characterisation studies. The developed (c)MIP sensors could serve as a steppingstone towards breath analysis for early detection of breast cancer. Alternatively, the sensors could be used for VOC monitoring.

2. Theoretical Background

2.1. Sensors

According to IUPAC definition, a chemical sensor is a "*device that transforms chemical information ranging from the concentration of a specific sample component to total composition analysis, into an analytically useful signal. The chemical information, mentioned above, may originate from a chemical reaction of the analyte or from a physical property of the system investigated*" [12].

Generally, sensors are small, affordable, portable, and do not require a large laboratory. Ideally, a sensor should demonstrate high selectivity, sensitivity, stability, and reproducibility. Every sensor consists of two primary components: a receptor and a transducer. The receptor is responsible for selective recognition and binding of the target analyte. The transducer converts the information about the binding event into a measurable signal. [12] Figure 1 shows a schematic of a typical chemical sensor. Sensors are classified according to their type of transduction. Typical transducers include optical, electrochemical, or mass-sensitive methods [13].
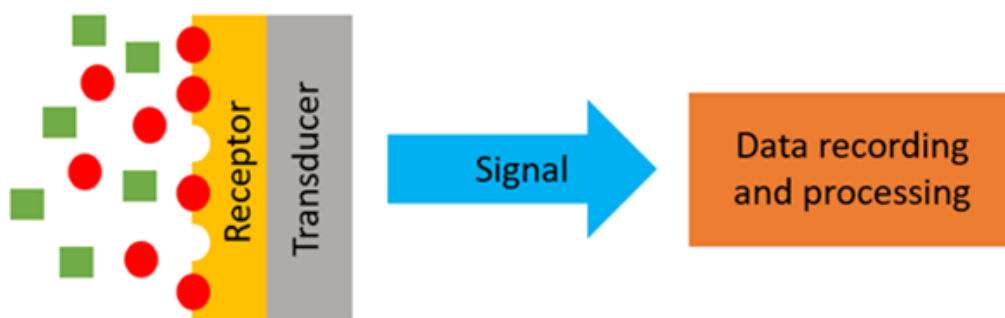
Figure 1: Schematic of a chemical sensor. The receptor selectively binds the target analyte (red circles). Other compounds (green squares) do not interact with the receptor. The transducer is responsible for converting the signal of the binding event in information that can be read out via the data recording and processing unit. [8]

2.1.1. Quartz Crystal Microbalance

Mass-sensitive sensors are acoustic devices that offer the advantage of label-free detection. Unlike other transduction methods, these sensors do not require any additional modification/derivatisation to generate a sensor signal. Every analyte has mass, making it a universal physical property to detect; this distinguishes it from other options, such as optical and electrochemical properties. If a suitable receptor

is available, mass-sensitive devices can detect a wide range of different analytes in both gaseous and liquid media, making them cost- and time-efficient. [14]

Most acoustic devices rely on the piezoelectric effect, which was discovered in 1880 by Jacques and Pierre Curie. The brothers found that crystals without inversion centre generate voltage when being deformed by external force. The opposite effect or "inverse piezoelectric effect" occurs when voltage is applied causing deformation of the material. For sensing purposes, several piezoelectric materials are available. However, quartz is the most popular one, because of its abundance and low price. [6]

Applying alternating voltage to piezoelectric materials results in mechanical oscillation, with the specific type of oscillation being determined by both the material and the cutting angle. [6] These oscillations are classified as either bulk acoustic waves, which travel through the material, or surface acoustic waves, which propagate along the surface. Analyte adsorption to the sensor surface affects wave parameters, such as resonance frequency or acoustic wave velocity. [15]

The QCM is a well-known piezoelectric sensor and a representative of bulk acoustic devices. Its advantages include straightforward design, easy availability, and low cost due to the abundance of quartz. Additionally, QCMs can operate in both gaseous and liquid phase. The device consists of a thin AT-cut quartz plate with metal electrodes on both sides, as shown in Figure 2. When an alternating voltage is applied to the electrodes, the quartz oscillates in thickness shear mode. The typical resonance frequencies of QCMs are in the range of 2-20 MHz with higher resonance frequencies resulting in higher sensitivity. Thinner quartz substrates reach higher resonance frequencies and sensitivities, up to a point. Beyond that, the substrate becomes too fragile to be mechanically stable and can easily break during handling and measurements. [15]

Figure 2: Schematic of a QCM sensor. A thin quartz plate is sandwiched between two metal electrodes.

In 1959 Günther Sauerbrey described the proportionality between the change in frequency and the mass adsorbed on the surface of a piezoelectric sensor. [16] This relationship, which is stated in Equation 1, allows one to use acoustic resonators for developing mass-sensitive sensors.

Equation 1: The Sauerbrey equation [16]:

$$\Delta f = -\frac{2f_0^2}{A\sqrt{\rho\mu}}\Delta m$$

Δf … frequency change

f₀ … fundamental frequency

A … active area

ρ … density of the piezoelectric material

μ … shear modulus

From the Sauerbrey equation, one can conclude that adsorbed mass leads to a decrease of the resonance frequency. Figure 3 schematically shows the working principle of a QCM sensor. When the analyte is adsorbed on the sensor surface, the oscillation decreases until it reaches a stable frequency again.
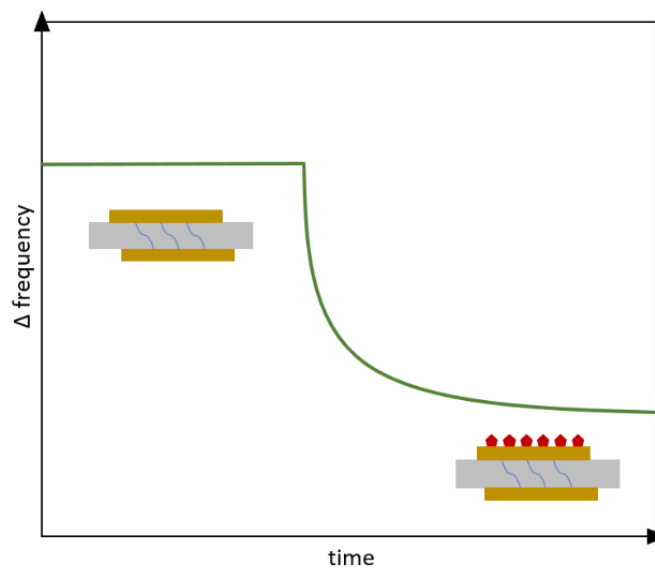
Figure 3: Working principle of a QCM sensor. The red shapes represent adsorbed analyte which causes a frequency decrease.

The Sauerbrey equation assumes rigid and indefinitely thin films on the electrode. It also excludes all mechanical interaction with the medium. Consequently, it is only valid in the gas phase. In liquids, parameters such as viscosity and density of the surrounding medium must be considered. To describe the change in oscillation frequency in liquids, Kanazawa and Gordon developed Equation 2. [17]

Equation 2: The equation by Kanazawa and Gordon [17]:

$$\Delta f = -f_0^{3/2} \left(\eta_L \rho_L \big/ \pi \mu_Q \rho_Q \right)^{1/2}$$

Δf … frequency change

f_0 … fundamental frequency of the dry crystal

η_L … elastic modulus of the liquid

ρ_L … density of the liquid

η_Q … elastic modulus of quartz

ρ_Q … density of quartz

The QCM is also affected by changes in the viscosity or density of the surrounding medium, which may seem like a disadvantage at first. However, this property can be utilised for measurement, resulting in a method called QCM with dissipation monitoring (QCM-D). This technique allows for both the determination of the mass and viscoelastic properties of an adsorbed layer in real-time. [18]

In addition to viscoelasticity, temperature changes have a significant impact on the frequency of QCM sensors. To ensure reliable signals in non-thermostated conditions, one can use sensors with an additional reference electrode on the same quartz substrate. By employing a dual electrode setup, signals resulting from variations, such as temperature, viscosity and unspecific adsorption are cancelled out by subtracting the reference from the measurement signal. [19] Figure 4 schematically depicts this principle.
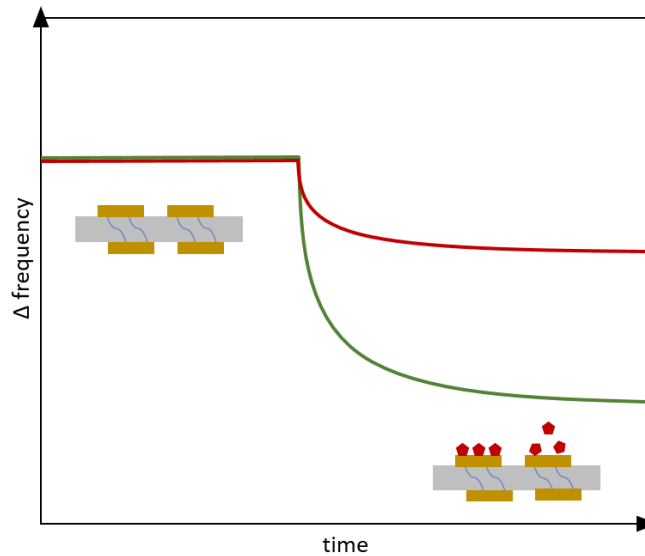
Figure 4: Schematic of a QCM measurement with dual electrode design. The frequency of the measurement electrode (green) decreases due to analyte adsorption to the sensing material. The frequency shift on the reference electrode (red) is smaller and caused by changes in the measuring cell and unspecific adsorption.

2.1.2. Chemiresistor

Chemiresistors consist of two interdigitated electrodes (IDEs) that are separated by a narrow gap. Figure 5 provides a schematic of a sensor. The electrodes are coated with the conducting receptor material. This connects the separate electrodes and allows for conductivity between them. The microelectrodes consist of thin platinum or gold films on a non-conductive support. The gap in between ranges from 1.5 µm to 100 µm. It is easier to bridge narrower gaps with a receptor film, which increases sensitivity. [20]

The electrical resistance between the electrodes changes upon exposure to gaseous analytes. The analyte and the sensing material dictate the signal magnitude. Metal oxides (MOX) are a popular sensing material for resistive gas sensors. MOX sensors are usually portable, cost effective in production, and exhibit good sensitivity. However, they are not particularly selective and require high operating temperatures, which equals to high power consumption. Alternatives to MOX sensors are resistive sensors based on conductive polymers. Chemiresistors coated with a conductive polymer layer operate at room temperature and often increase selectivity because of the affinity of the analyte towards a certain polymer. Gas adsorption leads to chain perturbations in the polymer, which affects the conductivity. [7]
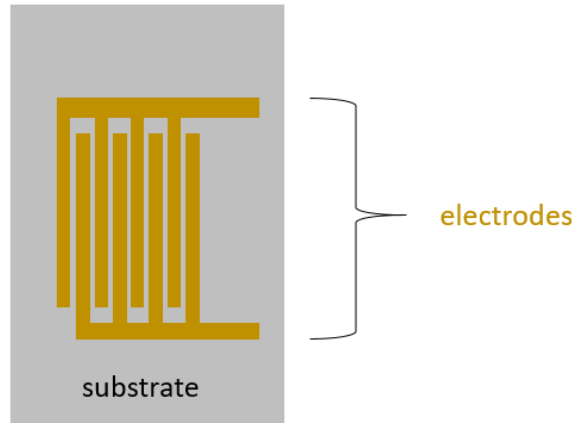
Figure 6 shows the chemiresistor sensing platform used in this project, which is based on a voltage divider. It comprises two sets of IDEs. Both are coated with the same sensing material. One of the electrodes is then sealed and does not interact with the analyte. The other electrode is exposed to the analyte and changes its electrical properties. This two-electrode set-up limits sensitivity of the device to drift and degradation effects. [21] The sensor response is based on the principle of a voltage divider and depends on the resistances of both electrodes and is given in Equation 3. [7]

Equation 3: Sensor response of the chemiresistor.

$$Sensor\ response\ [\%] = \frac{R_{ref}}{R_{ref} + R_{meas}} * 100$$

R_{ref}...electric resistance of the sealed reference electrode

R_{meas}... electric resistance of the measuring electrode

The sensor is equipped with a USB connector which supplies the input voltage. Simultaneously, it is used to read out the signal. To operate the sensor measurement and read out the data, any device with a USB port can be used. This allows for simplifying the measurement set-up and miniaturisation of the device. Furthermore, it helps reducing expenses and power consumption for additional equipment. Another

advantage is easy integration in a sensor array which allows for simultaneous measurements of several sensors, which decreases measuring time and increases comparability. [21]
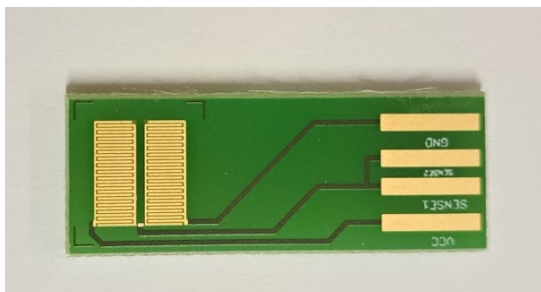
Figure 6: One of the chemiresistors used in this project. On the left side the two IDEs can be seen. On the other end of the sensor the USB connector is located.

Often those sensors are coated with unmodified conductive polymers, which limit their selectivity. An approach to increase selectivity is the use of cMIPs. Since most MIPs are made from acrylic or vinylic monomers and thus are electric insulators, strategies to make them conductive are necessary. [8] Upon exposure to the gaseous analyte, the polymer layers swell due to analyte adsorption. This changes their electrical properties, which can be detected as a shift in the electrical resistance. [22]

2.2.   Molecular Imprinting

Molecular imprinting is a synthesis strategy used to prepare synthetic materials with binding sites for specific analytes. Figure 7 depicts the process. Functional monomers are polymerised around a template. Co-polymerisation with a crosslinker ensures formation of a stable polymer network. After template removal, the material contains cavities, which are complementary to the template in size, shape, and functional groups. Thus, the analyte can selectively rebind to the material. [23] Historically, the first MIPs were silica materials that showed higher affinity towards the solvent in which they had been prepared. [24,25] In recent years, MIP research has mostly been based on organic polymers prepared by radical polymerisation. [26]
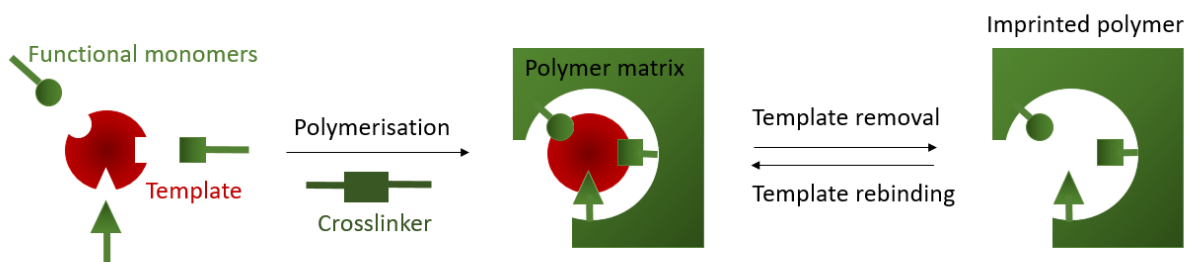
Figure 7: The principle of molecular imprinting. Functional monomers and crosslinker are polymerised around a template. After curing, the template is removed and leaves behind cavities in the material in which the analyte can selectively rebind.

The choice of functional monomer plays a crucial role in molecular imprinting. The monomers are chosen in a way to provide high affinity towards the template. The interaction is usually based on non-covalent bonds formed between the functional groups of the monomer and the template. The relatively low binding strength allows for comparably easy template removal and reusability of the MIPs. The less common covalent imprinting requires an additional synthesis step to cleave the covalent bonds between monomer and template. [27]

MIPs are designed to mimic the specific recognition abilities of biomolecules, such as the antibody-antigen interaction. However, due to their synthetic nature, they have certain advantages where biomolecules fail. For example, MIPs are more stable in harsher conditions such as varying pH or temperature. [1] They can easily be stored and often reused. MIP production is relatively cheap compared to, for example, the production of antibodies and can be adjusted to the respective purposes. [23]

MIPs exist in different shapes which depend on the method of synthesis. Thin films are produced by coating the gel-like oligomer solution onto a substrate before it is fully polymerised [28] or by electropolymerisation [29]. Particles can be obtained by preparing a bulk polymer and grinding it. [30] Alternatively, precipitation polymerisation [31] or Pickering emulsion polymerisation [32] result in usually round particles. A special case is the preparation of so-called nanoMIPs (short for molecularly imprinted nanobodies). They are obtained by solid-phase synthesis, contain only one binding site, and are separated according to their affinity to the template. This results in very specific binding to the target analyte. Because of these characteristics, nanoMIPs are often referred to as artificial antibodies. [33]

As diverse as the morphologies of the MIPs, are the analytes they can bind. Templates range from ions [34–36] and small molecules [28,37,38] over proteins [39–41] to whole cells [42,43] and organisms such as bacteria [44–46]. For larger templates surface imprinting is the method of choice. Here the templates are not completely immersed in the polymer, which facilitates template extraction and rebinding. Typically, the template is immobilised on a stamp and pressed into the oligomer layer before curing. [47] Proteins are often imprinted via epitope imprinting where only a small, characteristic sequence serves as the template instead of the whole molecule. [48]

2.2.1. Small Molecule Imprinting

Bulk imprinting is used for small target molecules. Hence, this is the method that was applied in this project and will be most extensively explored. Here the template is directly added to the monomer/crosslinker mixture before polymerisation. The template is not only present on the surface of the polymer, but also enclosed in the bulk of the material. Due to its small size, it can be extracted through pores in the polymer. [47] Porogens are used to enhance binding site accessibility and binding capacity by making the material more porous. [49] There are two strategies in bulk imprinting of small molecules: One is the so-called porogen imprinting approach. Here the template is additionally used as the solvent and porogen in polymer synthesis, which means that it is present in huge excess. The second approach is template imprinting, where the solvent differs from the template. [22]

The properties of the MIP depend on several factors such as the concentrations of the components and their interactions with one another. This is somewhat limited in porogen imprinting, since here the template itself is the solvent, hence removing one variable. Solvents are usually chosen for their ability to dissolve all components in the mixture. However, in the case of template imprinting this can result in MIPs which ultimately respond more strongly to the solvent in which they were prepared than to the intended template. [50] In certain cases, high amounts of template can impede the polymerisation leading to weaker responses. [38,51] Even though MIPs are usually prepared with a high degree of crosslinking, examples of sensitive MIPs prepared from dissolved linear polymers exist. [52] Those polymers tend to preferentially bind the solvent they were last dissolved in. [53] The polymer is already fully formed before it gets into contact with the solvent. Then it arranges itself around the solvent molecules in the most favourable way. This arrangement of the polymer chains is retained even when the solvent has evaporated. [54] The smaller the molecules are, the harder it is to achieve good selectivity, since the imprinting effect is proportional to the molar volume of the template. [55] Some studies suggest that the

imprinting effect is larger when the polymer is less soluble in the porogen solvent. [56] Affinity and surface area are proportional to solubility. [57] Since there is a large number of parameters in optimisation of MIP synthesis, it is hard to compare template and porogen imprinting directly. [58] So far, no general optimum conditions for porogen imprinting have been established. It is more likely to improve selectivity and sensitivity in template imprinting. However, porogen imprinting seems to be the better option for imprinting common solvents. With porogen imprinting, one can reach higher binding capacities. [22]

In template imprinting the template concentration is much lower, which also reduces the amount of possible binding sites. However, it has been proven that the ratio of template to monomer has an impact on the success of imprinting. In most cases, researchers came to the conclusion that best results can be obtained with a ratio of four molecules of the monomer for each molecule of the template. [59–62] In studies about crosslinking ratio the polymer with the highest crosslinking degree showed the best results. In fact, a ratio of 3:20 monomer to crosslinker was used. [63] The most common ratio of template, monomer and crosslinker is 1:4:20. [64,65] Even in the case of template imprinting, porosity of the material may increase the performance. [66] Polymer swelling can not only occur from adsorption of the template, but also from adsorbing the solvent in which it was prepared, which suggests unintentional porogen imprinting. [67] This phenomenon can be used in a combined approach of simultaneous template and porogen imprinting for MIPs with affinity for two molecules at the same time. [22]

MIP synthesis for small molecules is challenging. First, because the smaller the template is, the fewer possibilities to interact with the monomer there are. This reduces the overall affinity and selectivity of the material towards the template. The monomers may interact with any molecule present in the polymerisation mixture. In the optimum case, this means the energetically most favourable interaction with the template. However, small molecules are often volatile, which precludes intermolecular interactions. This reduces the interaction of the analyte with the monomers, which consequently may favour dimerisation over binding to VOCs. [22] Compared to liquid phase measurements, gas phase sensors may be more prone to unspecific binding. [68] Due to chemical and macroscopic variation in polymers, general models of the gas adsorption in MIPs are difficult to determine. [22] In gas phase measurements, there is naturally no solvent present in the binding site; it has not yet been determined how this affects the binding ability. [22] Especially in gas phase applications, humidity may be a challenge. Approaches to solve this include adding pyrolysed lotus leaves to the polymerisation mixture. The nanostructures of the leaves increase the hydrophobicity of the polymer. [69] A similar effect can be achieved by using nanoparticles instead of MIP films. [70]

Nevertheless, in some cases template-imprinted MIPs can be sufficiently selective to make even discriminating gaseous enantiomers possible. [71] Sensitivity can be low; this issue has been addressed with various approaches. For example, it is possible to delay adding the template to the oligomer solution. [72] A similar approach comprises delayed crosslinking after dissolving the template together with a linear polymer. [73] The template does not necessarily need to be the analyte itself. Sometimes analogues can be used instead, which still leads to sufficient recognition of the actual analyte. This is especially useful when one can substitute a hazardous analyte by a less dangerous compound. [74] When directly comparing them, it is noticeable that porogen imprinting is primarily used for small templates. For larger molecules template imprinting is favoured. It appears that template imprinting results in better selectivity which might be since it is harder to prepare selective MIPs for smaller targets. In template imprinting a larger amount of monomers is available for the templates, while in porogen imprinting a high amount of template molecules compete for functional groups to interact with. This may result in a more ordered interaction in template imprinting. Porogen imprinting is useful for most general gas sensing applications. However, if high selectivity and sensitivity are desired, template imprinting may lead to better results. [22]

2.2.2. Polymerisation Strategies

Radical Polymerisation

MIPs can be synthesised using different polymerising methods. The most popular one is free radical polymerisation. Examples of polymers prepared by free radical polymerisation are polyacrylates. Polyacrylates are made from acrylic acid or its derivatives. They are among the most widely used polymers for MIPs. Figure 8 shows the reaction mechanism with the monomer MAA. The process comprises of three parts: initiation, propagation, and termination. First, polymerisation is initiated by generating a free radical. Initiators used for that task are molecules that decompose into free radicals when heated or irradiated. The radicals attack the double bonds of the monomers where they generate new radicals. In many polymerisations, initiation is the rate determining step. Propagation is the part where the actual polymerisation happens: the radicals generated during initiation attack further monomers and connect to polymer chains of various lengths. The reaction terminates when two radicals combine to a bond without forming a new radical. Abstracting hydrogen from one chain to another yielding a terminal unsaturated group in one chain or chains combining with initiator radicals also terminate the propagation. [75]
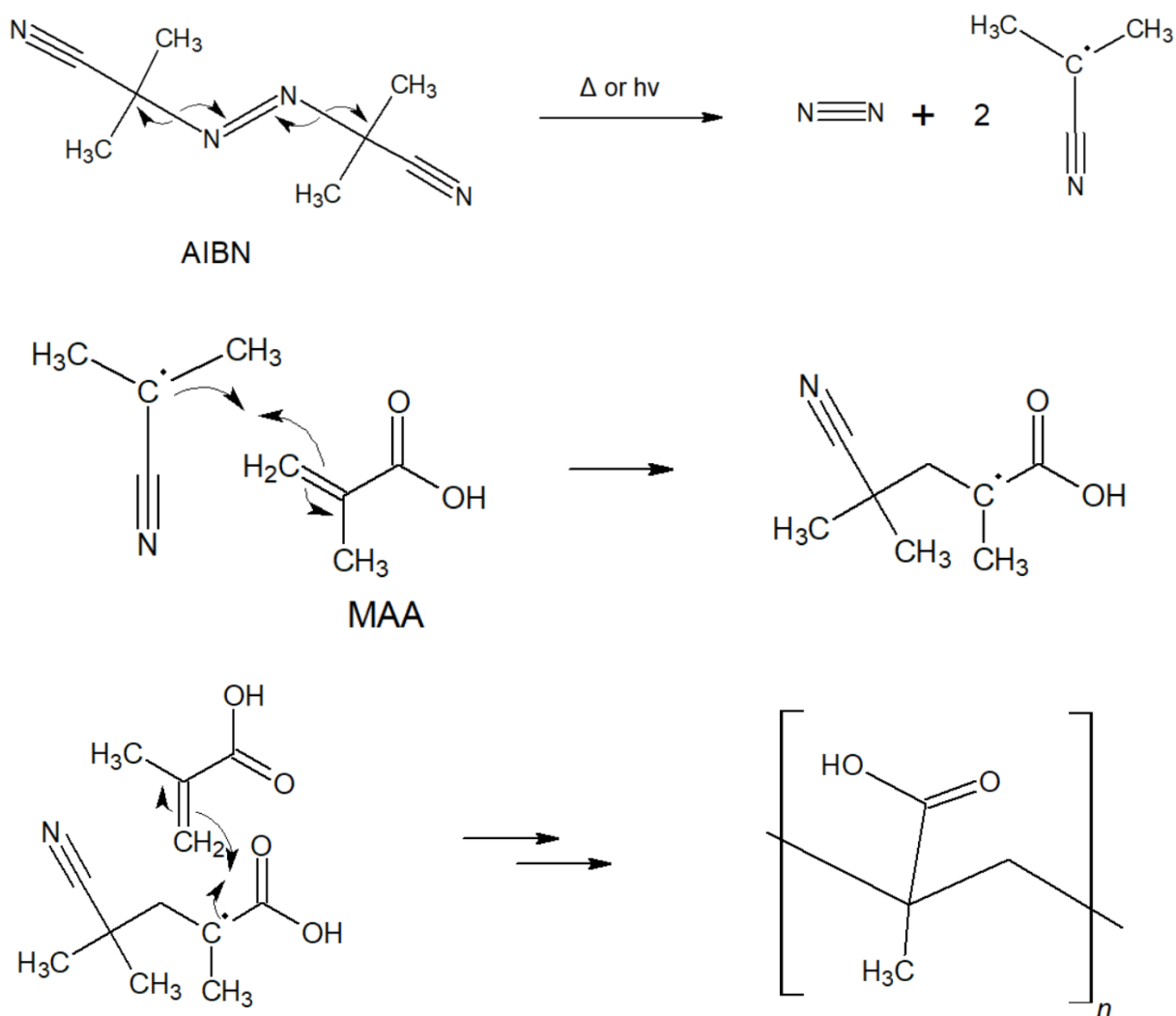
Figure 8: Free radical polymerisation shown with the monomer methacrylic acid (MAA) and the initiator azobisisobutyronitril (AIBN).

Synthesis via free radical polymerisation is relatively easy and straightforward; a wide selection of monomers is available to tailor the MIP to specific applications. The main drawback of this method is the statistical nature of the process. Chain length is neither predictable, nor controllable. This led to the development of methods to better control the chain length, such as reversible addition–fragmentation chain-transfer (RAFT) polymerisation. [75]

Polyaddition

Polyaddition is another type of polymerisation reaction. This type of polymerisation is, for instance, used for polyurethane synthesis. The characteristic urethane group forms by a reaction of an isocyanate with a hydroxyl group. The polyaddition reaction of di-isocyanates and polyols forms the polymer. Figure 9 depicts the reaction mechanism. The electron pair of the hydroxyl group attacks the carbon of the isocyanate. The hydrogen atom is moved from the hydroxyl to the nitrogen of the isocyanate. [76]
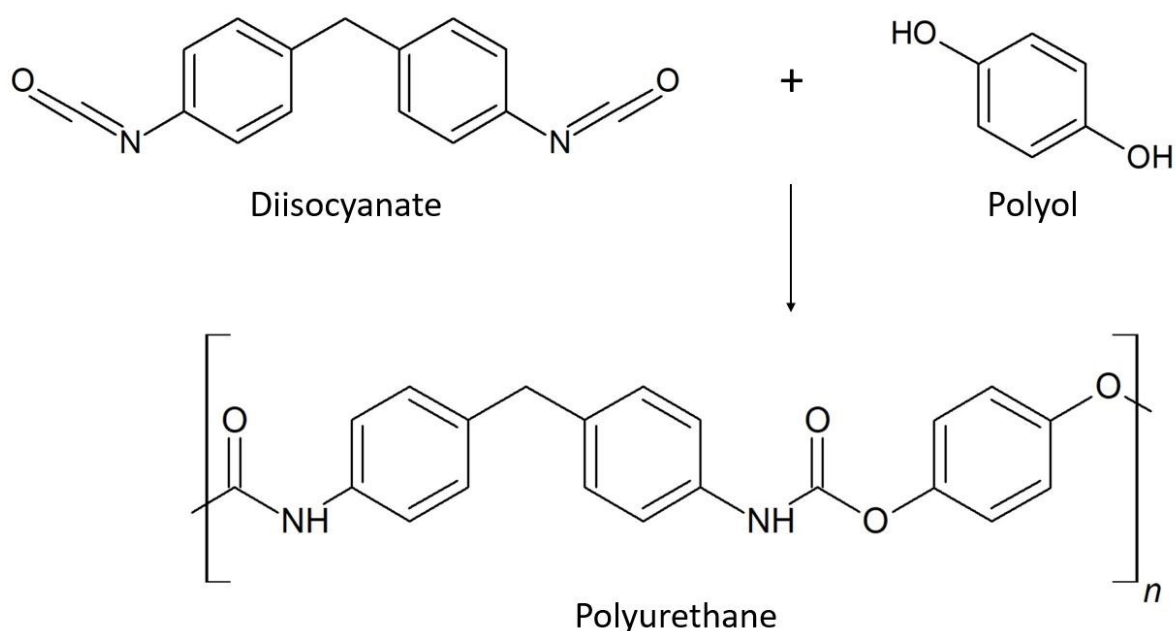
Figure 9: The polyaddition reaction forming polyurethane.

Small polyol molecules with several hydroxyl groups serve for crosslinking. Often, one uses aromatic isocyanate monomers since they are more reactive than aliphatic ones. Since the reaction is very slow at room temperature, polyaddition is often accelerated by adding catalysts. Either metal catalysts such as complexes of lead, zinc or mercury or amine compounds such as 1,4-diazabicyclo[2.2.2]octane (DABCO) and triethylenediamine (TEDA) can be used. [77] Even though using polyurethane in molecular imprinting is a recent development, there are published examples ranging from small molecules to whole

cells. [78–80] However, compared to polymers prepared by radical polymerisation, polyurethanes are rather limited in terms of variety of monomers. [75]

2.2.3. Conductive MIPs

Due to the wide choice of functional monomers, acrylate-based polymers remain among the most common MIP materials. [81] Those MIPs, however, are electric insulators by nature. This somewhat limits their applications in chemical sensing, since they are not useful in sensing strategies that require either electric conduction or monitor electrical changes in the receptor film. With emerging materials made from electrically conducting polymers [82–84] and conductive polymer nanocomposites [85,86] the possibility of integrating those in molecular imprinting and sensing has arisen. cMIPs, like their non-conductive counterparts, recognise an analyte via imprints. Additionally, they provide the advantage of a direct electrical response upon the binding event. Thus, cMIPs combine the advantages of both methods, namely selectivity for the analyte, and conductivity, which allows for using a wider range of transducers. It is possible to produce sensing devices, which are not available with non-conducting MIPs. [87] cMIPs change their electrical properties upon interaction with the analyte which allows for direct electrochemical detection. The use of cMIPs as a receptor on electrochemical sensors can, for example, reduce the influence of structurally similar compounds. Even if they interact with the binding sites, their electrochemical signal differs from the one of the target analyte. In terms of stability, cMIPs have the same advantages as non-conductive MIPs when compared to biomolecules. [88]

Synthesis Strategies to prepare cMIPs

cMIPs can be obtained by several different strategies. In general, they can be divided in polymerising conductive monomers and forming composites with conductive materials. Figure 10 shows a graphical overview over all reported strategies. Which one to choose depends on the application, the template, and the substrate.
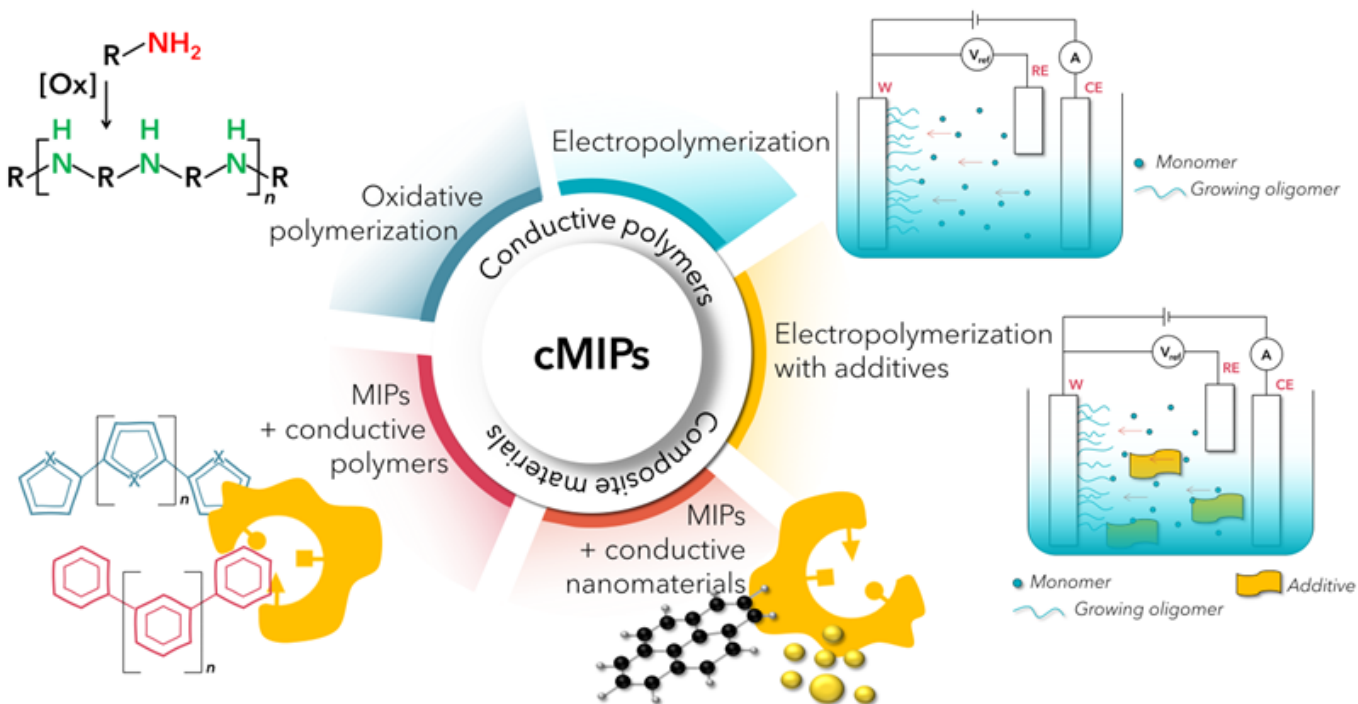
Figure 10: Ways to prepare cMIPs. [8]

Electropolymerisation is a straightforward way to obtain conductive polymers. From a solution of suitable monomers, they are electrochemically polymerised directly on the electrode surface. This usually happens by applying chronoamperometry or cyclic voltammetry. The thickness of the resulting polymer film is controlled by the amount of charge transferred during synthesis. The most frequently used monomers for electropolymerisation are pyrrole, aniline, dopamine and 3-aminophenylboronic acid. If a template is added to the solution before polymerisation, the polymer will form around it producing a cMIP. Polypyrrole is a conductive polymer and does not require additives. Polypyrrole MIPs have been developed for targets ranging from small molecules to larger species such as biomolecules or microorganisms. [89] The possibility to control the layer thickness is beneficial for good reproducibility between sensors. In contrast to other polymers, electropolymers are often synthesised in aqueous solution, which is a better environment for biomolecules than organic solvents. The main drawback of electropolymerisation is the limited number of suitable monomers and their lack of functionalities. This can be solved by synthesising new, tailored monomers for future applications. [8] Not all electropolymerised polymers are inherently conductive. Polyphenol, for example, requires additives to function as cMIP. For instance it is possible to introduce conductivity with carbon ink. [90]

Additives enhance specific properties of the polymer. For example, one can achieve an increased electrical response by combining the cMIP with 2D materials such as graphene [91,92], carbon nanotubes (CNTs) [39,93], or MXenes [94]. Nanoparticles increase the active surface area [95–97] which may lead to enhanced sensitivity and affinity towards the analyte.

A less common synthesis pathway is forming conductive polymers by chemical (oxidative) polymerisation. This approach usually relies on aniline monomers and ammonium persulfate as an oxidising agent. [98]

As mentioned above, acrylic or vinylic monomers are often the first choice for MIPs. However, the resulting polymers are insulators. To implement those polymers in electrochemical sensors, measures have to be taken to ensure sufficient electric conductivity. There are several choices. One of them is adding conductive nanomaterials, such as metal nanoparticles or carbon materials. [8]

Generally, bulk MIPs may be limited in the sense that they lead to weak signals due to impeded diffusion to the binding sites or low number of binding sites. Those problems can be circumvented by increasing porosity or incorporating nanomaterials that enhance the active surface area. The performance of sensing layers composed of cMIP blends can be further enhanced by forming more complex multi-component nanocomposites. [99]

Another possibility is combining non-conductive MIP with a (semi)conductive polymer, for instance through blends with polyaniline. [100] Blending the MIP with P3HT has proven successful in previous research for conductive imprinted gas sensors. [38] Although this seems straightforward, several crucial issues need to be considered, such as the sensitivity of the blending material toward the analyte or the measurement matrix, miscibility of the components, and degradation. It is important to ensure that the accessibility of the binding sites is not compromised by the blending. This issue can be solved by preparing nanocomposites, which have a high surface area and thus a large number of accessible binding sites. [101]

Poly(hexylthiophene) (P3HT)

P3HT is a conjugated polymer commonly used for solar cells, field-effect transistors, or light-emitting diodes, among others. Figure 11 shows the repeating unit of the polymer. Due to its ease of synthesis and good opto-electronic properties it serves as model polymer for various fundamental studies relating to charge transport and film morphology. [102]
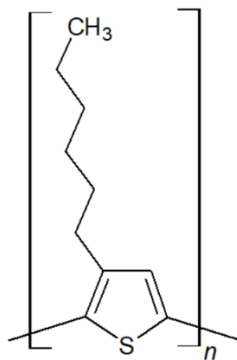
Figure 11: P3HT

3-Hexylthiophene is an unsymmetrical monomer which forms regioisomers during the early stages of polymerisation. The relative ratio of these regioisomers determines the regioregularity of the resultant polymers. [102] Compared to other conductive polymers P3HT demonstrates superior stability over time. [7]

In chemical sensing, P3HT is frequently used for ammonia (NH_3) detection. P3HT coated organic field-effect transistors reach to the lower ppm range. [103] By blending P3HT with polystyrene (PS) the sensitivity of these sensors can be increased. [104] Instead of layers, the use of P3HT nanowires as active layer has also proven useful for NH_3 sensing. [105] Upon absorption, NH_3 donates an electron lone pair to sulphur of the P3HT. [106] Recombination of electrons and holes in the p-type P3HT, increases the electric resistance. P3HT based NH_3 sensors are capable of detecting lower concentration of the gas than the human nose. [7]

P3HT has already been successfully used in MIP blends. The composites were applied to QCM and chemiresistor sensors for limonene detection. [38]

cMIP Sensors

cMIP sensors have already been developed for a wide range of analytes. These include ions, simple gas molecules, and drugs, as well as larger species, such as proteins and cells, and they are not limited to a single sensing strategy. Depending on the desired product and application, one can choose between electropolymerising suitable monomers or preparing conventional MIPs with conductive additives. In

terms of transducers, cMIPs offer a wide range of possibilities. [8] Figure 12 shows an overview of transduction methods that can be used for cMIP based sensors.
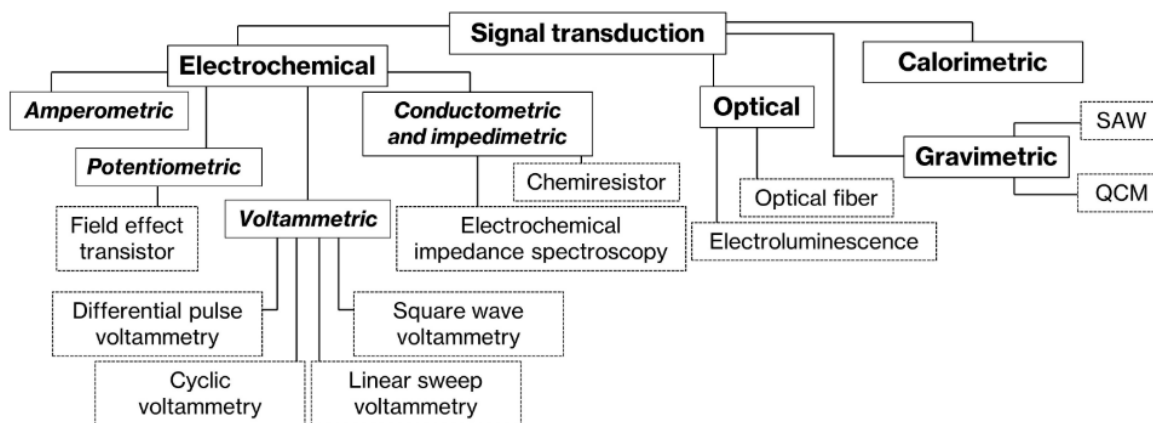

Figure 12: Possibilities of signal transduction for cMIP sensors. [8]

Non-conductive MIPs are often combined with mass-sensitive transducers such as QCM. This of course is also possible with cMIPs. [38] Surface acoustic wave (SAW) resonators, a different kind of piezoelectric sensors, can also be combined with cMIPs. [107] However, for those transducers electrically conductive polymers are not necessary. cMIPs are very useful when combined with electrochemical transducers because they enable electron transfer to the electrodes. [8]

Voltammetric methods identify the analyte via specific oxidation and reduction peaks and are therefore very selective. [108] Those methods include differential pulse voltammetry [109–111] and cyclic voltammetry [112–114], square wave voltammetry [115–117] or linear sweep voltammetry [96]. cMIP sensors with amperometric detection are less common. [118–120] Amperometric devices are a subgroup of voltammetric methods that operate at a fixed potential. The bound analyte is reduced or oxidised, which generates a current proportional to analyte concentration [121]. Other methods include potentiometric detection [99,122], electrochemical impedance spectroscopy [123–125], and resistive devices [126–128]. Electrochemical impedance spectroscopy measures the impedance of the system. The method is sensitive to capacitive and inductive effects [121]. Resistive devices are mainly used for gas sensing applications since measuring in buffers is challenging due to the high ionic strength of the medium [129].

2.3. Analytes

The analytes of this project are the VOCs 2-propanol, heptanal, and acetophenone.

2.3.1. 2-Propanol

2-Propanol is a colourless liquid. Figure 13 shows the structure of the molecule. It has a characteristic fruity odour and is best known for its use in rubbing alcohol and disinfectant. Furthermore, it is found in cleaning products, cosmetics and pharmaceuticals. [130]
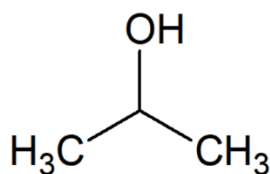
Figure 13: Structure of 2-propanol.

If ingested, hepatic alcohol dehydrogenase converts isopropanol to acetone which is excreted through urine and a minor part through the breath. The effects on the nervous system are similar to those of ethanol. However, they can be more severe. [130]

2.3.2. Heptanal

The aldehyde heptanal is a known biomarker for lung cancer. Figure 14 shows the structure of heptanal. High levels of aldehydes are found in the blood and cancer cells of patients. Heptanal together with hexanal is also emitted via the exhaled breath. [131] The aldehydes are formed by reactions of radicals with cellular lipids. The increase of aldehyde production is an indicator for high oxidative stress, which makes them possible biomarkers for cancer diagnostics. [132]
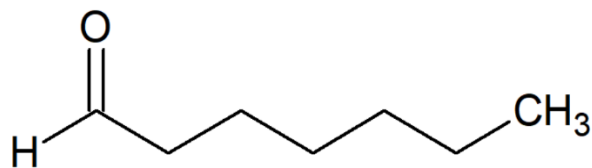
Figure 14: Structure of heptanal.

2.3.3. Acetophenone

Acetophenone is the simplest aromatic ketone (Figure 15). It is a colourless to pale yellow, viscous liquid with sweet, pungent odour. It is a naturally occurring substance in various fruits and vegetables, meat, milk and cheese, and grains. [133]
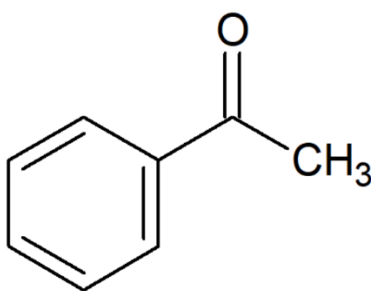
Figure 15: Structure of acetophenone.

Acetophenone is naturally present in tobacco. Nevertheless, it is also added to cigarettes as an additive to preserve the tobacco taste during manufacturing. [134] Acetophenone is produced as a by-product of the cumene process. [135] Commercially, it is usually produced by selective catalytic oxidation of ethylbenzene with oxygen. Commonly, one uses homogeneous cobalt-based catalysts for that purpose. The reaction takes place in the presence of manganese or bromide additives. [136,137] Other reports include a heterogeneous Ti-Zr-Co alloy catalyst. [138] Acetophenone production is relevant for the chemical industry, because the compound is a valuable precursor in the production of resins, such as acetophenone-formaldehyde resins. [139] Moreover, it is used in perfume production. Typically, it gives the perfume a fragrance of orange blossom. [140] Finally, it also plays a role in the production of

pharmaceuticals. [141,142] In the late 19th century acetophenone was used as a hypnotic and sleep-inducing drug. The sedative was known by the name Hypnone and was administered hypodermally. [143]

2.3.4. Biomarkers/Breath Analysis

The above-mentioned analytes have in common, that they are relevant for cancer diagnostics. Diseases affect the metabolism of a person, which leads to the production of certain substances, so-called biomarkers. Those can be found in the blood, urine, or sweat, but also in exhaled breath. [9]

The human breath contains a myriad of components, including VOCs. Some of them are exogenous volatiles, which are inhaled from the surrounding environment, produced after orally ingesting food, or derived from smoking. Endogenous compounds, in contrast, are blood-borne and released via the lungs or produced by symbiotic bacteria. [9] Blood-borne VOCs diffuse across the pulmonary alveolar membrane from higher to lower vapour pressure. They are suitable for detecting non-respiratory diseases. [144] Both types of VOCs occur at very low concentrations in the nanomolar or picomolar range which makes it hard to distinguish exogenous from endogenous compounds. However, collecting breath samples is easy, painless, and non-invasive. [9]

The levels of these compounds in breath correspond to the levels in blood, making breath analysis a valuable tool for diagnosis. This is supported by the fact that many diseases generate high levels of reactive oxygen species (ROS) that damage cell membranes and release alkanes into the bloodstream, which are eventually exhaled. Additionally, diseases can alter the body's metabolism of fat, proteins, and sugars, leading to a distinct pattern of exhaled VOCs that differentiates them from healthy breath. In infectious diseases, the VOCs are produced by microbial species. Identified biomarkers often include small molecules, such as alkanes, benzene derivatives and other aromatic compounds alcohols, ketones and aldehydes. [144] Certain breath VOCs linked to diseases are already used for diagnosis. For example, acetone for diabetes, trimethylamine for trimethylamineuria, methylmercaptan for fetor hepaticus. [9]

Breast Cancer

Cancer research has increasingly focused on identifying breath biomarkers for early diagnosis. This is also the case for breast cancer, which is the most diagnosed malignancy among females. Next to lung cancer, it is the second leading cause of cancer-related deaths worldwide. One of the most important strategies to improve the survival rate is early diagnosis. However, the disease usually develops asymptomatically

which makes this difficult. Current screening techniques are expensive, cause discomfort, and can even be harmful for patients. Furthermore, they often do not fulfil the requirements of reliable discrimination between breast cancer patients and healthy subjects. [145] Conventional diagnostic techniques include mammography, ultrasound imaging, magnetic resonance imaging, CT scan, positron emission tomography scan, and biopsies. The preferred screening method for breast cancer is mammography. This technique is effective, but its sensitivity significantly decreases, when the breast tissue is either dense, or shows heterogeneous density. In extremely dense breast, mammography misses almost half of the tumours. [146] Such uncertainties lead to repeated exposure to radiation, surgical interventions, and emotional and psychological stress for the patients. [147] Ultrasound imaging and MRI can detect malignant and invasive cancers. However, these screening methods have shown to lead to overdiagnoses in several studies. [146]

Breath analysis on the other hand offers the advantage of being non-invasive and is thus painless and easy to perform. The method provides a potentially useful approach to screening breast cancer. [145]

Especially in combination with the available imaging methods, breath analysis may help to facilitate early detection of breast cancer. Suitable screening tools should be able to detect disease in its early stage, with good precision and high sensitivity. [147]

In 1994 Hietanen et al. first examined the breath of breast cancer patients and found significantly increased pentane levels compared to healthy controls. This was attributed to elevated oxidative stress. [148]

Phillips et al. screened three groups of females for alkanes and monomethylated alkanes. The groups included females with and without histologically proven breast cancer, and healthy volunteers. The authors found that they could distinguish between healthy females and females with breast cancer via markers in their breath. They were also able to distinguish between females with breast cancer and healthy females with an abnormal mammogram. They even claimed that screening for biomarkers was superior to mammography in terms of the negative predictive value. The compounds of a subset of eight VOCs in breast cancer patients were either increased or decreased compared to healthy individuals of the same age. Increased biomarker levels may stem from oxidative stress, while a decrease is most likely caused by an increased activity of cytochrome P-450. These are both accompanying effects of breast cancer. [149]

In a different study, Phillips et al. determined whether it is possible to predict breast cancer by screening breath VOCs and applying fuzzy logic. They concluded that a combination of five markers is necessary to

predict the disease. The VOCs in question are 2-propanol, 2,3-dihydro-1-phenyl-4(1H)-quinazolinone, acetophenone, heptanal and isopropyl myristate, which in part have been used as analytes for this project. [11]

Analysis Methods

The gold standard for breath VOC testing is GC-MS. This technique is also used to identify unknown biomarkers in complex mixtures. Even though GC-MS is a very established and sensitive method with detection limits in the ppb range, it is not suitable for point-of-care testing. GC-MS devices are expensive, immobile machines and measurements are time-consuming. Sensors in general solve some of these problems. They are usually portable and can measure in real time. Piezoelectric sensors such as the QCM, are sensitive and can be functionalised with a wide range of coatings to tailor the affinity to specific analytes. However, they are sensitive to changes in the environment, such as vibrations and temperature changes. Chemiresistive sensors operate at room temperature and respond rapidly. However, humidity can be an issue and drying of the sample might be necessary. [150]

3. Experimental

3.1. Materials

Table 1 summarises all chemicals used in this work. It lists the supplier and purity for each compound.

Table 1: List of the chemicals used, including supplier and purity of the substance.

Name	Supplier	Purity
2-propanol	VWR	
Diphenylmethane 4,4'- diisocyanate (DPDI)	Merck	Mixture with 20-40 % triisocyanate
Acetophenone	Sigma Aldrich	99 %
Acrylamide (AA)	Merck	>99 %
Azobisisobutyronitrile (AIBN)	Sigma Aldrich	98 %
Bisphenol A (BPA)	Alfa Aesar	97+ %
Diphenylmethane (DPM)	Sigma Aldrich	99 %
Dimethyl sulfoxide (DMSO)	VWR	
Ethylene glycol dimethacrylate (EGDMA)	Sigma Aldrich	≥97.5 %
Heptanal	Sigma Aldrich	95 %
N-Isopropyl acrylamide (NIPAM)	Alfa Aesar	97 %
Methacrylic acid (MAA)	Sigma Aldrich	≥99 %
N,N-Dimethylacrylamide (DMAA)	Sigma Aldrich	99 %
P3HT (MW = 24.480)	Ossilia	93.6 % RR
Phloroglucinol (PG)	Alfa Aesar	98 %
Tetrahydrofuran (THF)	VWR	

3.2. Polymer Synthesis and cMIPs

In general, all MIPs were prepared by bulk imprinting. This means that the template was added directly to a solution of functional monomer and crosslinker in a suitable solvent. In some cases, sonication (ultrasonic bath Elma Elmasonic S120) was necessary to dissolve all components. Batches leading to acrylate- and acrylamide-based polymers were flushed with argon to remove oxygen prior to initiating the

reaction, which took place with AIBN. The monomer solutions were thermally pre-polymerised in a water bath. When reaching the gel point, the oligomer solution or a dilution was either spin- or drop-coated on the QCM electrodes. Some polymers required curing under UV light at 312 nm. Templates were removed from the polymer matrix either via evaporation (for volatile compounds), or by washing the fully cured MIPs.

The P3HT blends were prepared by mixing pre-polymerised MIP solutions with a P3HT stock solution. The stock solution was prepared by dissolving 10 mg P3HT in 1 mL THF. The mixtures were spin- or drop-coated on QCMs or drop-coated on chemiresistors.

The procedures below describe the MIP syntheses. NIPs and cNIP blends were prepared in the exact same way as the corresponding MIPs without adding the template.

3.2.1. PU (2-Propanol)

This procedure was adapted from a previous publication of the group. [78] The MIP preparation process was optimised, and a suitable NIP was established. According to the original procedure, a MIP stock solution was prepared from 1 g DPDI, 1.97 g of BPA and 0.22 g PG in 2 mL THF. This was downscaled to 250 mg DPDI, 492 mg BPA and 55 mg PG in 500 µL THF. Figure 16 shows the chemical structures of the monomers and the crosslinker. 30 µL of this stock solution were diluted in 970 µL of the template 2-propanol. Prior to spin-coating, the solution was further diluted 1:30 with 2-propanol. Since the original procedure did not include the preparation of a corresponding NIP, this was done by diluting the first stock solution in the same way as the MIP with THF instead of the template. 5 µL of the diluted oligomer solutions were spin-coated on the QCM electrodes for 4 min at 3000 rpm. Afterwards, the layers were cured at room temperature overnight and placed in the oven at 80°C for 3h prior to measurements to ensure the removal of the volatile template.
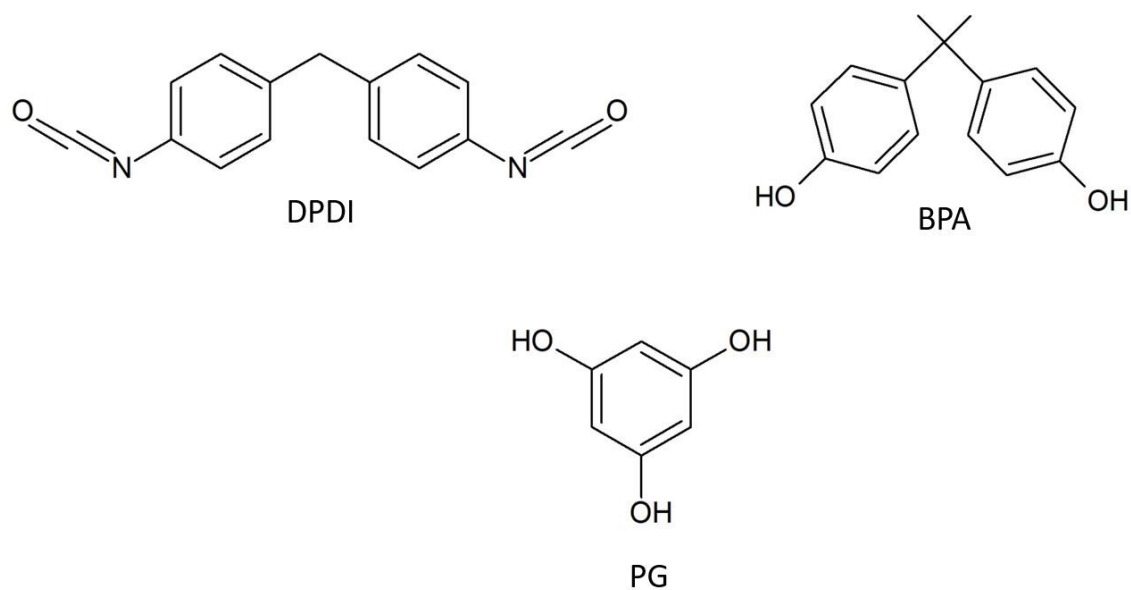
Figure 16: Structures of the monomers and the crosslinker.

The result section explains the optimisation process. For the optimised MIP, 30 µL of the stock solution were diluted in 970 µL of a 1:2 (v/v) mixture of the template 2-propanol and THF. 50 µL DPM were added as a porogen. The NIP solution was prepared in the same way using only THF instead of the 2-propanol/THF mixture. Prior to coating, both solutions were diluted 1:2 with THF. Figure 17 shows the process for clarification. Each QCM electrode was spin-coated with 5 µL of the respective oligomer solution for 4 min at 3000 rpm.

Figure 17: Preparation process of PU MIP and NIP solutions.

3.2.2. DMAA-*co*-EGDMA (Heptanal)

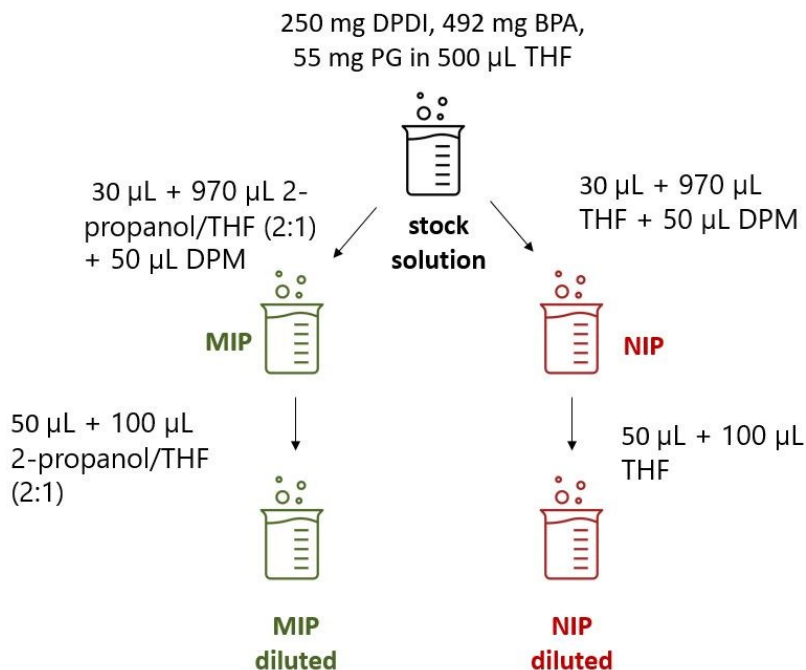The first experiments with heptanal MIP followed a published procedure using MAA and EGDMA for polymer synthesis. [151] 15 µL of the functional monomer MAA and the template heptanal were dissolved in 600 µL DMSO. 25 µL of the crosslinker EGDMA and 2.4 mg of the initiator AIBN were added. The mixture was sonicated for 10 min. Afterwards it was flushed with argon to remove oxygen. The solution was pre-polymerised in a water bath at 70°C while stirring under argon atmosphere. The viscous oligomer solution was coated onto the QCM electrodes by spin-coating 4 µL for 30 seconds at 200 rpm. The NIP was prepared in the same way in the absence of the template. The polymers were cured under UV light (312 nm) overnight. After comparing the sensor signals obtained with MIPs prepared from various functional monomers, including AA, NIPAM and DMAA, MIP synthesis continued relying on DMMA instead of MAA. The additional amine group was believed to promote stronger interaction of the monomer with the aldehyde. Figure 18 shows the monomers and crosslinker used for the polymers.
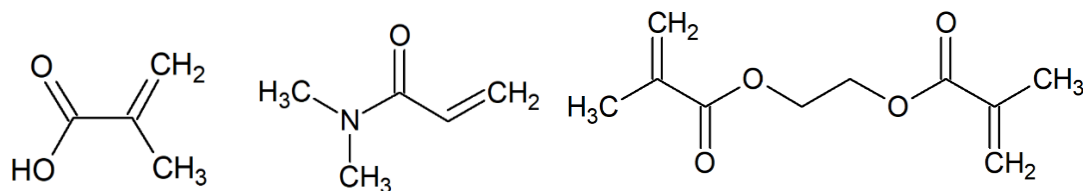
Figure 18: The chemical structures of the functional monomers MAA, DMAA and the crosslinker EGDMA (left to right).

The solvent DMSO was exchanged with the more volatile THF. In the final procedure 18 µL DMMA, 25 µL EGDMA and 15 µL heptanal were dissolved in 540 µL THF. The mixture was flushed with argon. Then 60 µL of a solution of 24 mg AIBN in 600 µL THF was added, and the solution was flushed with argon again. After 10 min sonication, the monomer solution was pre-polymerised in a water bath at 70°C while stirring under argon atmosphere. 4 µL of the pre-polymerised solution were spin-coated onto QCMs for 30 seconds at 2000 rpm. The polymer was cured under the UV lamp (312 nm) overnight (16-18h). To remove the template and remaining solvent, the QCMs were heated in a muffle furnace (Thermolyne 1300) to 150°C until the resonance frequency did not increase further.

3.2.3. MAA-*co*-EGDMA (Acetophenone)

The original procedure was based on a previous publication on MIPs for terpenes. [152] 60 µL MAA and 16 µL acetopheneone were dissolved in 1197 µL THF by sonicating for 5 min. 200 µL of a solution containing 7 mg/mL AIBN as well as 527 µL EGDMA were added. The mixture was again sonicated for 5 min. Oxygen was removed by flushing with argon for 4 min. The NIP was prepared in the same way without adding acetophenone. MIP and NIP were spin-coated onto QCM sensors (2 µL, 2000 rpm, 15s) and cured overnight (16-18h) under UV light (312 nm). The polymer layers were washed in ethanol for 15 min to remove the template. Since the original composition and coating process did not yield homogeneous layers of sufficient thickness, it was adapted. For the optimum results, 60 µL MAA and 16 µL acetophenone were dissolved in 497 µL THF and sonicated for five minutes. Then 527 µL EGDMA as well as 400 µL of a solution containing 35 mg/mL AIBN in THF (= 1 wt. % with respect to monomer and crosslinker) were added. The mixture was sonicated again. Oxygen was removed from the mixture by flushing with argon for four minutes. This was done to avoid side reactions. The tube was placed in a water bath at 60°C. Pre-polymerisation took place under stirring with magnetic bars and under argon atmosphere until the gel-point was visibly reached. This was usually the case after 60 minutes when the viscosity increased to

a gel-like state. The oligomer solution was cooled in an ice bath to prevent further polymerisation. Both MIP and NIP oligomer solutions were diluted 1:10 with THF prior to QCM coating. All polymers were cured in UV light (312 nm) over night. To remove the template the sensors were stirred in a petri dish filled with ethanol for 15 min.

3.3. Measurements/Methods

3.3.1. Sensor Fabrication

QCM

AT-cut 10 MHz quartz plates (The Roditi International Corporation Ldt, UK) with a diameter of 14 mm and a thickness of 168 µm were equipped with dual-channel gold electrodes. For early experiments with 2-propanol, screen printed electrodes were used. Gold paste (Heraeus GGP 1229D-10 % H, bright gold paste) was applied through a self-made stencil and heated to 400°C for 4h in an oven (Heraeus Thermicon P). Figure 19 shows the screen-printed electrodes and the stencil. On the top side, which was coated with the polymers, the electrodes had a diameter of 5 mm. The electrodes on the bottom side measured 4 mm in diameter, resulting in 4 mm active area, where the top and bottom electrodes overlapped.

Figure 19: QCM gold electrodes applied by screen-printing. Left: Stencil used for applying the gold paste. Right: The resulting electrodes.

The larger part of the experiments was performed with electrodes applied by physical vapour deposition (PVD) through a self-made shadow mask. Figure 20 shows the electrode design. An interlayer of 2 nm chromium was necessary to immobilise the 60 nm gold layer on the quartz surface. The electrodes had a diameter of 5 mm on both sides of the QCM.
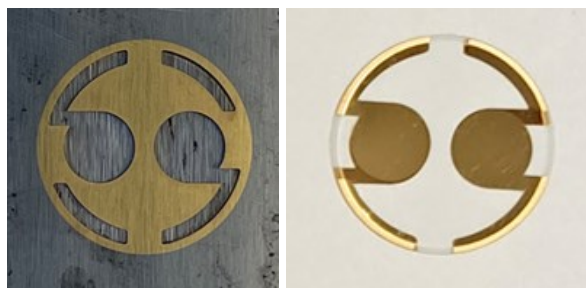
Figure 20: QCM gold electrodes applied by PVD. Left: Shadow mask used for applying the gold paste. Right: The resulting electrodes.

The reason for switching from screen-printing to PVD was to obtain more reproducible electrodes. Figure 21 shows microscope images of QCM electrodes prepared by screen-printing and PVD respectively. The screen-printed electrode has a much rougher surface whereas the PVD electrode appears smooth. The difference is also evident at the edges of the electrodes. The PVD electrodes have well defined edges while the ones of the screen-printed electrodes are irregular and fringed.
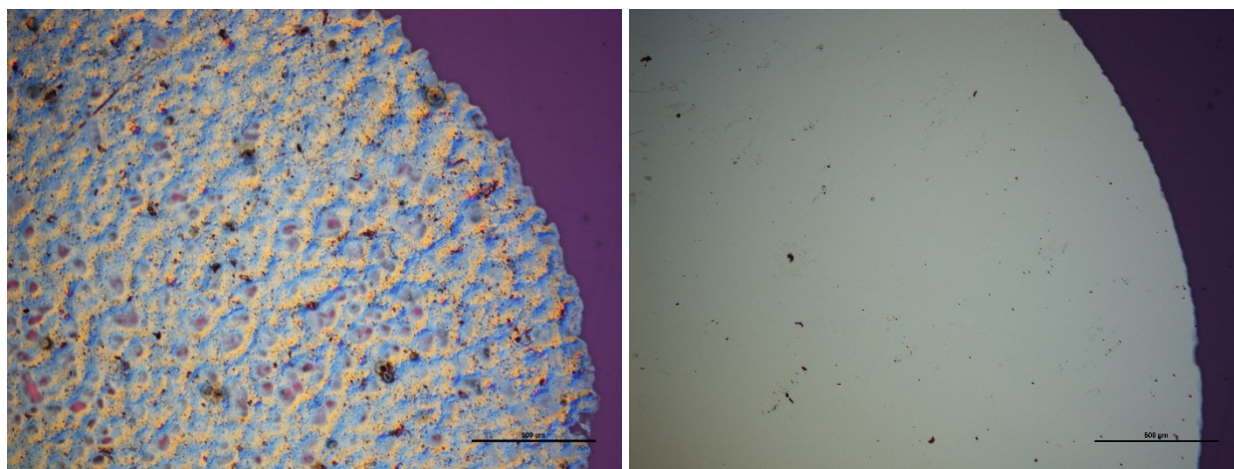
Figure 21: QCM electrodes. Left screen-printed. Right: PVD. Scale bar: 500 µm.

The electrodes were cleaned with acetone and ethanol and treated with oxygen plasma (Diener Zepto with Balcers TPC 015 vacuum pump) prior to coating. One of the electrodes was covered with MIP (blend) solution by either drop- or spin-coating and later used as the measuring electrode. The second electrode was covered with the respective NIP (blend) and served as the reference. For spin-coating a

programmable spin-coater (G3P-8 from Specialty Coating Systems) was used. The resonance frequency of each electrode was measured before and after coating with a network analyser (Agilent Technologies, ENA Series Network Analyzer, E5062A, 300 kHz – 3 GHz). This allows for evaluating the layer thickness according to the Sauerbrey equation. As a rule of thumb, a frequency decrease of 1 kHz from uncoated to coated QCM equals roughly a layer of 40 nm. Figure 22 shows the same QCM electrode before and after coating with PU. Coating with the polymer shifts the resonance frequency to lower values. Furthermore, damping increases after coating.
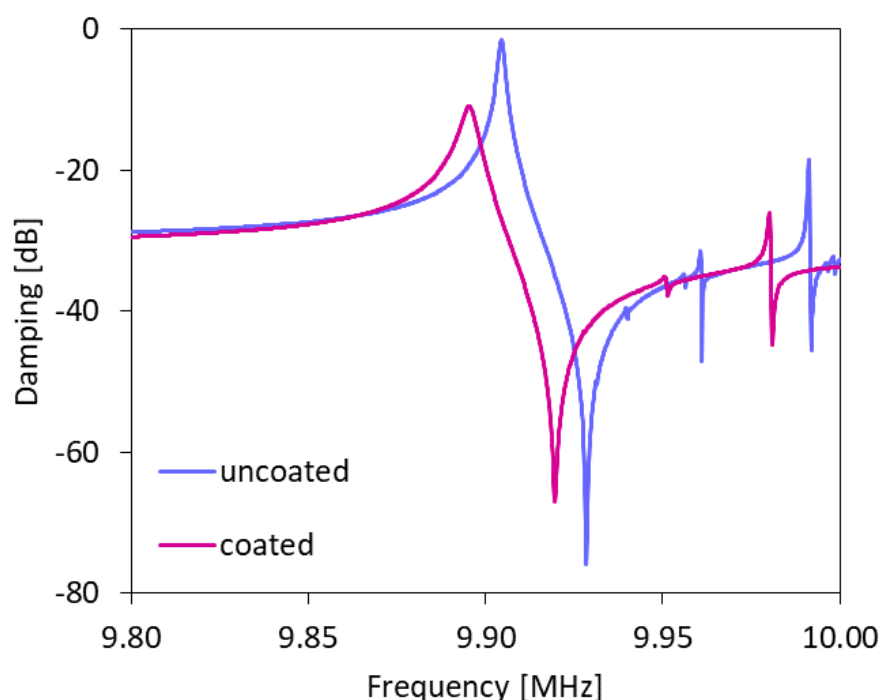
Figure 22: Networkanalyser measurements of the same QCM electrode before and after coating with PU. The resonance frequency is shifted to a lower value after coating. The PU layer on this electrode is approximately 90 nm thick.

Chemiresistor

The chemiresistor sensors were custom-made by a commercial supplier (multi-cb boards, Brunnthal, Germany) They are based on a voltage divider and have two gold IDEs, one sensing and one reference electrode. Figure 23 provides a microscope image of the IDE. The design is based on a recent publication. [21] Both IDEs were coated with 3 µL of the same P3HT blend. Before the measurement, the reference electrode (in this case always the lower one of the two IDEs) was sealed with Kapton tape to remain

constant during the measurement. Conductivity and sufficient coverage of the electrodes was ensured by measuring the electric resistance with a multimeter (RS Pro, RS-14, Autoranging Digital Multimeter) and light microscope.
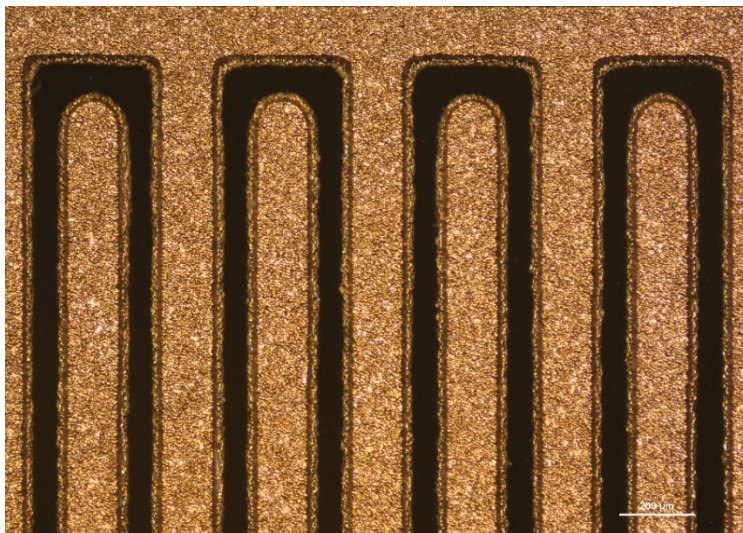
Figure 23: IDEs of a chemiresistor. Scale bar: 200 µm.

3.3.2. Measuring Set-Up

Measurements were conducted on a self-built gas-measuring set-up shown in Figure 24. Gas flow was regulated via a flow computer (Westphal Mess- und Regeltechnik WMR 4008) connected to mass flow controllers (Brooks Delta II). One of the flow controllers was responsible for the background air. Another one was connected to a gas washing bottle filled with the analyte in liquid form. When this valve was opened, air streamed through a frit in the solvent. This way solvent saturated air was created in the bottle. This stream was combined with the background air before being led into the measuring cells.
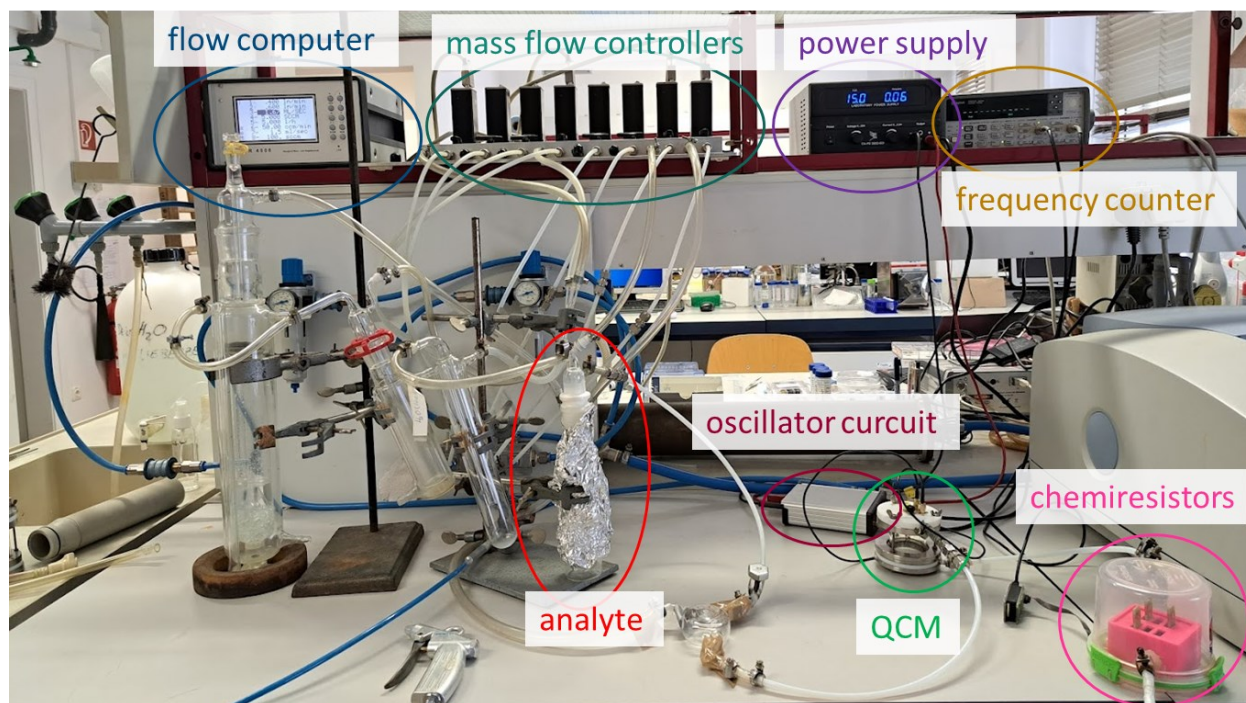
Figure 24: Measuring set-up.

The measurements took place in constant flow of either 1 L/min or 3 L/min. At the beginning of each measurement the cell was flushed with clean air until a stable baseline was reached. Different analyte concentrations were introduced by adjusting the airflow and flow of analyte-saturated air accordingly. The concentration can be estimated from the volume flows and the vapour pressure of the respective solvent following Equation 4.

Equation 4: Calculation of the analyte concentration:

$$c_{sol} = \frac{V_{sol}\left(1 + \frac{p_{sol}}{p_0}\right)}{V_{sol}\left(1 + \frac{p_{sol}}{p_0}\right) + V_{air}} * \frac{p_{sol}}{p_0} * 10^6 \; [ppm]$$

c_{sol}...*concentration of the solvent in ppm*

V_{sol}...*volume flow of the air going through the solvent in L/min*

V_{air}...*volume flow of the background air in L/min*

p_{sol}...*vapour pressure of the solvent in bar*

p_0...*atmospheric pressure, 1.013 bar*

For QCM measurements a self-made oscillator circuit was connected to a power supply (EA Elektro-Automatik, EA-PS 2032-025) and a frequency counter (Agilent 53131 A225 MHz Universal Counter). The QCM was placed in a self-made measuring chamber (Figure 25).
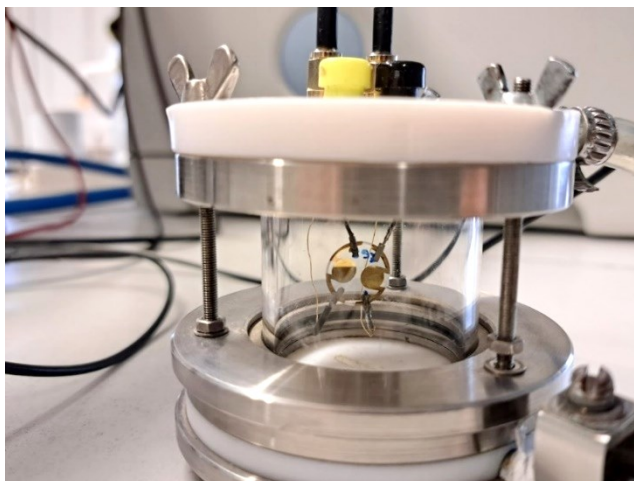
Figure 25: QCM measuring cell.

A self-built sensor board with six USB ports for the simultaneous measurement of up to six chemiresistors (Figure 26) was placed in a self-built measuring chamber. The chamber was connected to the same gas-flow set-up as the QCM cell. Measurements were performed in the exact same way as described above. The sensor board has a built-in humidity and temperature sensor.
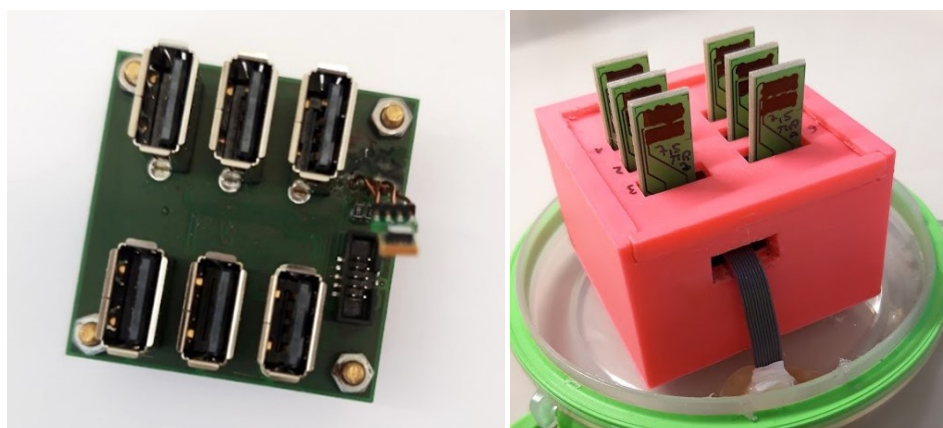
Figure 26: Chemiresistor sensor board for array measurements.

The actual sensor board can be seen on the left side. On the right side it is placed inside a 3D-printed case with removable lid. This case was made to protect the electronics from the solvent vapours during the measurements and damage and dust from handling and storage in between measurements. The chemiresistor cell can be connected to the QCM cell, which allows for simultaneous measurements of both types of sensors.

4. Results

4.1. 2-Propanol

4.1.1. Original Procedure

The first step in developing the sensor was reproducing the MIP of the original procedure explained in the experimental section and optimising the layer height of the resulting films. Table 2 shows the average thickness of the resulting layers. It is evident that the layers are too thin: Desirable layer heights for QCM measurements are in a range between 50 and 200 nm.

Table 2: Layer thickness of QCMs coated with PU MIP and NIP according to the original procedure. NIP: n=7, MIP: n=6.

	Average height [nm]	Standard deviation [nm]
NIP	31	15
MIP	23	12

Nevertheless, measurements were conducted with different concentrations of 2-propanol in dry air to assess the imprinting effect. Concentrations used were: 1000-900-800-700-600-500 ppm. Figure 27 shows an example of a measurement. In this case, the frequency shift on the MIP-coated electrode is larger than on the NIP-coated electrode, which is the desired outcome. However, the signals in general are rather small with frequency shifts below 10 Hz for the highest concentration. The frequency shifts are reversible when flushing the cell with air. The figure also shows the average MIP and NIP signals of the batch:
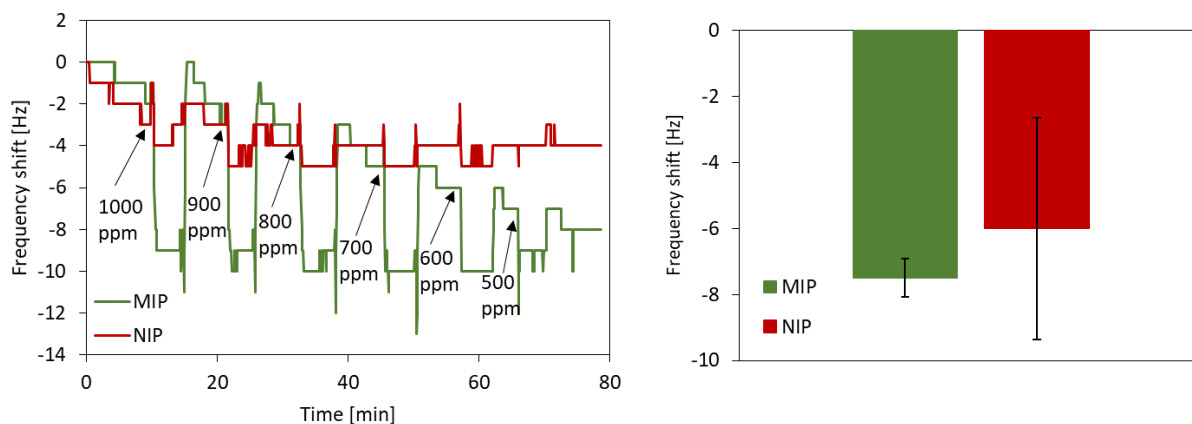

Figure 27: Right: QCM measurement with different 2-propanol concentrations. The cell was flushed with clean air in between the concentrations. Left: Average frequency shifts for 1000 ppm 2-propanol. n=4.

The frequency shifts of MIP and NIP do not differ from each other in a statistically significant way. MIP signals are consistent at around -8 Hz. NIP signals vary more. Since the layers are similar in height, the signals are in this case not normalised to layer height. The frequency curves appear edgy which is caused by the measurement set-up operating at a resolution of 1 Hz.

4.1.2. Increasing Layer Thickness

Spin-Coating Parameters

The first optimisation step was increasing the layer thickness. One approach to do so is altering the spin-coating time. The original 4 minutes were reduced to 3 and 2 min respectively. Table 3 shows the results.

Table 3: Average layer height of PU MIP and NIP on QCM electrodes. Spin-coating parameters: 5 µL, 3000 rpm for either 3 or 2 min. n=3.

3 min	Average height [nm]	Standard deviation [nm]
NIP	51	11
MIP	41	22
2 min		
NIP	55	27
MIP	38	11

Although the average NIP layer increased from initially 31 nm to 51 nm and 55 nm respectively, the layers heights are still on the lower limit of the ideal range. MIP layers are less affected by the change in spin-coating time.

Dilution Factor

Thus, the next step in optimisation of the layer thickness was reducing the dilution factor before spin-coating the pre-polymer but using the original spin-coating parameters (5 µL, 4 min, 3000 rpm). The MIP and NIP solutions were coated undiluted as well as in dilutions of 1:2, 1:10 and 1:20.

Table 4 shows that coating the undiluted MIP and NIP solution leads to layers coming close to the µm range which is too thick for OCM measurements.

Table 4: Average layer height on QCMs coated with the undiluted MIP and NIP solutions. n=5.

Undiluted	Average height [nm]	Standard deviation [nm]
NIP	960	535
MIP	640	416

Table 5 shows the results of coating 1:2 diluted MIP and NIP solutions. Since only results of two QCMs are available, the individual layer heights are stated instead of the average. The layers are in a desirable range between 50 and 200 nm with one MIP layer being noticeably thicker than the other layers.

Table 5: QCMs coated with 1:2 diluted MIP and NIP solutions. The layer heights are stated individually since only 2 sensors could be measured.

1:2	QCM 1 height [nm]	QCM 2 height [nm]
NIP	218	108
MIP	90	93

Table 6 shows the average layer heights of 1:10 diluted MIP and NIP solutions. The polymer layers are in the desired range.

*Table 6: Average layer height on QCMs coated with 1:10 diluted MIP and NIP solutions. n=3.*

1:10	Average height [nm]	Standard deviation [nm]
NIP	90	26
MIP	69	14

A dilution of 1:20 instead of 1:30 places most layers on the lower limit of the previously stated range of thickness (Table 7). In this case again only two measurements are available.

Table 7: QCMs coated with 1:20 diluted MIP and NIP solutions. The layer heights are stated individually since only 2 sensors could be measured.

1:20	QCM 1 height [nm]	QCM 2 height [nm]
NIP	45	53
MIP	65	15

Overall, one can thus conclude that diluting the initial stock solution by 1:10 or 1:2 leads to polymer layers that are sufficiently thick. Figure 28 shows examples of QCM measurements with sensors coated with undiluted and 1:2 diluted MIP and NIP solutions. The QCM signals increased from initially less than 10 Hz to around 30 Hz for 1000 ppm 2-propanol. This may be connected to the increased layer thickness. Even though the polymer layers prepared with the undiluted polymers are approximately five times thicker than the 1:2 dilutions, the frequency shifts are in the same range. This could be an indication that the thickness of the layers only plays a role up to a certain point and in very thick layers the analyte cannot reach imprints closer to the electrode anyway. Layers in a range of the undiluted polymer can cause high damping and are most likely not completely rigid. Therefore, they often do not lead to reliable sensor signals. However, the QCM data also reveals that the difference of the frequency shifts of MIP and NIP is rather small. This indicates that a large amount of the signal is caused by unspecific binding. One reason for this could be decreased accessibility of the imprints in the bulk of the MIP.
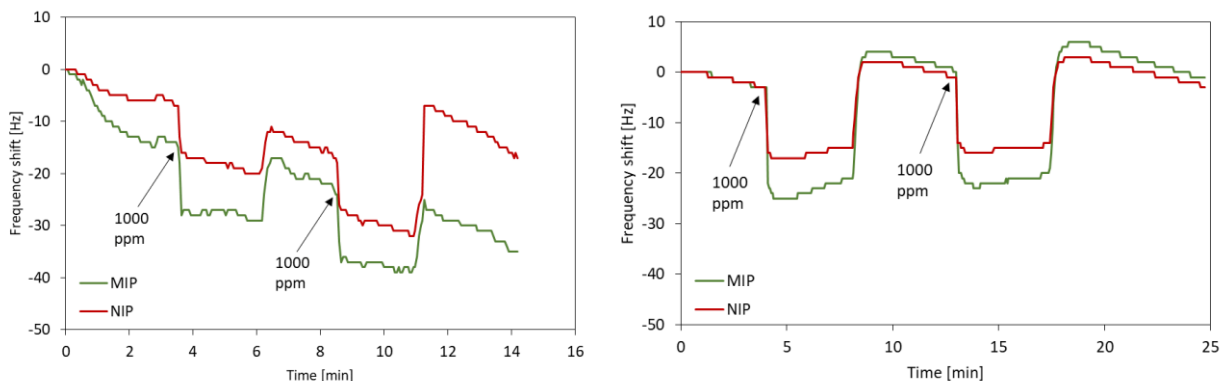
Figure 28: QCM coated with undiluted MIP and NIP solution (left) and 1:2 dilutions (right).

4.1.3. Porogen

To enhance the accessibility of the imprints, a porogen was added, namely 60 µL DPM (10 v%). The rest of the procedure for MIP and NIP preparation followed the original recipe with different dilutions being spin-coated. Table 8 shows the average thickness of the layers prepared from 1:30 dilutions which agrees well with the results shown in the previous section.

Table 8: Average layer height on QCM coated with MIP and NIP prepared with 10 v% in the stock solution. n=3.

	Average height [nm]	Standard deviation [nm]
NIP	50	16
MIP	40	17

Figure 29 shows the results of two QCMs measurements from this batch. In both cases, the MIP signal is stronger than the NIP signal. However, the absolute frequency shifts differ from one another. For the same 2-propanol concentration one sensor exhibits a frequency shift of -7 Hz while the other one reaches -17 Hz on the MIP-coated channel. The difference in frequency shifts can in this case not be attributed to the layer thickness: The MIP layer on the sensor showing larger frequency shifts is in fact thinner (68 nm) than on the other QCM (45 nm). The NIP layers measure 30 nm on both QCMs and yet the absolute frequency shifts vary. This indicates that other effects influence the magnitude of the frequency shifts. From those results one may conclude that reproducibility between the sensors is limited.
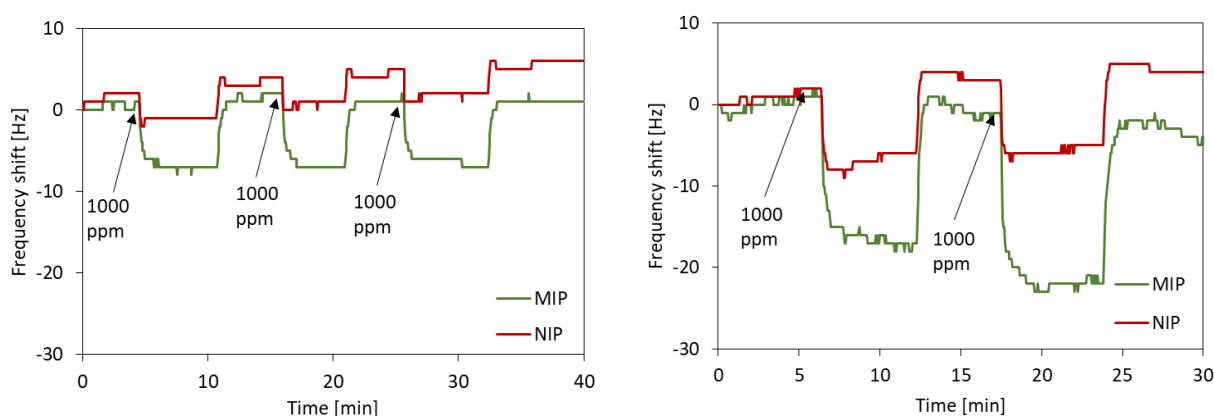

Figure 29: QCM measurements with two sensors coated with MIP and NIP with DPM in the stock solution.

Table 9 shows the layer heights of polymers resulting from the same stock solution as above containing 10 v% DPM, 1:10 diluted. The layers are in accordance with the previous experiments. However, they show a large standard deviation.

Table 9: Average layer height of MIP and NIP. Both prepared from a stock solution containing 10 v% DPM. MIP and NIP diluted 1:10 before spin-coating. n=3.

	Average height [nm]	Standard deviation [nm]
NIP	95	75
MIP	95	65

From this batch, only one sensor could be measured (Figure 30). Even though the layer height increased, the frequency shifts of -8 Hz for 1000 ppm of the analyte are comparable to the ones obtained with the 1:30 diluted MIP and NIP solutions. In this particular measurement, the imprinting effect seems worse when the solutions are less diluted. However, given the very limited number of measurements for both solutions, it is impossible to make a definitive statement.
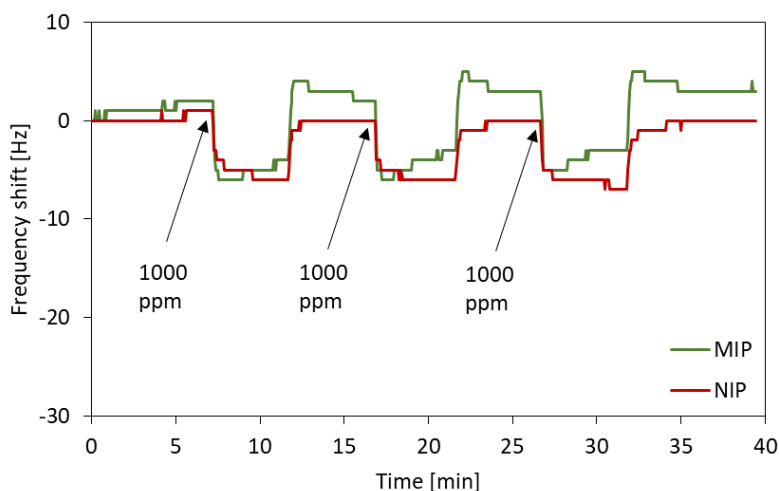
Figure 30: QCM measurement. Coated with 1:10 dilution of MIP and NIP solution.

To test the influence of adding the porogen at a later stage of the preparation process, DPM was added to the MIP and NIP solutions before diluting 1:30 instead of directly to the stock solution. To each solution 50 µL of the porogen were added which equals 5 v%. Table 10 states the average layer heights. The NIP layers are on average noticeably thicker than the corresponding MIP layers. Given the high standard deviation, this is a result of fluctuations in the batch.

Table 10: MIP and NIP solutions containing 5 v% DPM. Both diluted 1:30 before spin-coating. n=6.

	Average height [nm]	Standard deviation [nm]
NIP	68	56
MIP	30	12

Figure 31 shows that the absolute frequency shift is larger on the MIP-coated electrodes than on the NIP-coated ones. Also, the standard deviation is larger while NIP signals only deviate by 1 Hz. No correlation between layer height and the magnitude of the frequency shifts was observed.
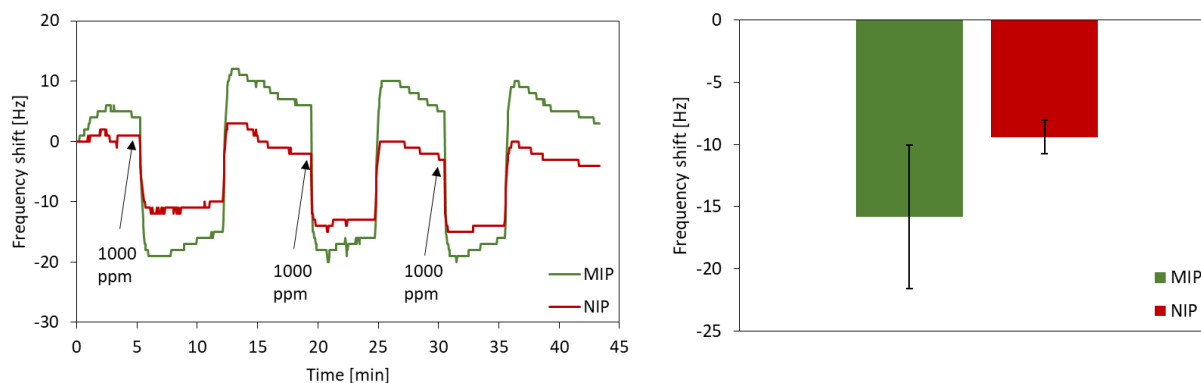

Figure 31: Example of a QCM measurement and average frequency shifts of QCM sensors coated with MIP and NIP containing 5 v% DPM, diluted 1:30. n=5.

With this composition, coating both sides of the QCM to obtain thicker layers and thus more binding sites to enhance the signals was briefly tested. Table 11 states the average combined layer thickness. Coating

both sides of the electrodes with the same polymer increases the layer height. However, the effect is rather small. In some cases, the damping is too high (exceeding -12 dB) to measure the sensors.

Table 11: Average layer height on QCMs coated on both sides. n=6.

	Average height [nm]	Standard deviation [nm]
NIP	89	28
MIP	65	26

Figure 32 shows QCM measurements with single vs. double-sided coating of the same sensor. One can clearly see that the signal increases by coating both sides of the QCM. The increase in frequency shift affects both MIP- and NIP-coated side. The difference between MIP and NIP signal increases by a few Hz.
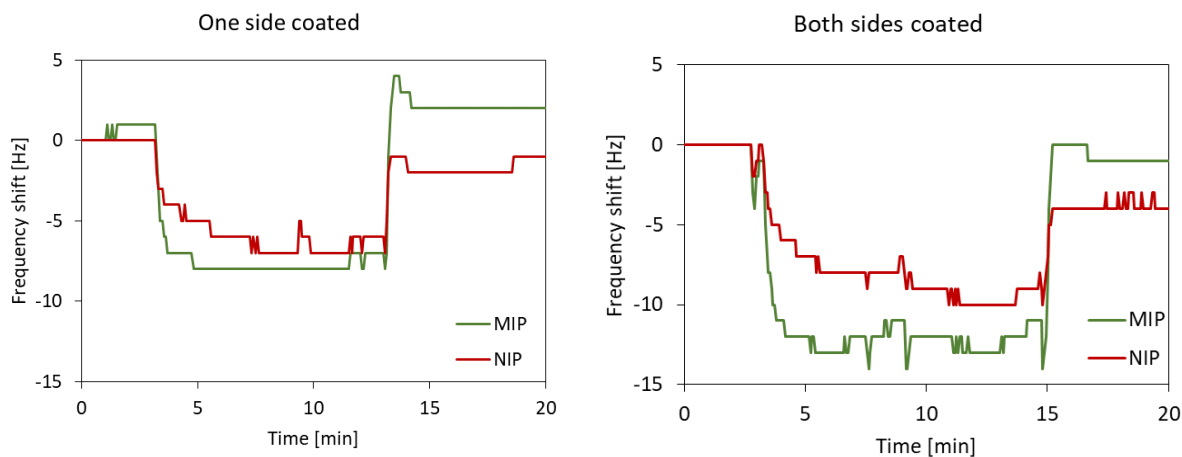
Figure 32: Comparison of the same sensor exposed to 1000 ppm 2-propanol. Left: one side coated with PU MIP and NIP. Right: Both sides coated.

It is evident that there is an increase in the frequency shifts, which can also be seen in the average signals in Figure 33. Since the polymer batch did not show a large imprinting effect in the experiments with only one side coated, it is impossible to say if double-sided coating improves the imprinting factor. However, due to the issues with high damping, the double-sided coating was not continued.
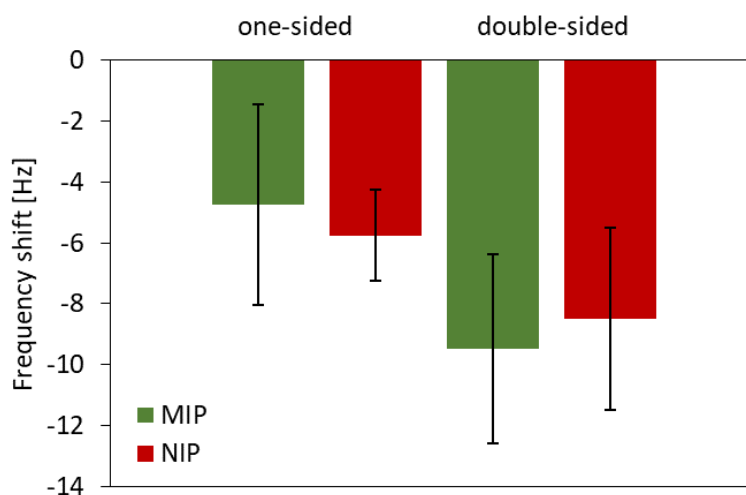
Figure 33: Comparison of QCM signals for 1000 ppm 2-propanol. One-sided vs. double sided coating. n=5.

Table 12 shows the average layer heights of polymers prepared from the same stock solution but diluted 1:2.

Table 12: Average layer height on QCM. MIP and NIP 1:2 diluted. MIP and NIP solutions contained 5 v% DPM. n=6.

	Average height [nm]	Standard deviation [nm]
NIP	218	95
MIP	178	119

Figure 34 shows an example of a QCM measurement as well as the absolute and normalised frequency shifts of all sensors of this batch. In the measurement shown, the MIP shifts are significantly larger than the shifts on the reference electrode. The large frequency shift on the MIP-coated electrode (-74 Hz) compared to the previous measurements is also noticeable. However, this is the only measurement out of four in total presenting this behaviour. The other sensors showed smaller frequency shifts and less difference between MIP and NIP signals. After normalising to 100 nm all MIP signals were larger than the corresponding NIP signal, however, for some sensors not by much.
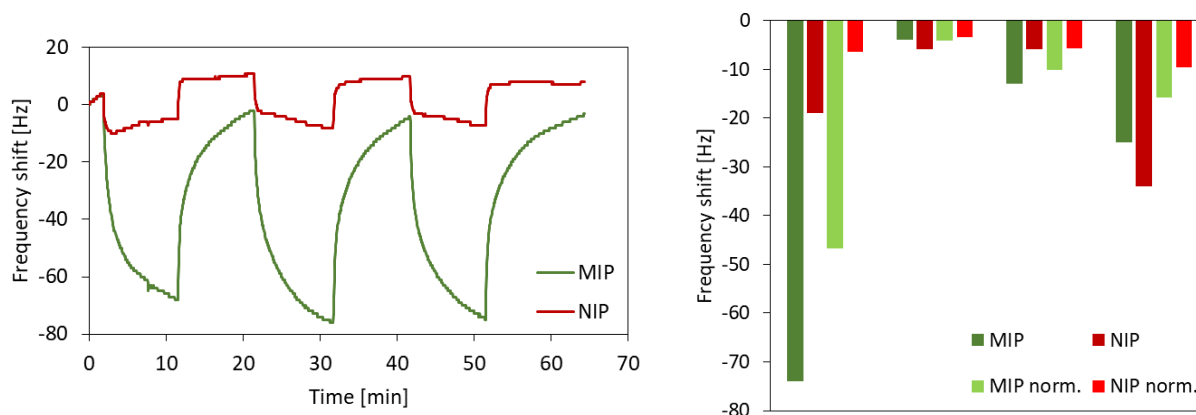
Figure 34: Left: Example of a QCM measurement. Right: Absolute and normalised frequency shifts of MIP and NIP electrodes of four sensors of the same batch. Normalised: Shift for 1000 ppm/100 nm polymer layer.

To further investigate the effect of adding the porogen at a later stage of synthesis, DPM was added in the last step to the diluted MIP and NIP solutions before spin-coating. 30 µL (= 5 v%) were added to the respective 1:30 dilution. As expected, the layer heights (Table 13) are close to the ones obtained with the original recipe.

Table 13: Average layer height of polymers prepared with 5 v% DPM in the 1:30 diluted MIP and NIP solutions on QCM. n=4.

	Average height [nm]	Standard deviation [nm]
NIP	53	22
MIP	56	14

Figure 35 shows an example of a QCM measurement as well as the average frequency shifts of MIP- and NIP-coated electrodes. In this case, adding a porogen did not increase the frequency shifts. The average MIP signal for 1000 ppm 2-propanol was 10 Hz. Even though the MIP-coated electrode in the depicted measurement shows a larger frequency shift than the NIP, the average MIP and NIP signals are not significantly different from one another. No correlation to the layer height was observed.

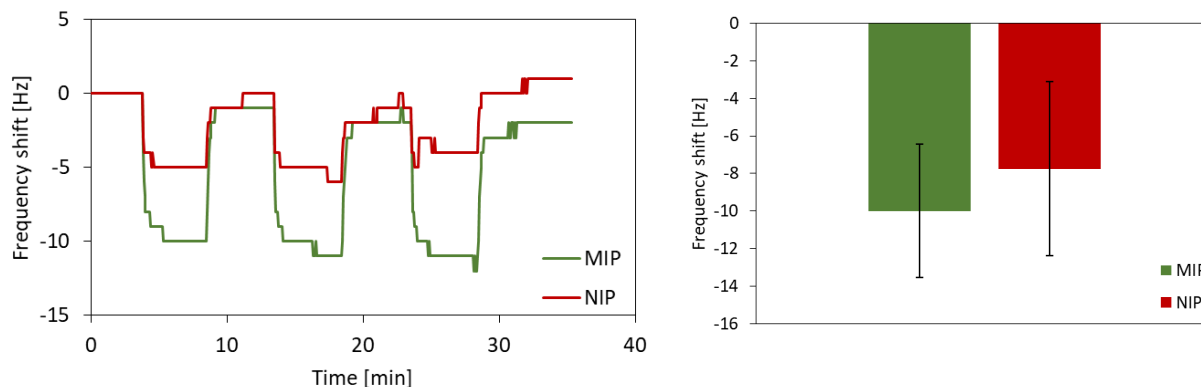*Figure 35: Example of a QCM measurement with a sensor coated with MIP and NIP containing 5 v% DPM in the 1:30 dilution and average frequency shifts. n=4.*

The experiments demonstrate that the optimal sensor responses result from adding 10 v% DPM into both MIP and NIP solutions before dilution and coating, resulting in absolute frequency shifts of up to -74 Hz in response to 1000 ppm 2-propanol. On the other hand, adding the porogen to either the initial stock solution or the diluted oligomer solutions is less effective, as it only leads to a maximum frequency shift of around -20 Hz for the same concentration.

4.1.4. Reducing the Amount of Template

The results from the previous sections make it evident, that the MIP layer is often thinner than the corresponding NIP, despite preparing them from the same stock solutions. The large amount of template in the MIP preparation may inhibit the polymerisation since the isocyanate can also react with 2-propanol instead of the polyol monomers. The following step thus was to reduce its amount and partly substitute it with the solvent THF.

Using a 1:1 (v/v) mixture of 2-propanol and THF as the solvent both during MIP synthesis and for diluting oligomer batches gives the following results: MIP and NIP solution, respectively, contained 50 µL DPM and lead to roughly the same average layer height (Table 14). With this composition average MIP and NIP layers have similar thicknesses. With only 2-propanol as solvent, MIP layers were often thinner, reaching sometimes only half the thickness of the corresponding NIP.

	Average height [nm]	Standard deviation [nm]
NIP	30	12
MIP	34	18

The sensor responses and average frequency shifts in Figure 36 reveal larger responses of the MIP-coated electrodes than the ones of the NIP-coated references. The signals obtained with the MIP-coated electrodes are on average 1.8 times higher than the ones of the NIP-coated electrodes suggesting imprinting even with less template.
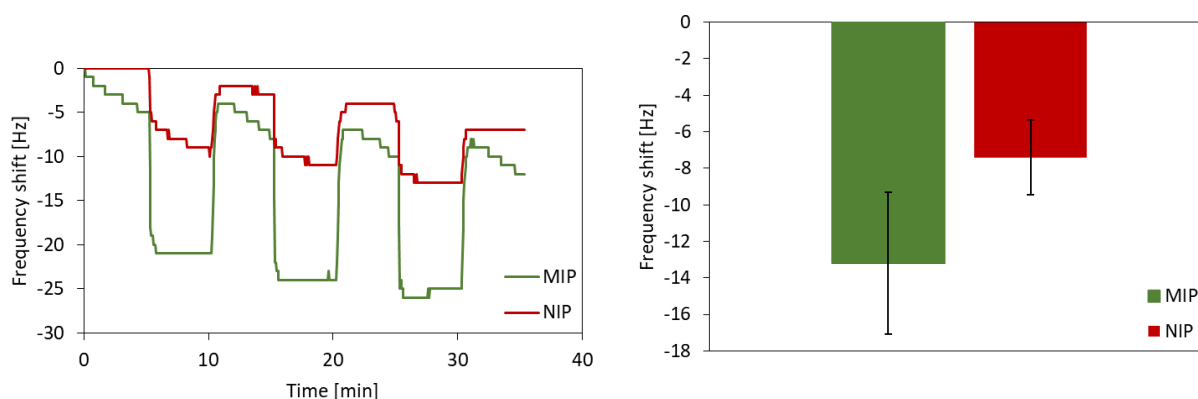
Figure 36: Example of a QCM measurement (left) and the average frequency shifts. n=5.

To find out if it is possible to imprint using even lower amount of template, an approach with a 1:2 (v/v) mixture of 2-propanol and THF as a solvent for the MIP was carried out using 50 µL DPM in MIP and NIP. This means, that the solvent mixture contained only one third of the initial amount of 2-propanol. In this case, the final dilution was again 1:30 with the same solvent mixture. Here the MIP layers are again rather thin as can be seen in Table 15.

	Average height [nm]	Standard deviation [nm]
NIP	50	11
MIP	18	4

Nonetheless, they exhibit good affinity towards the analyte with the absolute MIP signals being 1.4 times larger than the NIP signals as Figure 37 shows. Especially after normalising the signals to the same layer thickness, the average MIP signals are four times larger than NIP signals. However, they also have a larger standard deviation of 23 % of the average signal.
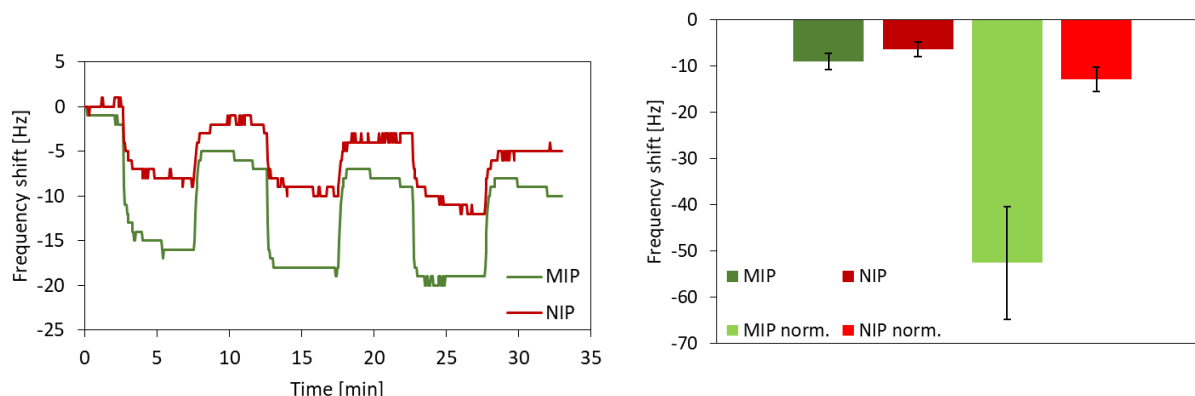
Figure 37: Example of a QCM measurement (left) and average frequency shifts including normalised signals for 1000ppm/100nm (right). n=3.

To obtain thicker layers, the MIP was 1:2 diluted with same solvent mixture (1:2 2-propanol/THF) instead of 1:30. This led to layers that were in fact thicker than desired as shown in Table 16.

Table 16: Average layer heights of MIP and NIP on QCM. n=4.

	Average height [nm]	Standard deviation [nm]
NIP	214	19
MIP	441	43

To make it easier to distinguish between MIP and NIP signals, the testing concentration was increased to 2000 ppm instead of 1000 ppm. In the example shown in Figure 38 the MIP signal is approximately twice as large as the NIP signal. By normalising to 100 nm polymer layer, the difference increases to a ratio of 1:5 (NIP:MIP). However, the other sensors do not show the same behavior. Their absolute signals are smaller in comparison ranging from -4 to -16 Hz and MIP and NIP signals are similar or NIP signals are even larger. When normalised to the layer height, all MIP-coated electrodes exhibit slightly larger frequency shifts than the corresponding NIPs. However, the difference is smaller reaching only factors of 1.2 to 1.8.
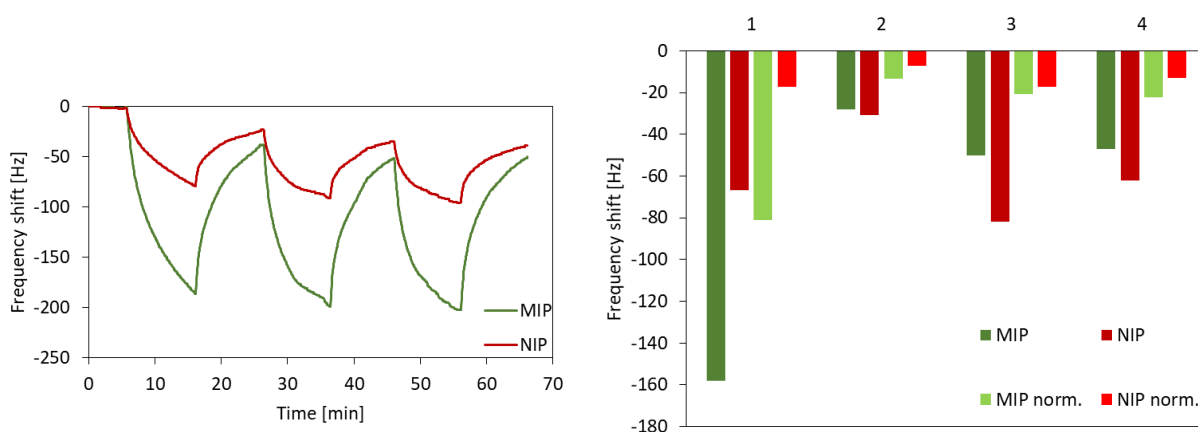
Figure 38: Example of a QCM measurement (left) and individual frequency shifts for 2000 ppm 2-propanol.

A different approach was using a 1:1 (v/v) mixture of 2-propanol and THF for preparing the MIP solution and diluting both MIP and NIP solution 1:30 with THF only. This further decreased the amount of 2-propanol in the final MIP dilution. The average layer heights of MIP and NIP are shown in Table 17.

Table 17: Average layer thickness of MIP and NIP on QCM. n=5.

	Average height [nm]	Standard deviation [nm]
NIP	50	24
MIP	33	9

The sensors of this batch on average show 1.8 times larger frequency shifts on the MIP-coated electrodes, which can be seen in Figure 39. Like the previous experiment, the use of less template for MIP preparation leads to sufficient imprinting effects reflected in higher MIP frequency shifts compared to the NIP-coated reference electrodes.
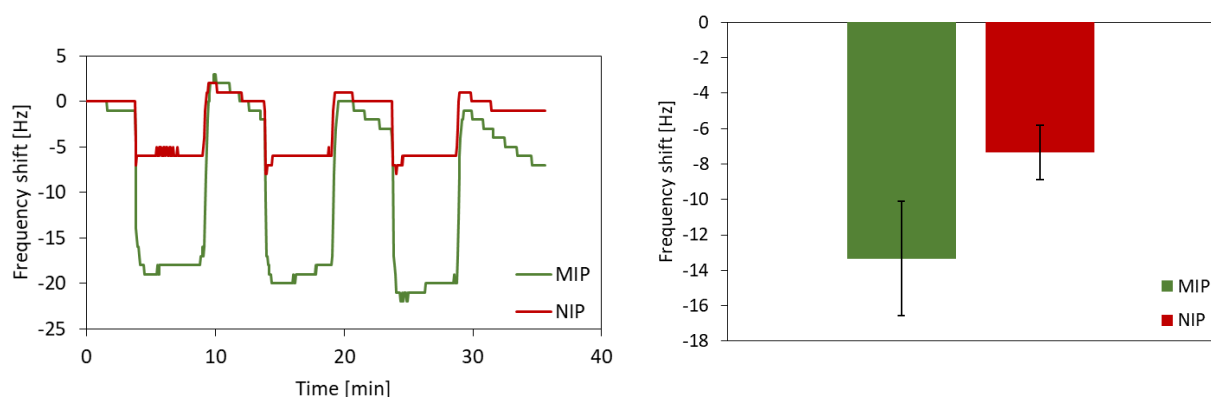
Figure 39: Example of a QCM measurement and average frequency shifts. n=3.

The same MIP and NIP solutions were also diluted 1:2 with THF only to obtain thicker layers. Table 18 presents the results.

Table 18: Average layer thickness of MIP and NIP on QCM. n=6.

	Average height [nm]	Standard deviation [nm]
NIP	205	139
MIP	125	54

In these measurements however, the frequency shifts of MIP and NIP coated electrodes show no difference. This is visible in Figure 40, which shows an example of a QCM measurement and the average sensor signals. This suggests that the dilution of the polymer plays a role in successful imprinting.
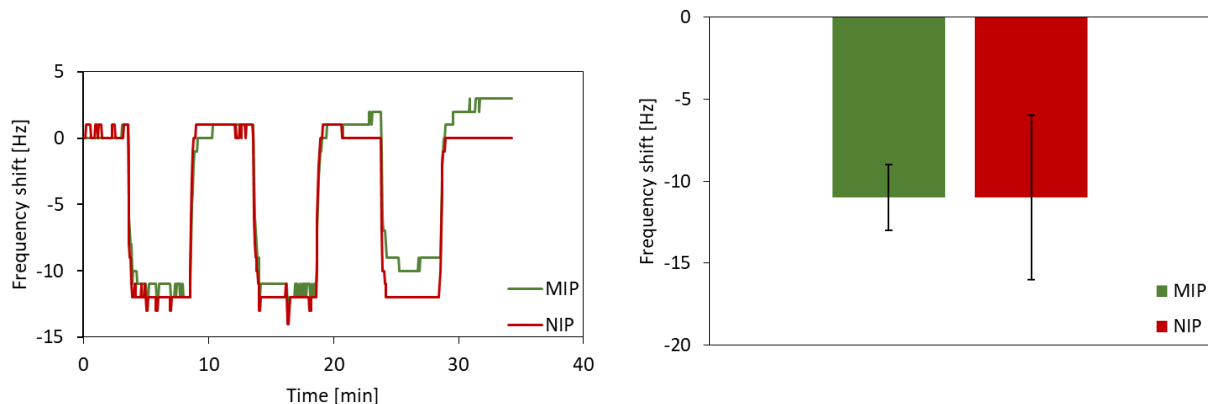
Figure 40: Example of a QCM measurement and average frequency shifts. n=4.

The experiments of this section show that using less template can in fact improve the polymerisation and imprinting. However, this is only true for diluted oligomer solutions, since the imprinting effect is partly lost when only diluting 1:2 instead of 1:10.

4.1.5. Conductive Blends

As diluting indeed improves sensor responses, it is of interest to generate conductive blends based on the recipe shown in the previous section prepared with 1:2 mixtures of 2-propanol and THF for both the MIP solution and the dilution. Even though the 1:10 diluted polymer showed better performance on the QCMs, the 1:2 dilution was used for blending since mixing the polymer with the P3HT stock solution further dilutes it anyway. Using the already diluted oligomer solutions would lead to very low amounts of the PU in the resulting blends. Table 19 shows the amounts of MIP/NIP solution and P3HT stock solution used to obtain the blend with the respective P3HT concentration. The P3HT content was calculated with respect to the total polymer mass on the QCM electrode.

Table 19: Volumes of MIP/NIP solutions and P3HT stock solution mixed to obtain the blends and the resulting P3HT content of the material.

MIP/NIP solution [µL]	P3HT solution (10 mg/mL) [µL]	P3HT [wt. %]
75	25	73.5
50	50	48.0
25	75	23.6

P3HT has dark purple colour. Dissolving in THF resulted in a dark reddish/purple solution. In contact with the diluted PU MIP and NIP solutions however, the colour drastically changed. This can be seen in Figure 41 which shows MIP and NIP blends containing 23.6 wt. % P3HT. All cNIP blends turned bright orange, which was never experienced with the acrylic polymers. In contact with the MIP solution the blend retained the purple colour. However, The P3HT seemed to quickly precipitate in the MIP solutions. The only difference between MIP and NIP in this case was 2-propanol which made up one third of the MIP solvent. Hence, this precipitation was most likely due to reduced solubility of P3HT in 2-propanol. Experiments to confirm this showed that P3HT is insoluble in 2-propanol and has only limited solubility in the 2-propanol/THF mixture.
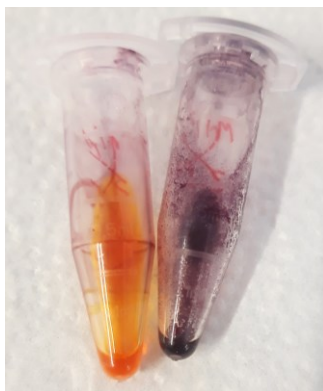
Figure 41: NIP (left) and MIP (right) solutions after blending with the P3HT stock solution. The blends shown contain 23.6 wt. % P3HT.

Nevertheless, the blends were coated onto QCMs and chemiresistors. Table 20 shows the average layer heights on QCM. One can see that all layers exceed the optimum range of layer height. It is also noteworthy that the layer height increases with P3HT content. P3HT increases the viscosity of the blend which could be observed during spin-coating. It is noticeable that the MIP layers with the highest P3HT content have more than double the thickness of the corresponding NIP. This can be explained by the precipitation mentioned earlier.

P3HT [wt. %]		Average height [nm]	Standard deviation [nm]
23.6	cNIP	749	466
	cMIP	416	177
48.0	cNIP	899	449
	cMIP	1161	286
73.5	cNIP	545	204
	cMIP	1829	310

QCM Measurements

Even though the layers were too thick for actual application, all QCMs were exposed to four different concentrations of 2-propanol vapour, namely 1000-1500-2000-2500 ppm in dry air while recording the corresponding frequency shifts.

Figure 42 shows a QCM measurement with the abovementioned 2-propanol concentrations on a QCM sensor coated with the blends containing 23.6 wt. % P3HT. Depicted next to it are the average signals for 1000 ppm of the analyte. As can be seen, the absolute frequency shifts of cMIP- and cNIP-coated electrodes are the same. The graph also shows signals for 1000 ppm normalised to 100 nm polymer layer. After normalisation, there is a difference between MIP and NIP. However, it is not ideal to normalise for such thick layers, because the analyte will most likely not diffuse all the way to through the polymer. Thus, one cannot assume a linear signal increase with increasing layer height.
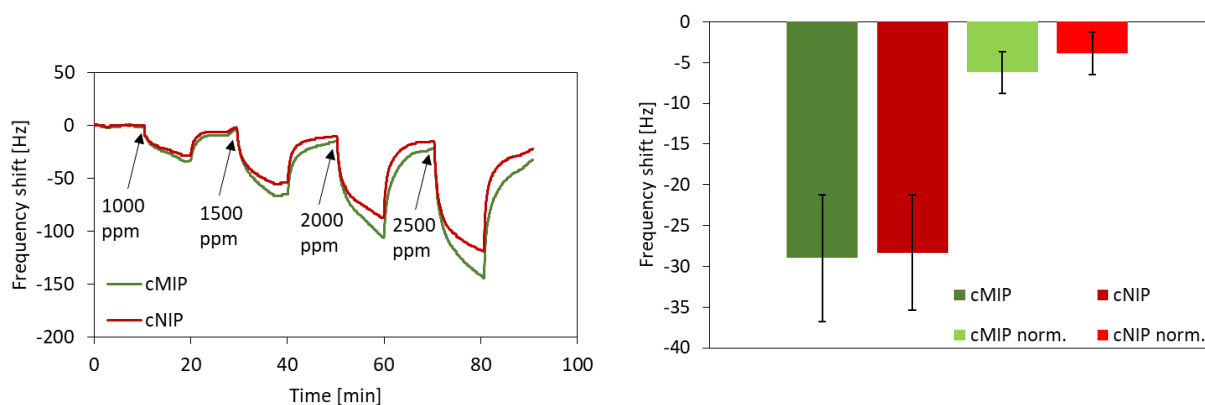
Figure 42: Example of a QCM measurement with a QCM coated with the blends containing 23.6 wt. % P3HT and average frequency shifts of the batch including normalised shifts for 1000 ppm/100 nm. n=3.

Figure 43 shows the same experiments conducted with QCMs coated with blends containing 48.0 wt. % P3HT. Here the cMIP signals are significantly larger than the cNIP signals. Since only two sensors could be measured from this batch, no average signals are provided.
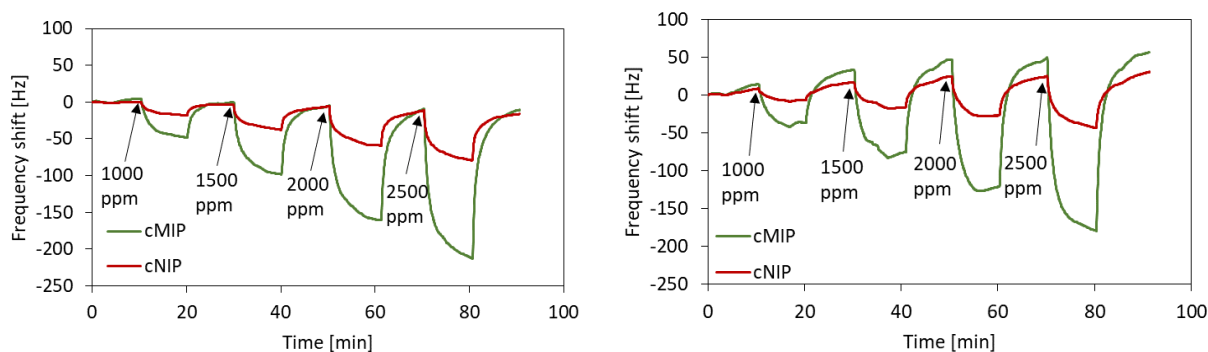
Figure 43: Two QCM measurements with various 2-propanol concentrations. Sensors coated with blends containing 48.0 wt. % P3HT.

Figure 44 depicts an example of a measurement with blends containing 73.5 wt. % P3HT and the average frequency shifts of sensors from this batch. In this batch, the difference in frequency shift between cMIP and cNIP is even more pronounced with cMIP signals being five times larger.
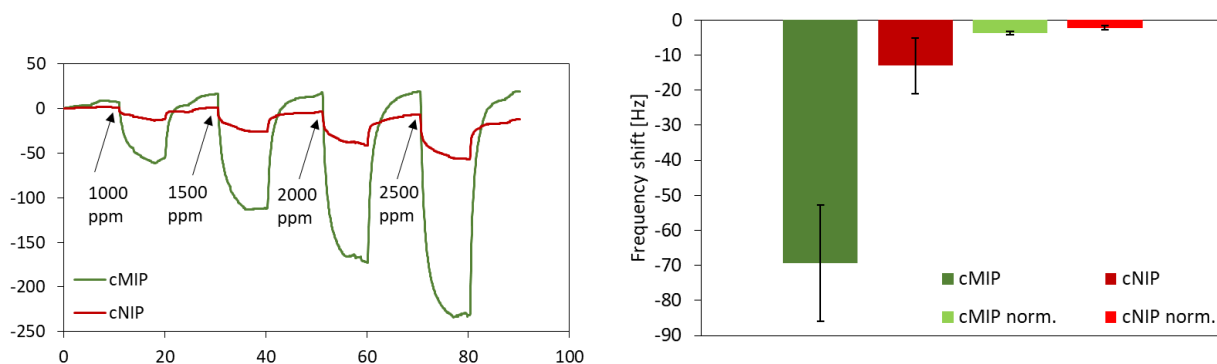
Figure 44: Example of a QCM measurement and average frequency shifts of QCMs coated with the blends containing 73.5 wt. %. n=3.

Additionally, selectivity tests were performed. Figure 45 shows examples of selectivity testes with 1000 ppm of n-heptane and heptanal respectively.
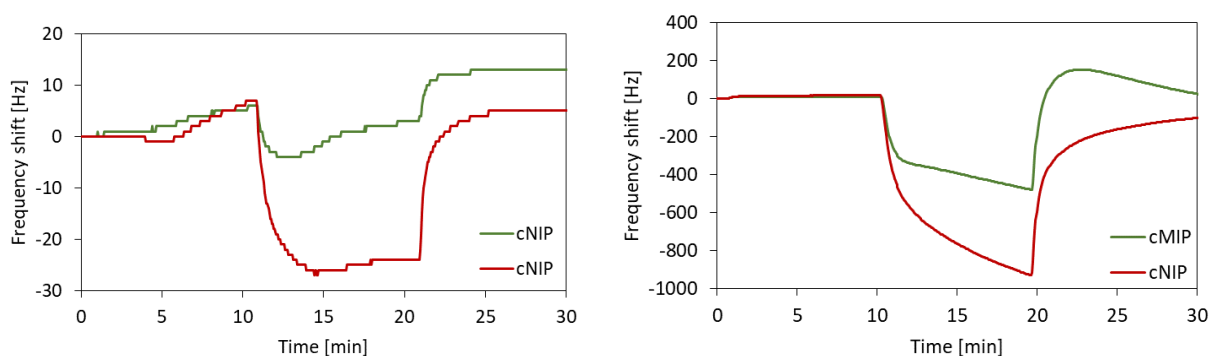
Figure 45: Selectivity test with 1000 ppm n-heptane (left) and 1000 ppm heptanal (right) on a QCM coated with the blends containing 23.6 wt. % P3HT.

In both cases, the cNIP-coated channel responds more strongly to the VOC. In the case of n-heptane the frequency shift is in a reasonable range around -30 Hz. In the case of the heptanal measurement however, the cNIP frequency decreases as much as -1000 Hz which is unlikely due to the mass of gas molecules adsorbed. A similar behaviour with very strong frequency shifts is experienced when testing the blends with higher P3HT contents with heptanal and 1-butanol (Figure 46). However, here the cMIP coated channels show the larger frequency shifts. The sensors show responses of -1277 Hz and -892 Hz to 1000 ppm heptanal and 1-butanol respectively. The same sensors showed responses of -71 and -48 Hz to 1000 ppm 2-propanol.
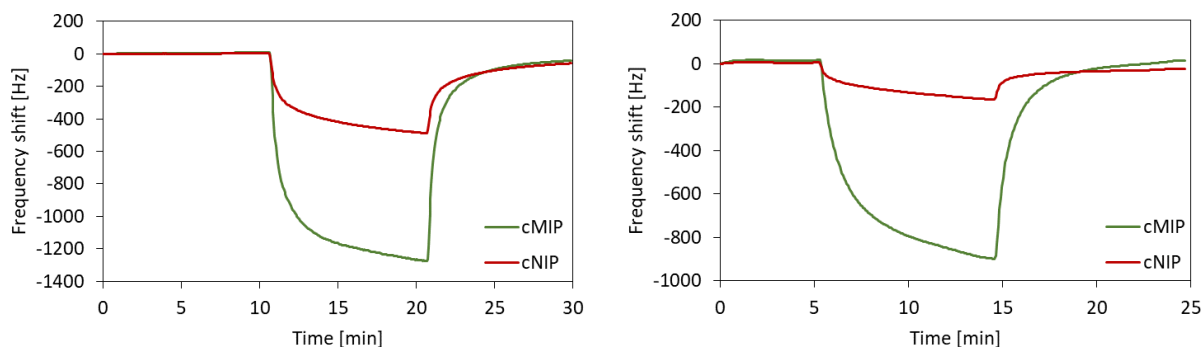
Figure 46: Left: Selectivity test with 1000 ppm heptanal on a QCM coated with blends containing 48.0 wt. % P3HT. Right: Selectivity test with 1000 ppm 1-butanol on a QCM coated with blends containing 73.5 wt. % P3HT.

This suggests that there are other factors that influence the frequency shift. One reason may be the thick polymer layers, since they most likely are not completely rigid. Interestingly, even in the selectivity tests the cMIPs with higher P3HT content show more affinity towards the VOC than the corresponding cNIPs. This could be a result of increased surface roughness of the cMIP layers resulting from P3HT precipitation. Additionally, one must keep in mind, that the cMIP layers are thicker than the cNIP layers and thus are more prone to unspecifically adsorbing gas molecules. However, the tests suggest that the QCM sensors in their current form are not selective for 2-propanol since the frequency shifts obtained with other VOCs are larger than the ones obtained with the same concentration 2-propanol on the same sensors.

Chemiresistor Measurements

Chemiresistors coated with the cMIP blends were exposed to the same sequence of 2-propanol concentrations as the QCMs, meaning 1000-1500-2000-2500 ppm. In between the cell was flushed with clean air. Figure 47 shows the results obtained with sensors coated with cMIP blend containing 23.6 wt. % P3HT. The following section shows all data after noise reduction (rolling average of 20 data points) and baseline drift correction.
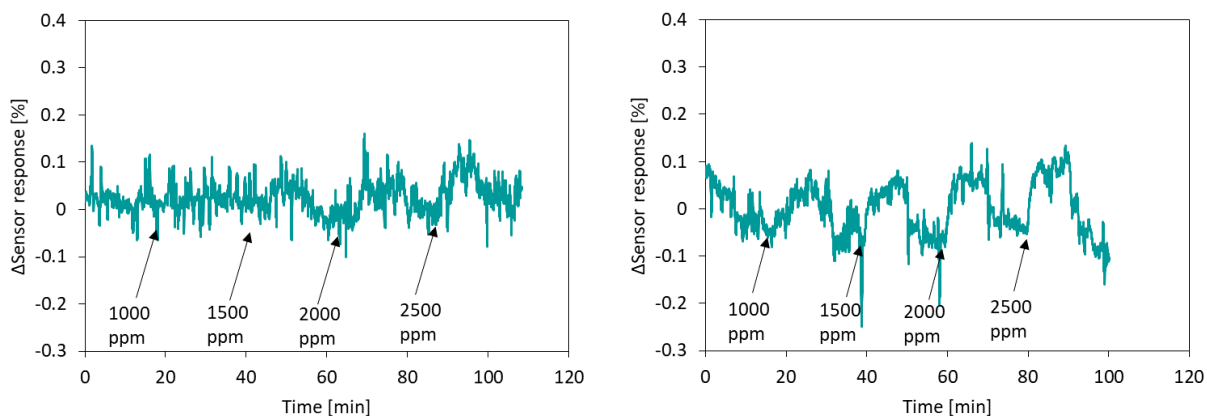
Figure 47: Chemiresistor measurements with sensors coated with cMIP blend containing 23.6 wt. % P3HT.

The measurements of the sensors coated with blends containing 23.6 wt. % P3HT differ from one another. One of the sensors only shows a detectable change in resistance at 1500 ppm and above, with the response to the highest concentration being 0.128 %. The second sensor shows a clear response of 0.111 % at 1000 ppm. To show the differing behaviour, Figure 48 shows the sensor responses plotted against the concentration. As three sensors were prepared for each batch, they were named A, B and C to identify them. Responses of sensors B and C are depicted below. Sensor A could not be measured due to insufficient covering of the IDEs with the blend.
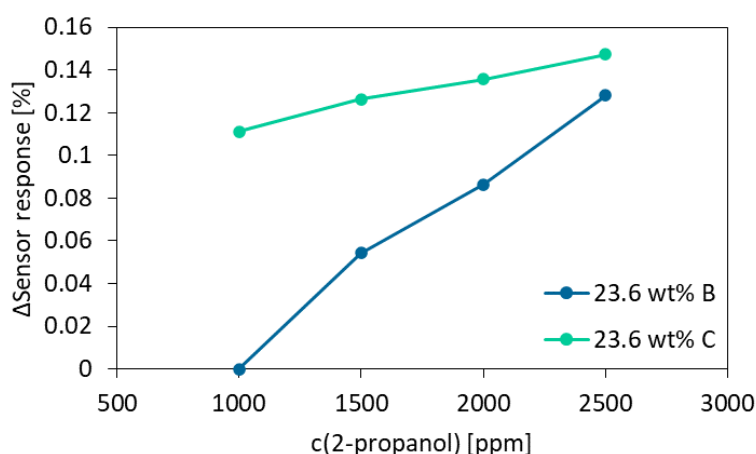
Figure 48: Sensor responses of the chemiresistors coated with cMIP blends containing 23.6 wt.%.

61

While sensor C starts out with higher responses its slope is less steep than the one of sensor B. At the highest concentration, the responses are similar to one another. As mentioned above, due to failure of the third sensor of the batch only two measurements are available. From this, no clear statement can be made.

The sensors coated with the blends containing higher amounts of P3HT showed reversible responses over the entire concentration range which can be seen in Figure 49.
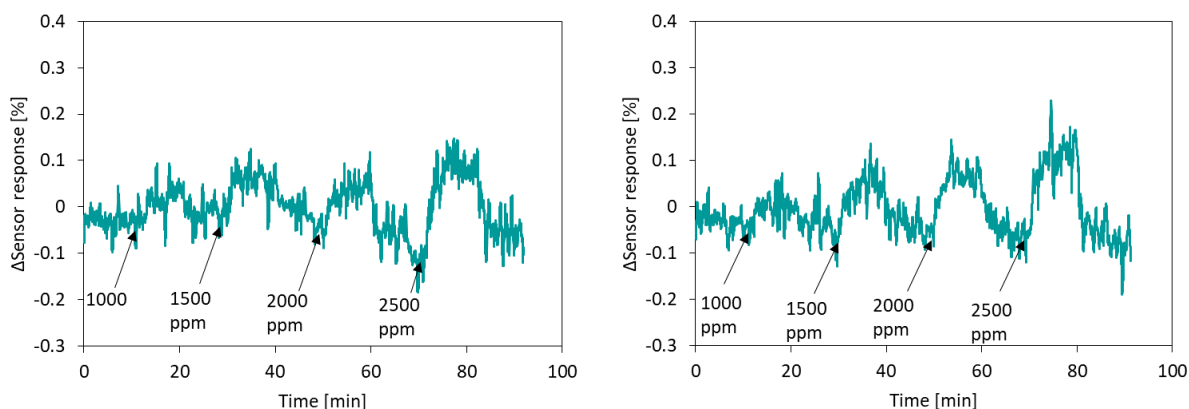
Figure 49: Examples of chemiresistor measurements with sensors coated with cMIP blends containing 48.0 (left) and 73.5 wt. % P3HT (right).

Figure 50 summarises the results of all measurements with chemiresistors coated with 48.0 wt. % and 73.5 wt. % blends. The average signals obtained with the 73.5 wt. % blends are higher than the ones of the 48.0 wt. % blends. Since all sensors from this batch showed a similar response at 1000 ppm, the error bar is not visible in the plot. The signals for 1500 and 2000 ppm show the largest standard deviation. The resistors coated with the 48.0 wt. % blend show smaller responses. However, they exhibit smaller deviations between the sensors of the batch. In both cases the average signal increase is not perfectly linear. The correlation coefficients are 0.9092 for 48.0 wt. % P3HT and 0.9287 for 73.4 wt. % P3HT respectively.
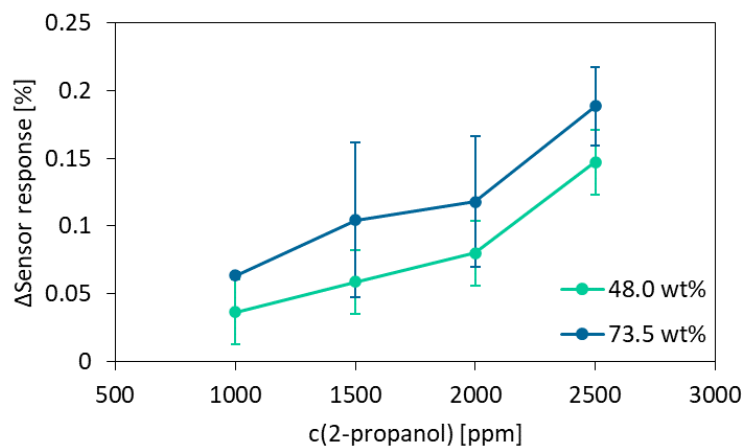
Figure 50: Average sensor responses of the chemiresistors coated with cMIP blends. n=3.

Figure 51 depicts the results of the selectivity tests performed on all sensors with 1000 ppm 1-butanol. Interestingly all sensors exhibited an irreversible sensor response when tested with 1-butanol. While 1-butanol was lead through the measuring cell, the sensor response of the polymers steadily increased. When the cell was flushed with clean air, the signal remained at the level that it had reached until then.
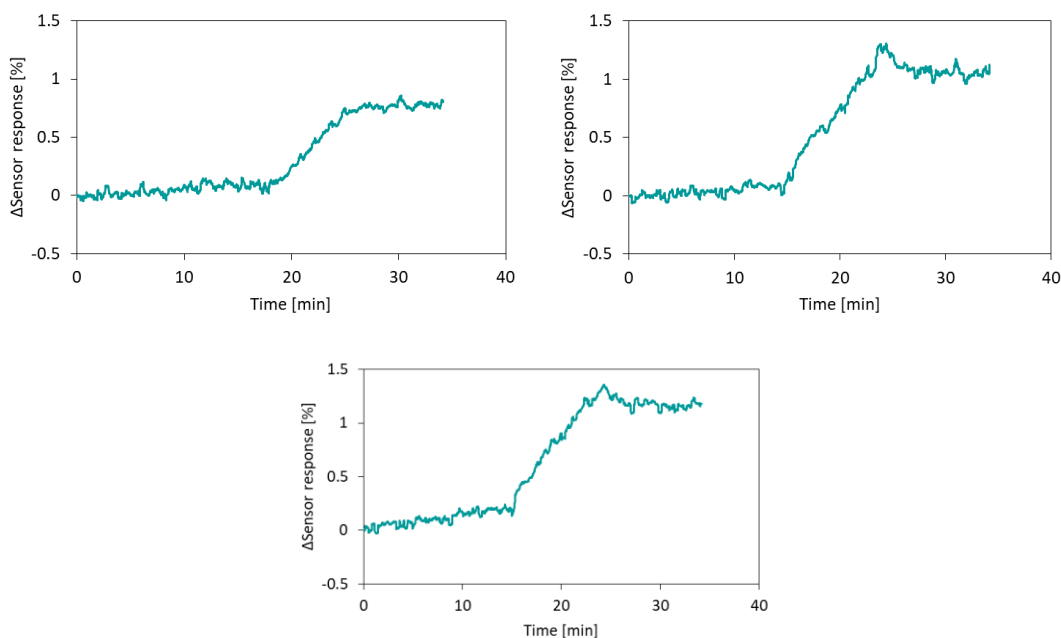
Figure 51: Selectivity test with 1000 ppm 1-butanol on chemiresistors coated with cMIP blends containing 23.6 wt. % (top left) 48.0 wt. % (top right) and 73.5 wt. % P3HT (bottom).

4.1.6. Surface Characterisation

Light Microscope

The polymer layers were characterised using various methods. Of those, light microscopy is the simplest way to observe the surface of the material. Figure 52 shows images of a PU MIP and NIP surface on QCM electrodes. Both MIP and NIP form homogeneous thin films over the whole area of the respective electrodes. Pores in the micrometre range can be seen in both materials, which is beneficial for analyte diffusion. For better comparison is important that MIP and NIP, apart from the imprints, have similar surface roughness, which seems the case for these materials.
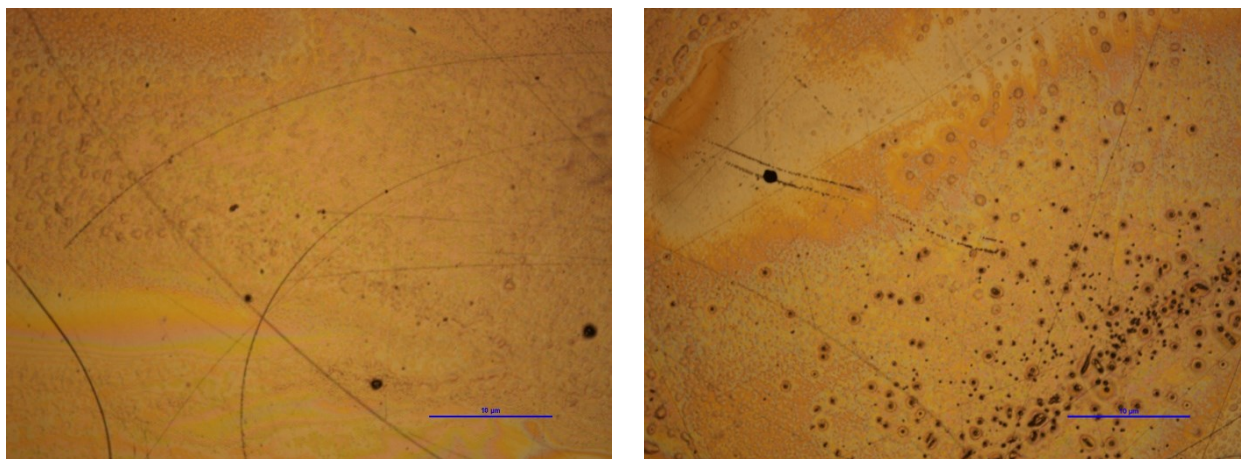
Figure 52: Light microscope images of the PU MIP (left) and NIP (right) surfaces. Scale bar: 500 μm.

The blends were also examined in the microscope. Figure 53 -Figure 55 show images of MIP and NIP blends of all prepared compositions. Precipitates can be seen in the MIP blends. This corresponds to the observations made when preparing the composites: P3HT precipitates in 2-propanol. The amount of precipitate decreases with the P3HT content in the blends. The NIPs on the other hand mix better with the P3HT solution and result in smoother layers.
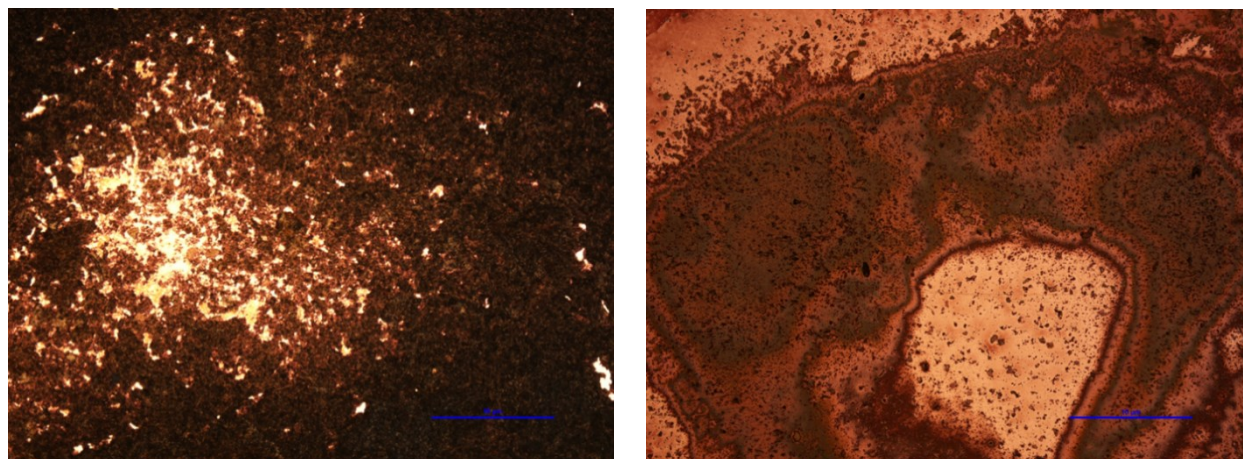
Figure 53: Light microscope images of the cMIP (left) and cNIP (right) blends containing 73.5 wt. % P3HT. Scale bar: 500 μm.
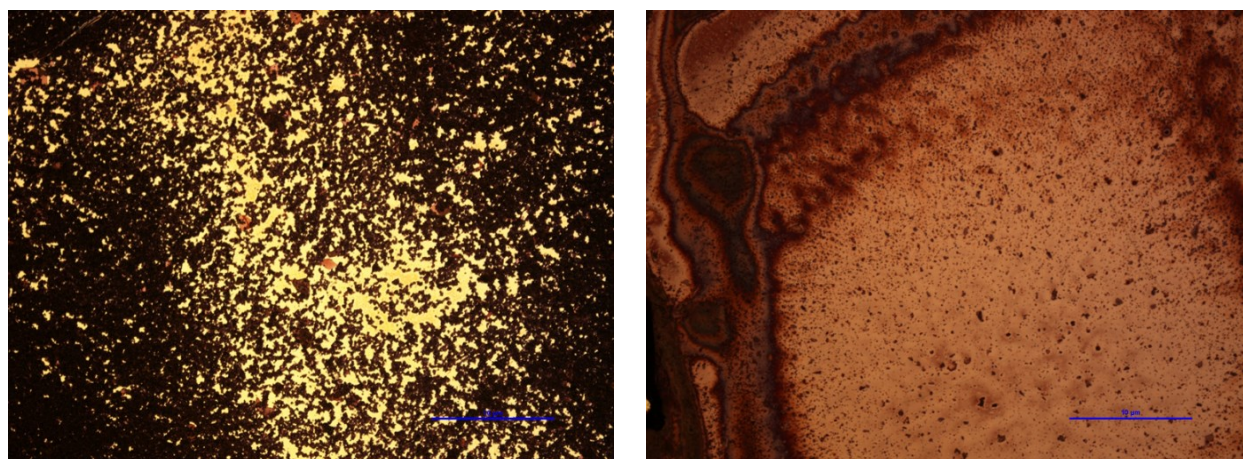
Figure 54: Light microscope images of the cMIP (left) and cNIP (right) blends containing 48.0 wt. % P3HT. Scale bar: 500 μm.
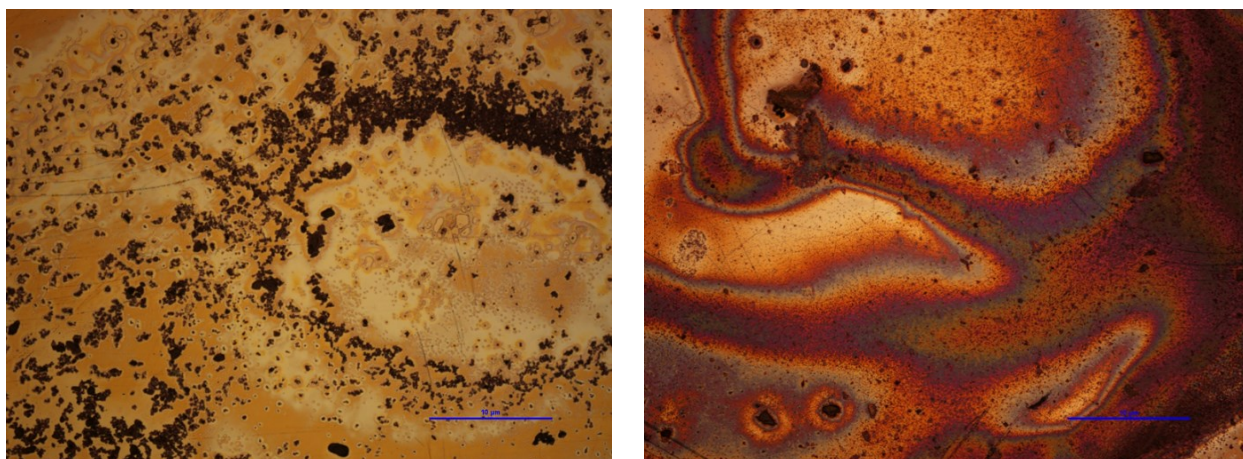
Figure 55: Light microscope images of the cMIP (left) and cNIP (right) blends containing 23.6 wt. % P3HT. Scale bar: 500 μm.

Figure 56 shows microscope images of the conductive blends on chemiresistors. The precipitates are also visible on the chemiresistors. With increasing P3HT content in the blends one can achieve a more homogeneous coating and connection between the IDEs.
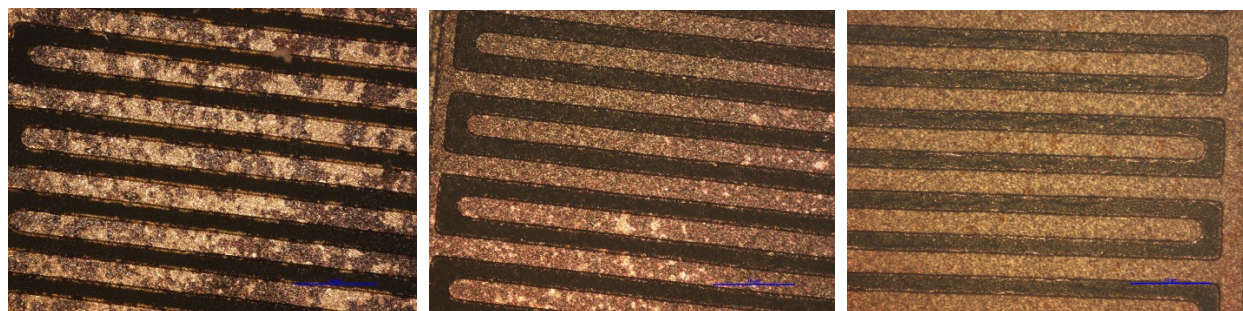
Figure 56: cMIPs on chemiresistors. Left to right: 23.6-48.0-73.5 wt. % P3HT. Scale bar: 500 μm.

AFM

Both non-conductive MIP and NIP as well as cMIP and NIP containing 73.5 wt. % P3HT were analysed with atomic force microscopy (AFM). This allows for making smaller features on the polymer films visible. Figure 57 shows images of the non-conductive PU layers. The AFM images of the MIP show a smooth surface with few irregular pores. In the bottom right corner, an area which is significantly higher than the rest of the image appears in brighter colour. This can either be a clump of polymer or simply dirt from storing the sample. The image of the NIP shows a more porous polymer than the MIP in the scanned area.
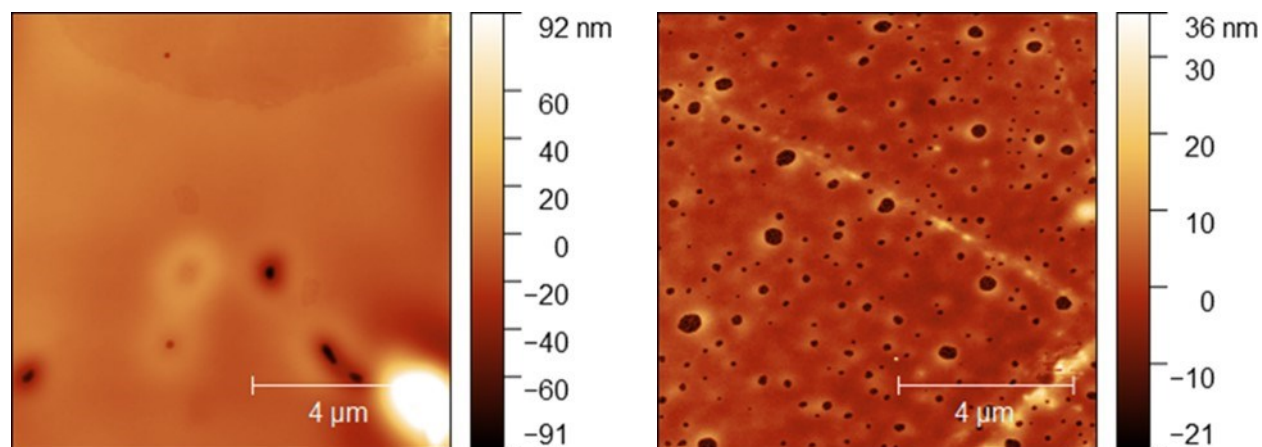
Figure 57: AFM images of the PU MIP (left) and NIP (right) surfaces.

Figure 58 shows AFM images of blends containing 73.5 wt. % P3HT. The conductive composites appear less smooth in comparison to the PU thin films. However, one must take into account that the samples shown in the images above contain more P3HT than PU. As mentioned before, P3HT partly precipitated in contact with the PU solutions, which may cause the roughness of the deposited thin film.
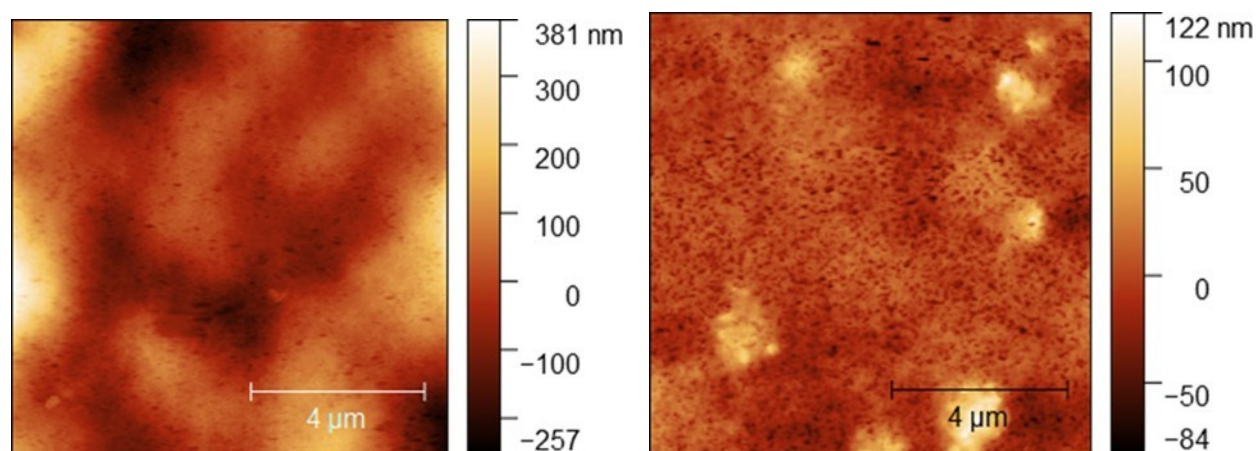
Figure 58: AFM images of the cMIP (left) and cNIP (right) blends containing 73.5 wt. % P3HT.

SEM and EDX

Some samples were also analysed with SEM. Figure 59-Figure 61 show the results. With increasing P3HT content the overall surface appears to get rougher. However, when zoomed in, regular pores can only be observed in the blend containing 23.6 wt. % P3HT. This suggests that the pores are formed in the PU while P3HT promotes the formation of more homogeneous layers.
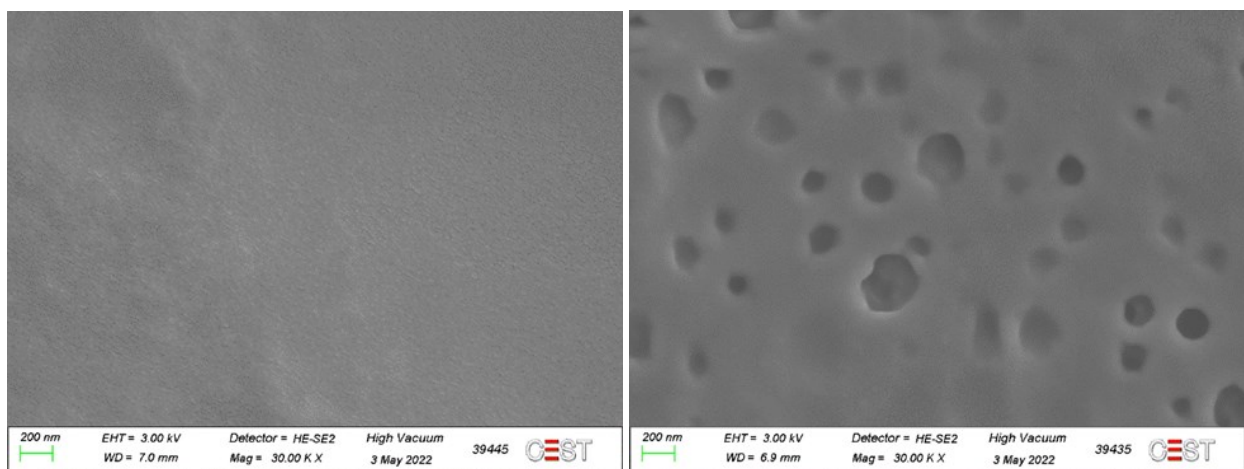
Figure 59: SEM images of the cMIP (left) and cNIP (right) blends containing 23.6 wt. % P3HT.
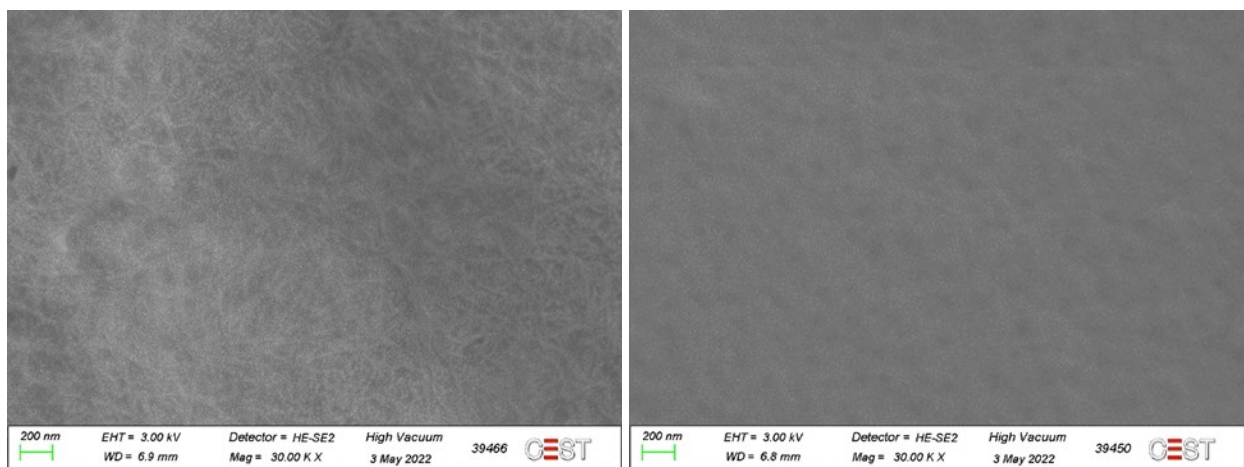
Figure 60: SEM images of the cMIP (left) and cNIP (right) blends containing 48.0 wt. % P3HT.
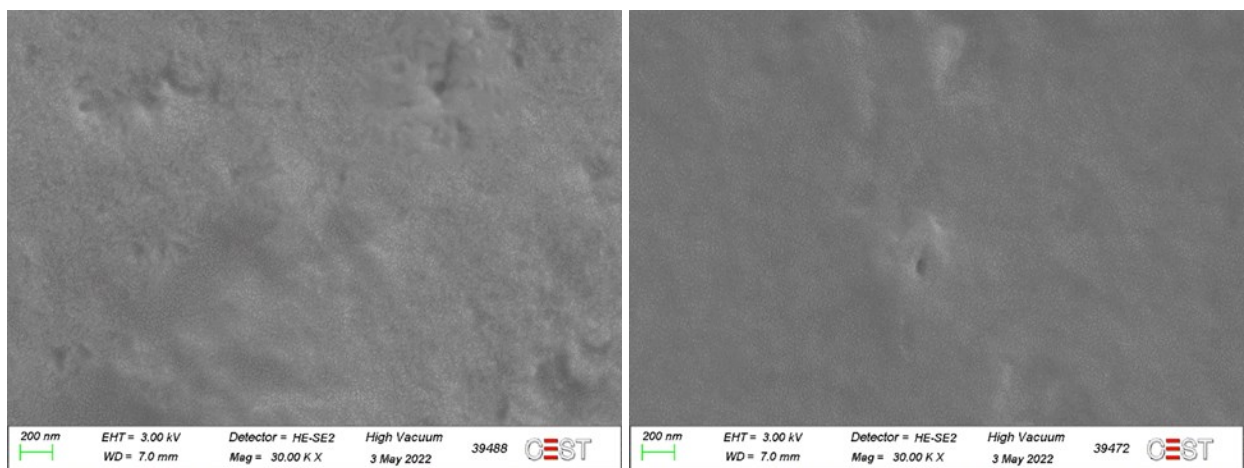
Figure 61: SEM images of the cMIP (left) and cNIP (right) blends containing 73.5 wt. % P3HT.

On some samples, small, sharp pieces appeared to stick out of a rather smooth surrounding area. Those may be pieces of undissolved P3HT. To confirm this, EDX was performed of an area without those pieces and on several spots directly on the pieces. Figure 62 shows an SEM image of the sample surface with the probed area (yellow rectangle) and spots (circles with blue labelling) indicated.
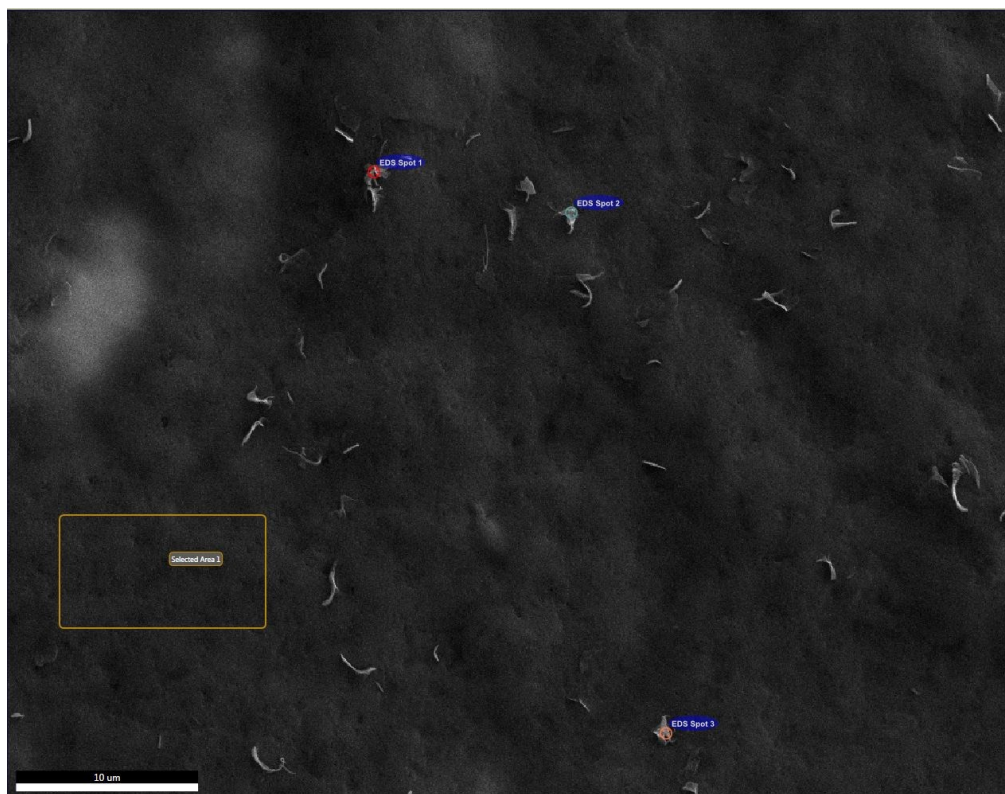
Figure 62: QCM 33 cMIP 73.5 wt. % P3HT. Scale bar: 10 µm.

The results of the elemental composition are shown in Table 21. Against the expectations, the spots on the solids did not contain significantly more sulfur than the smooth area. They could be covered with the polymer blend ad thus the signal is the same as in the surrounding material. It is also possible that they are dirt on the surface.

Table 21: EDX results of the probed area and spots.

	Element	Weight %	Atomic %
Area 1	C K	81.7	95.2
	O K	1.1	1
	Au M	10	0.7
	S K	7.2	**3.1**
Spot 1	C K	75.2	96.2
	O K	0.5	0.5
	Au M	20.7	1.6
	S K	3.6	**1.7**
Spot 2	C K	80.3	94.6
	N K	0.1	0.1
	O K	1.8	1.6
	Au M	11.3	0.8
	S K	6.6	**2.9**
Spot 3	C K	74.3	93
	O K	3.3	3.1
	Au M	16.8	1.3
	S K	5.6	**2.6**

4.2. Heptanal

4.2.1. Original Procedure

The starting point for developing the heptanal MIP was a publication of the group in which imprinted MAA-*co*-EGDMA thin films were used for detecting small molecules on QCM. [151] First, the MIP for the template heptanal and a corresponding NIP were prepared according to the published procedure described in the experimental section. As washing with the described solvent mixture removed almost the entire polymer layer, the template was instead removed via evaporation. For this, the sensors were placed in a drying cabinet at 80°C until the resonance frequency of the QCM did not increase further due to evaporation. Table 22 shows the calculated layer heights after drying.

	Average height [nm]	Standard deviation [nm]
NIP	81	36
MIP	97	46

To test the sensor responses, they were exposed three times to 1000 ppm heptanal in dry air. In between the cell was flushed with clean air. The total gas flow was kept constant at 3 L/min. Figure 63 shows that the frequency shifts of the MIP-coated electrode in general exceed the ones of the NIP-coated electrodes by a factor of roughly 1.7. However, the sensors show different absolute frequency shifts for the same analyte concentration, suggesting poor reproducibility of the sensor responses. No correlation of the sensor response with layer height was observed.
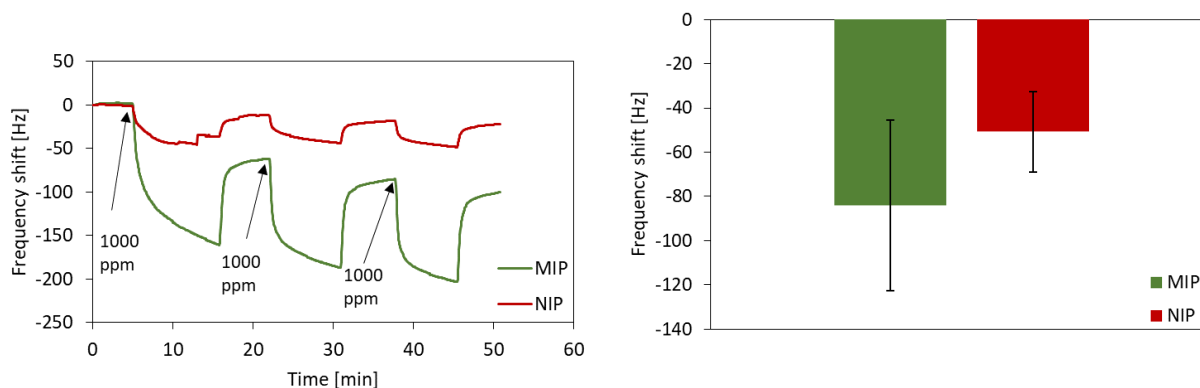
Figure 63: Example of a QCM measurement (left) and average frequency shifts for 1000 ppm heptanal (right) of QCMs coated with MAA-co-EGDMA MIP and NIP. n=4.

Since heptanal has a rather high boiling point at 153°C, the evaporation temperature was increased from 80°C to 150°C to ensure template removal. Table 23 shows the average layer thickness of MIP and NIP after drying.

	Average height [nm]	Standard deviation [nm]
NIP	101	41
MIP	59	40

As can be seen in Figure 64, this, in general, leads to smaller frequency shifts than polymers dried at 80°C. The individual signals of the sensors again differed for the same concentration ranging from -16 to -57 Hz for 1000 ppm heptanal. No correlation to the layer height was observed. On average MIP signals are larger than NIP signals by a factor of 1.6. However, the error bars overlap.
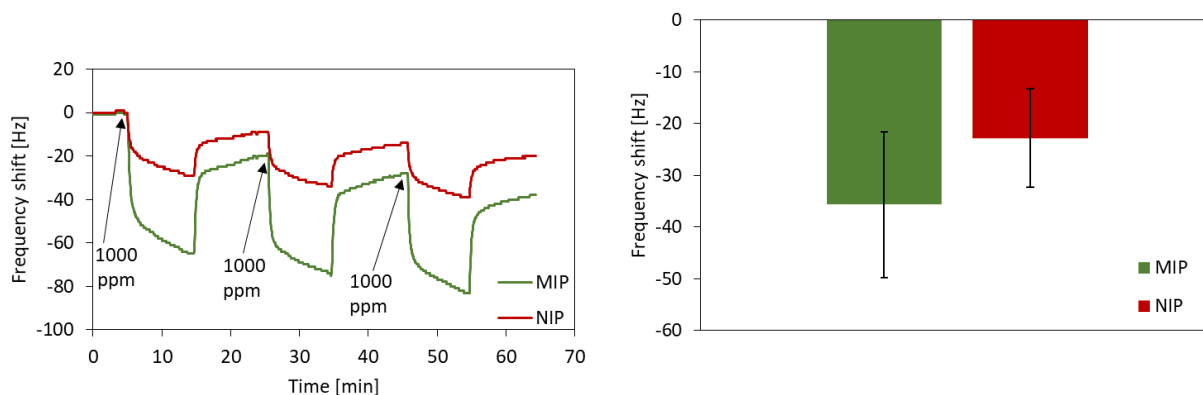
Figure 64: Example of a QCM measurement (left) and average frequency shifts for 1000 ppm heptanal (right) of QCMs coated with MAA-co-EGDMA MIP and NIP. n=6.

4.2.2. Monomers

To further optimise the sensor responses, other acrylamide-based monomers were assessed instead of MAA. The idea behind this was to increase the interaction with the aldehyde with amide groups in the monomers. The molar ratio of all components and all other parameters were retained. For the first experiment, 12.5 mg acrylamide (AA) were used instead of MAA.

The layers obtained with AA-*co*-EGDMA (Table 24) are thicker than the ones previously obtained with MAA but still in a useful range.

	Average height [nm]	Standard deviation [nm]
NIP	228	186
MIP	138	52

Figure 65 shows the results of tests of the polymer on QCM with 1000 ppm heptanal. The frequency shifts of the MIP coated electrodes of the QCMs are both in the range of -50 Hz, while the NIP signals are significantly smaller in both cases.
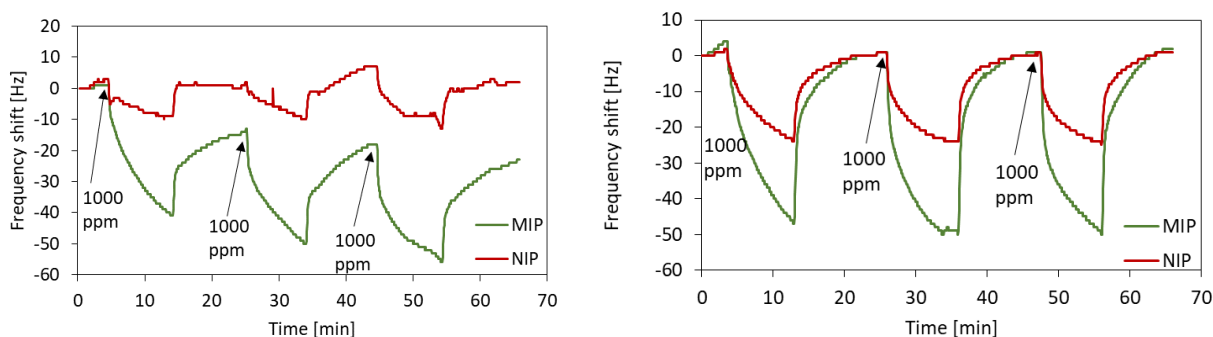
Figure 65: QCM measurements with AA-co-EGDMA MIP and NIP.

Even though the results are satisfactory, there were concerns that the unsubstituted amine could react with the aldehyde causing it to be irreversibly bound in the polymer layer. Therefore, it was exchanged for other monomers with substituted amine groups. N-Isopropylacrylamide (NIPAM) for example, has one isopropyl group attached to the nitrogen. 20 mg NIPAM were used while the rest of the procedure remained unchanged. The average layer heights are presented in Table 25. The layers prepared with NIPAM have an average thickness of almost 1 µm, which is too high for QCM sensing. Furthermore, the standard deviation of the layer heights is extremely high, meaning that it is problematic to obtain reproducible layer heights.

	Average height [nm]	Standard deviation [nm]
NIP	866	941
MIP	926	887

Figure 66 shows the results of tests with both sensors showing approximately the same response on both electrodes when tested with 1000 ppm heptanal. There is no indication for successful imprinting. The isopropyl substituent could impede the interaction with the template due to steric hindrance. This monomer is not suitable for this application.
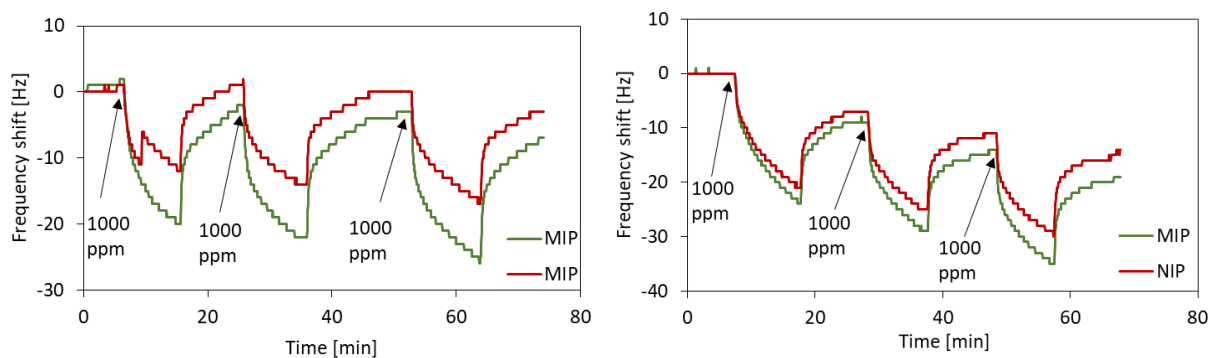
Figure 66: QCM measurements with NIPAM-co-EGDMA MIP and NIP.

DMAA was chosen as a potential alternative. The acrylamide has two methyl groups attached to the amine group that should prevent irreversible reactions with the aldehyde while still being small enough to allow for interacting with the template. 18 µL DMAA were used in the otherwise unchanged procedure. Table 26 presents the obtained layer heights which are in the desired range.

	Average height [nm]	Standard deviation [nm]
NIP	128	16
MIP	137	56

The sensor signals for 1000 ppm heptanal can be seen in Figure 67. The larger frequency shifts on the MIP-coated electrodes suggest successful imprinting. However, the magnitudes of the frequency shifts of the measuring electrodes vary between -34 and -65 Hz. Since all polymer layers are in the same thickness range around 130 nm, normalising the signals to 100 nm does not change the results drastically.
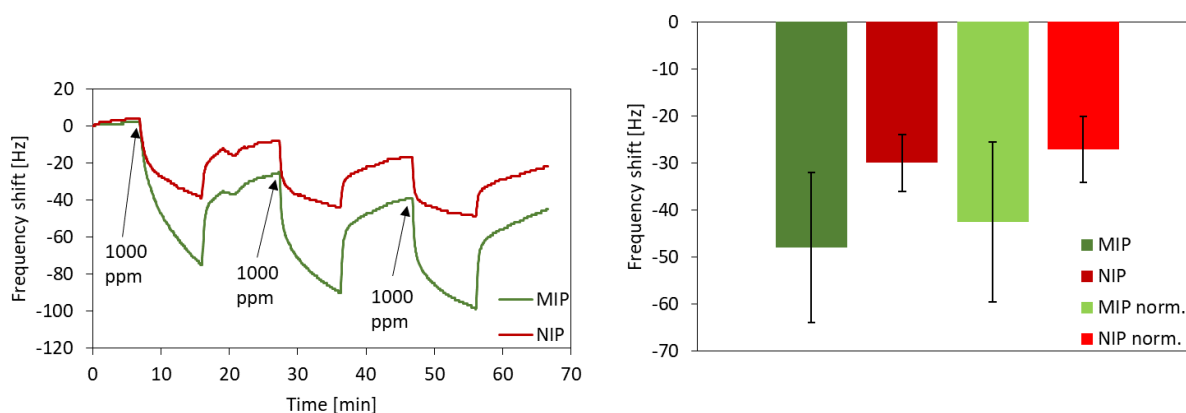
Figure 67: Example of a QCM measurement (left) and average absolute and normalised frequency shifts. n=3.

Overall, switching from MAA to DMAA increased the average MIP response for 1000 ppm heptanal from -36 to -48 Hz while the imprinting factor remained constant at 1.6.

4.2.3.   Conductive Blends

For the P3HT blends, switching to a different solvent was necessary since DMSO cannot dissolve the conductive polymer. Several solvents were tested, namely heptanal, n-heptane, acetonitrile, acetone, toluene, dimethylformamide and 1,4-dioxane. Although they could dissolve all components, the growing polymer started to precipitate in most of them shortly after initiation. Ultimately, THF was chosen.

Switching to THF also brings other advantages. It has a lower boiling point than DMSO, meaning it evaporates better from the polymer layers. This also means that there is less influence on damping, from solvent residues in the polymer. In this approach, the QCMs are coated on both sides of the sensor. Table 27 shows the combined layer height of the non-conductive control polymers coated on both sides of the QCMs. Naturally, after double-sided coating, the layers are thicker than in the previous experiments.

Table 27: Average layer heights of the DMAA-co-EGDMA MIP and NIP in THF on QCM. n=4.

	Average height [nm]	Standard deviation [nm]
NIP	266	23
MIP	303	116

Figure 68 shows the results of measurements of the sensors at different concentrations of heptanal (500-1000-1500-2000 ppm). This measurement suggests successful imprinting as the MIP-coated electrode responds significantly stronger than the reference electrode. Furthermore, the MIP signals depend on concentration. However, similar results to this measurement were only obtained with one other sensor. The absolute frequency shifts of both measurements, sensor 2 and 4 of the batch, are depicted below. Both sensors show similar responses and linear behaviour of the MIP signals over the whole concentration range. Regression coefficients are 0.9906 for sensor 2 and 0.9836 for sensor 4.
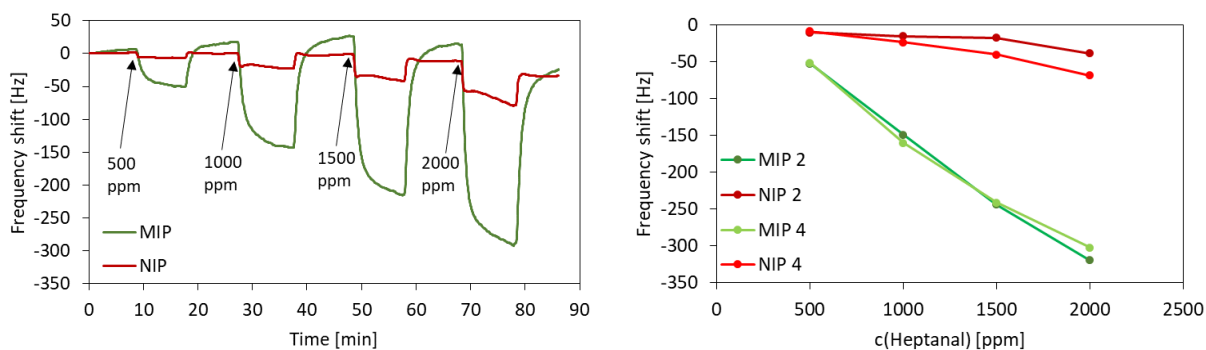
Figure 68: Example of a QCM measurement and absolute MIP and NIP frequency shifts plotted against heptanal concentration for sensor 2 and 4.

Figure 69Figure 70 shows the results for each sensor are presented individually. The other two sensors show the opposite behaviour. Apart from that, the magnitude of the frequency shifts caused by the same concentration of 1000 ppm varies from -34 to -169 Hz. Normalisation to the layer height places the signals for 1000 ppm in a narrower frequency range. However, they still vary too much to calculate useful average signals for the whole batch.
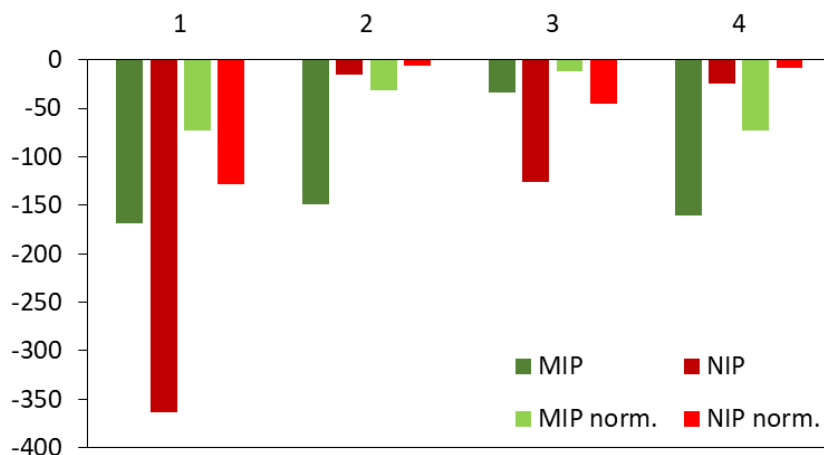
Figure 69: Summary of the frequency shifts for 1000 ppm heptanal including normalised signals for 100 nm polymer layer. n=4.

Like the blends prepared for sensing 2-propanol, the non-conductive oligomer solutions were mixed with P3HT to obtain conductive composites. Table 28 shows the amounts of the respective polymers and the resulting P3HT content of the composite.

Table 28: Volumes of MIP/NIP solutions and P3HT stock solution mixed to obtain the blends and the resulting P3HT content of the material.

MIP/NIP solution [µL]	P3HT solution (10 mg/mL) [µL]	P3HT [wt. %]
75	25	5
50	50	13
25	75	31

Table 29 presents the layer heights of the blends coated onto QCMs and the electric resistance of the blends coated onto chemiresistors. The layer height increases with increasing P3HT content. cMIP and cNIP layers with the same P3HT content were similar. The blend with the lowest P3HT content is not conductive at all. This means that the content is too low to completely bridge the gap between the electrodes. The blends containing 31 wt. % P3HT are more conductive than the ones containing only 13 wt. % which can be seen from the decrease of the electric resistance. The cNIP blends with 31 wt. % P3HT showed unexpectedly high resistances.

Table 29: Average layer heights of blends on QCM and average electric resistance of blend on chemiresistors. n=3-4.

P3HT [wt. %]		Average height [nm]	Standard deviation [nm]	Electrical resistance on chemiresistor [MΩ]	Standard deviation [MΩ]
5	NIP	171	47	--	--
	MIP	171	22	--	--
13	NIP	265	94	0.905	0.117
	MIP	228	22	1.252	0.339
31	NIP	343	113	2.583	0.113
	MIP	306	116	0.485	0.091

QCM Measurements

All sensors were tested with a series of heptanal concentrations. In the measurement shown in Figure 70, there is a clear difference between the frequency shifts of cMIP- and cNIP-coated electrodes, with the cMIP showing three times higher affinity towards the analyte. If all measured sensors of the batch are taken into account, one can see that the difference between the average MIP and NIP signals is rather small, namely by approximately 10 Hz lower than the NIP signal resulting in an average imprinting factor of 1.2. What is also apparent, is the large standard deviation of the absolute NIP signals. Given that the average layer height of MIP and NIP is exactly the same, normalising to the layer thickness does not change the results significantly, which can be seen below. In this section the frequency shifts for 500 ppm heptanal were used for comparing the QCM signals.
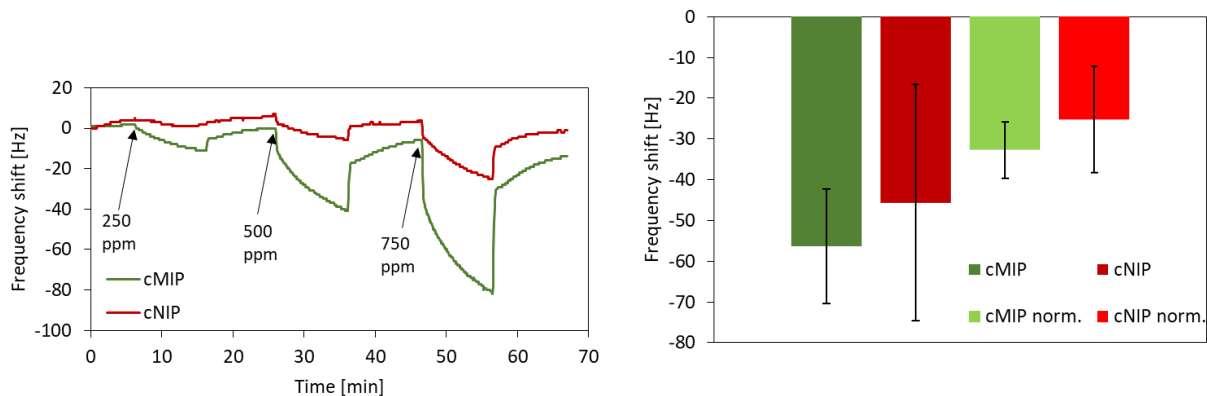
Figure 70: Example of a QCM measurement with a QCM coated with blends containing 5 wt. % P3HT (left) and average signals for 500 ppm including signals normalised to 100 nm polymer layer. n=3.

The imprinted blends containing 13 wt. % P3HT clearly exhibit stronger affinity for the analyte than the corresponding non-imprinted blend. As can be seen in Figure 71 the responses for 500 ppm heptanal of all sensors are in the same range which is reflected in a narrow standard deviation. The same trend can be seen when the frequency shifts are normalised to 100 nm polymer layer.
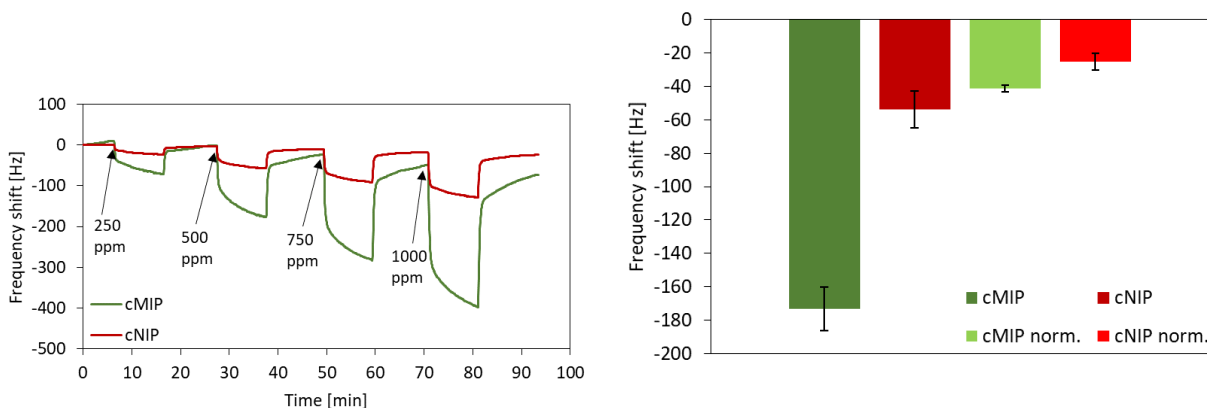
Figure 71: Example of a QCM measurement with a QCM coated with blends containing 13 wt. % P3HT (left) and average signals for 500 ppm including signals normalised to 100 nm polymer layer. n=3.

Figure 72 depicts the results of the measurements with blends containing 31 wt. %. Again the QCM measurements indicate stronger affinity between the analyte and the cMIP compared to the cNIP. The

spikes occuring on the cNIP channel when changing the flow between clean air and analyte are probably a sign of disruption of the equilibrium. This behaviour is also present on the cMIP channel for higher concentrations.
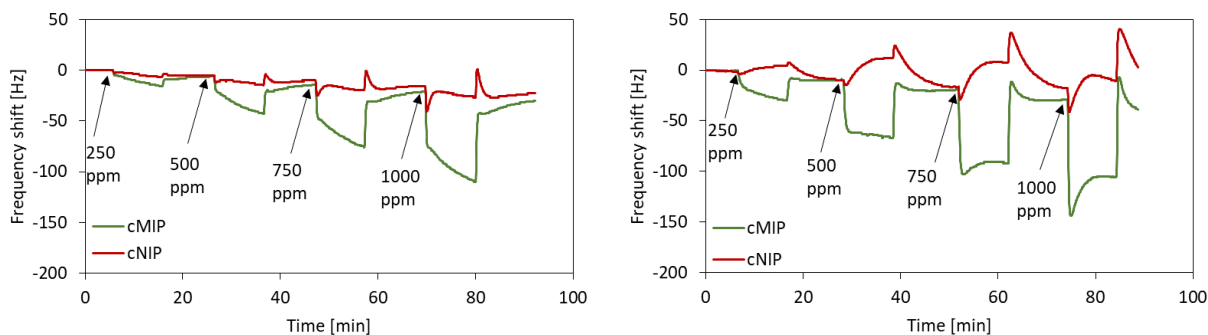
Figure 72: QCM measurements with QCMs coated with blends containing 31 wt. % P3HT.

To further verify the imprinting effect, slectivity tests with ther VOCs were conducted. Figure 73 shows sensor responses of 1000 ppm 2-propanol on QCMs coated with different blends. Testing for sensitivity towards 2-propanol is important, because it is also an analyte in this work; cross-selectivity is not beneficial for measuring with both types of sensors at the same time. However, these experiments did not yield any clear sensor signal. In both measurements shown, the QCMs exhibit signal drift on both channels. When 2-propanol is introduced, the slope slightly decreases.
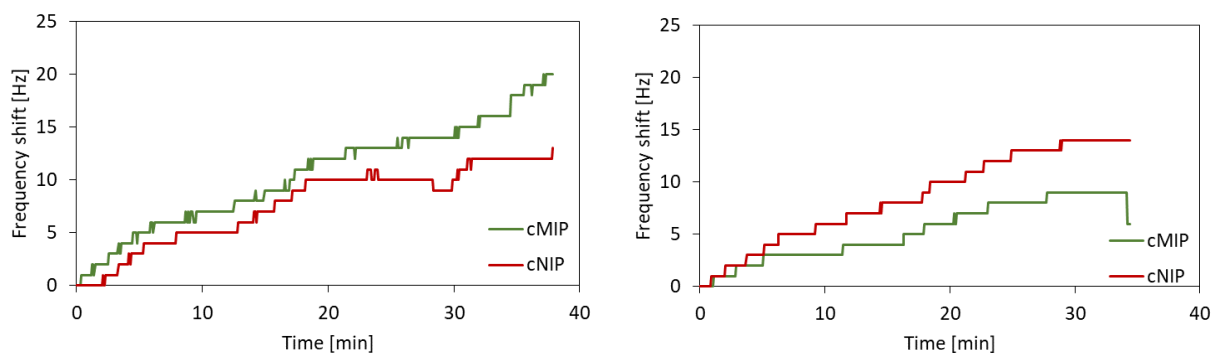
Figure 73: Selectivity tests with 1000 ppm 2-propanol on QCMs coated with 5 wt. % P3HT (left) and 31 wt. % P3HT (right).

Since heptanal, apart from the aldehyde, consists of an unbranched hydrocarbon chain, selectivity tests with other linear molecules are interesting. In theory, 1-butanol should fit into the cavities, since it is a linear alcohol and even smaller than heptanal. 1000 ppm 1-butanol cause frequency shifts of about -20 Hz (Figure 74) which are much lower than for the same concentration of heptanal. The signals of the cNIPs-coated electrodes are slightly stronger which indicates weak interaction of 1-butanol with the binding sites.
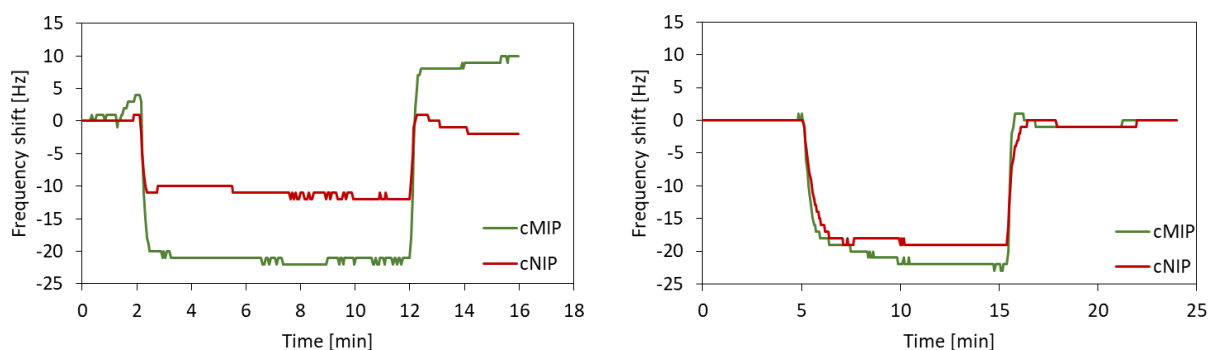
Figure 74: Selectivity tests with 1000 ppm 1-butanol on QCMs coated with blends containing 5 wt.% (left) and 31 wt.% (right) P3HT.

n-Heptane was tested since it is very similar to the target analyte heptanal. In fact, it is the same hydrocarbon chain lacking the aldehyde function. Thus, it should fit into the imprints. Figure 75 shows two examples of QCM measurements with this analyte. 1000 ppm n-heptane cause frequency shifts around -5 Hz. The shifts are identical on both channels which indicates that they only reflect unspecific binding. This shows that the binding of the target analyte heptanal in the imprints mainly relies on the aldehyde group of the molecule.
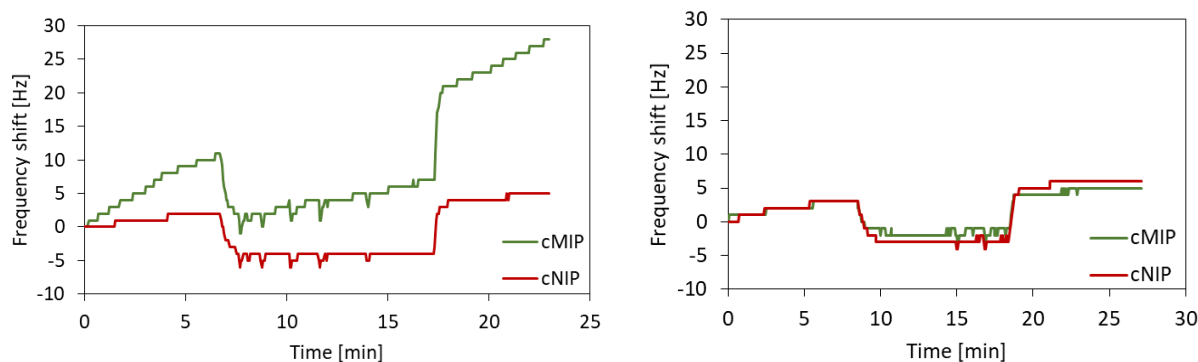
Figure 75: Selectivity tests with 1000 ppm n-heptane on QCMs coated with blends containing 13 wt. % (left) and 31 wt. % (right) P3HT.

The tests suggest good selectivity of the composite coated sensors for the target analyte. Other VOCs cause only small signals which are mainly attributed to unspecific binding.

Chemiresistor Measurements

Figure 76 shows the responses of chemiresistors coated with cMIP blends containing 13 wt. % P3HT when exposed to 250-500-750-1000 ppm heptanal. In between, the cell was flushed with dry air. The chemiresistors respond to the analyte heptanal with an increase in measured voltage resulting from changes in electric resistance. The effect for 250 and 500 ppm is very weak, around 0.1 %, for all measured sensors. For 750 and 1000 ppm, one can observe clear signals, with 1000 ppm causing 1.8 times larger shift. The change in resistance is reversible, which means that the sensor signal approximately returns to the initial value. However, the chemiresistors exhibit baseline drift. Because of that, the signals in Figure 76 seem like not returning to baseline level. The absolute signals are calculated as the difference from the highest point of the signal to the baseline right before the analyte is introduced into the cell. There is a noticeable difference in the magnitude of the signals of the three sensors. The 1000 ppm signals range from 0.16 to 0.60 %.
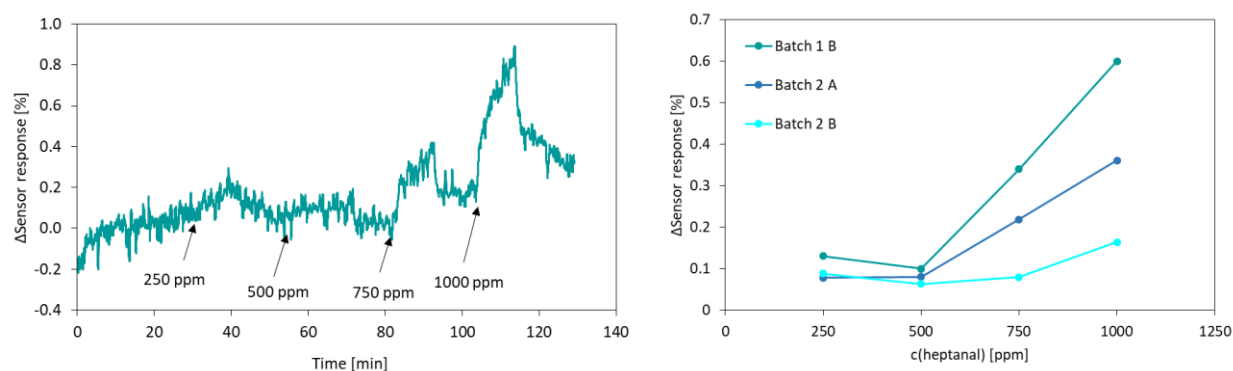
Figure 76: Example of a chemiresistor measurement with a sensor (Batch 1 B) coated with cMIP containing 13 wt. % P3HT (left). Absolute sensor responses for heptanal concentration of three sensors coated with cMIPs (13 wt. % P3HT) from two different batches (right).

Figure 77 shows the results of the chemiresistors coated with the cMIP containing 31 wt. % P3HT. The two measured sensors respond similarly to the heptanal concentrations. Like the blends with lower P3HT content, they respond better to concentrations 750 and 1000 ppm.
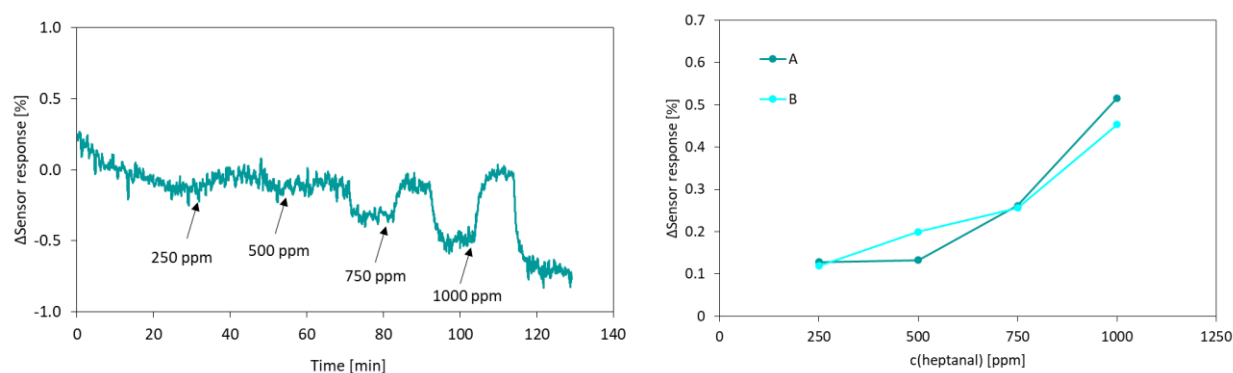
Figure 77: Example of a chemiresistor measurement with a sensor (sensor A) coated with cMIP containing 31 wt. % P3HT (left). Absolute sensor responses for heptanal concentration of two sensors coated with cMIPs (13 wt. % P3HT) (right).

For reference, pristine P3HT was coated onto chemiresistors. This resulted in devices with a resistance of 1.470 ± 0.173 MΩ. The sensors were measured in the same way as the cMIP sensors. Figure 78 shows one measurement together with the sensor signals obtained with both sensors. Pristine P3HT also responds to heptanal with a decrease in resistance. For the P3HT-coated sensors, the response towards higher

heptanal concentrations is weaker compared to the cMIP-coated ones, with a maximum response of 0.38 % for 1000 ppm.
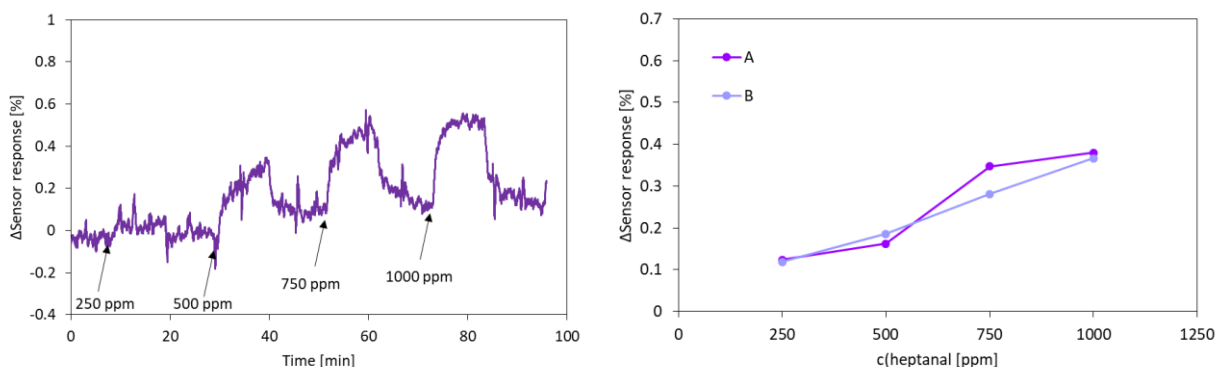
Figure 78: Example of a chemiresistor measurement with a sensor (sensor A) coated with pristine P3HT (left). Absolute sensor responses for heptanal concentration of two sensors coated with P3HT (right).

For direct comparison, cMIP- and cNIP-coated chemiresistors were prepared and exposed to the same heptanal concentrations. Two sensors were prepared and measured each with blends containing 13 and 31 wt. % P3HT. Figure 79 compares the absolute signals of the sensors for 1000 ppm heptanal. For the blends containing 13 wt. % P3HT, molecular imprinting seems to increase the sensor signal. In this experiment, the cNIP blends containing 31 wt. % P3HT showed similar responses as the 13 wt. % blends. However, the cMIP-coated sensors respond with smaller shifts.
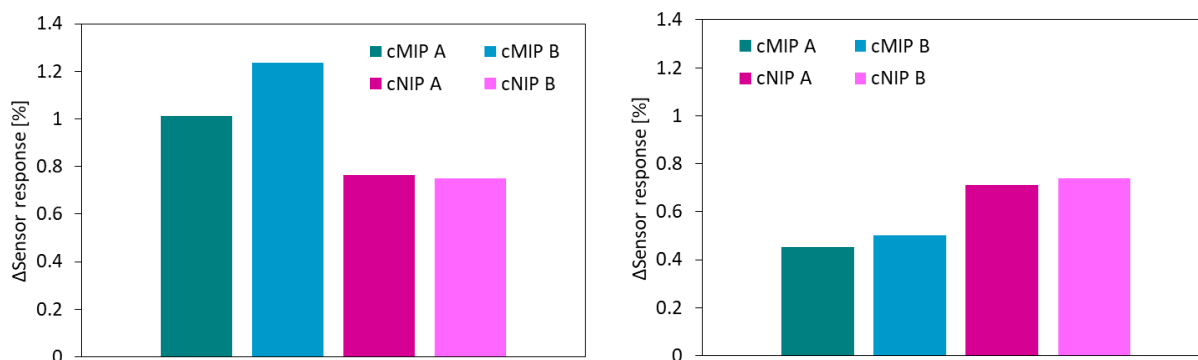
Figure 79: Sensor responses for 1000 ppm heptanal. Left: chemiresistors coated with cMIP and cNIP blends containing 13 wt. % P3HT. Right: chemiresistors coated with cMIP and cNIP blends containing 13 wt. % P3HT.

By comparing the sensor signals coated with different batches of the same polymer blends, it becomes evident that they differ in resistivity response when exposed to the same heptanal concentrations. One possible explanation for this variation could be irregularities in film thickness and coverage from manually drop coating the polymer onto the electrodes.

4.2.4. Surface Characterisation

Light Microscope

Samples of the non-conductive polymers as well as the conductive blends are characterised with various surface analysis methods. For a rough overview, a light microscope is used. Figure 80 shows microscope images of the non-conductive MIP and NIP. The images show very rough surfaces of the polymers. This could explain the variations in the absolute signals, because gas molecules are more likely to adsorb on rougher surfaces.
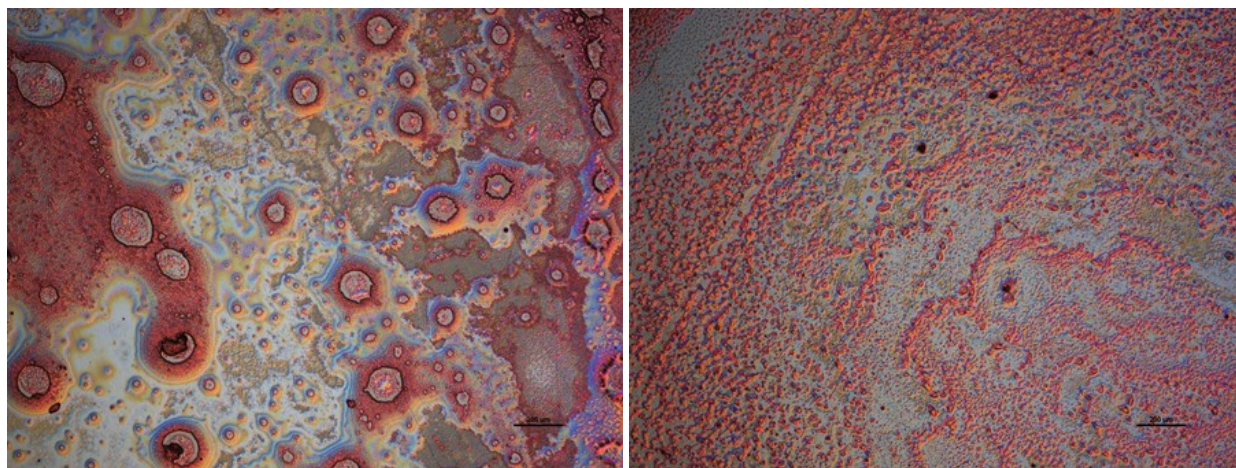
Figure 80: Light microscope images of the DMAA-co-EGDMA MIP (left) and NIP (right) surfaces. Scale bar: 200 µm.

Figure 81 to Figure 83 show microscope images of the conductive blends on QCM electrodes. Compared to the non-conductive polymers, the blends appear smoother, without visible pores. From the images it seems that the cNIPs form more homogenous layers than the cMIPs. The latter seem to contain larger amounts of crystalline material incorporated into the layers. This could be a similar solubility issue as observed in the blends for detecting 2-propanol.
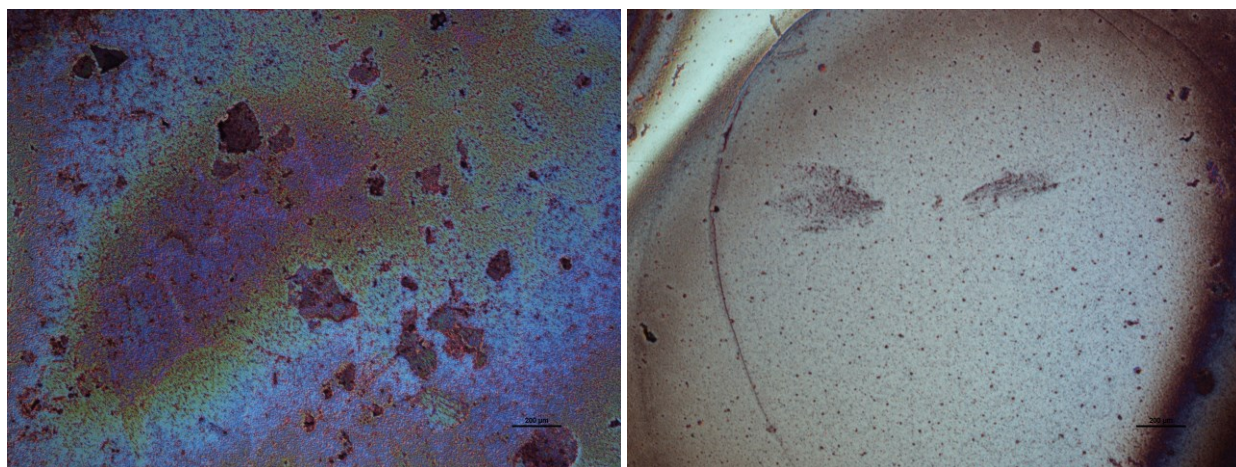
Figure 81: Light microscope images of the cMIP (left) and cNIP (right) containing 5 wt. % P3HT. Scale bar: 200 µm.
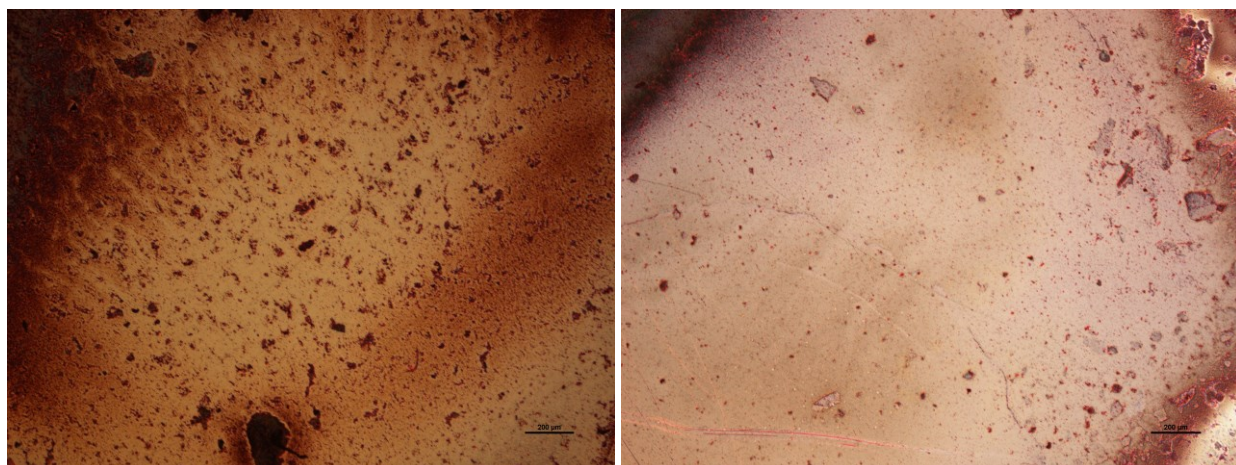
Figure 82: Light microscope images of the cMIP (left) and cNIP (right) containing 13 wt. % P3HT. Scale bar: 200 µm.
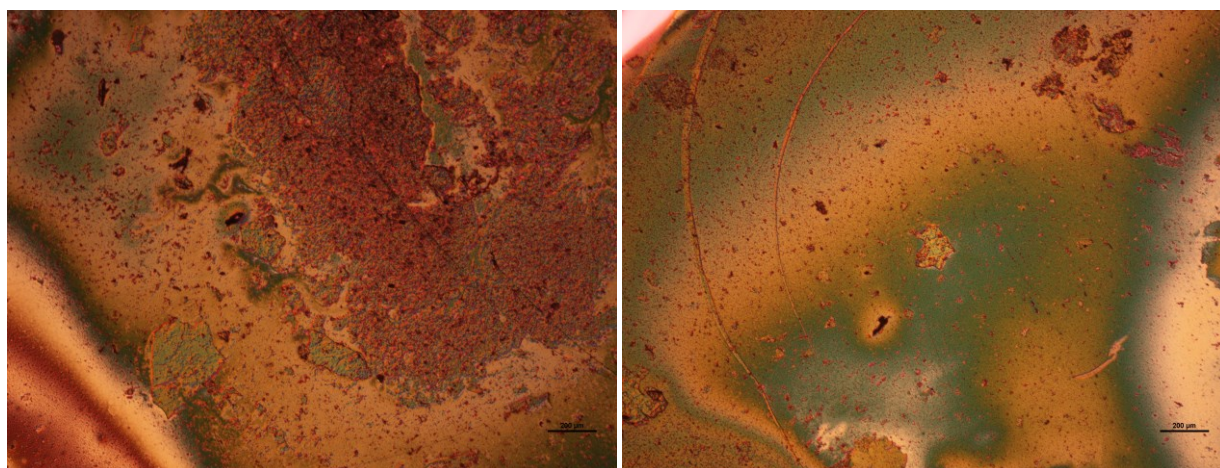
Figure 83: Light microscope images of the cMIP (left) and cNIP (right) containing 31 wt. % P3HT. Scale bar: 200 µm.

Peak force Quantitative Mechanical Property Mapping (QNM) is a method that allows for mapping nanomechanical properties of a sample by probing it with an AFM tip. This helps gaining better understanding on how the MIP and P3HT blend together. Figure 84 shows images of a peak force QNM measurement of MIP blends containing 13 wt. % P3HT. Most properties correspond well to the height image which shows a porous surface. In the stiffness image, one can see patterns that do not overlap with the pore structure. This suggests that the stiffness of the blend is not homogeneous over the whole surface. This can be caused by inhomogeneous mixing of the DMAA-*co*-EGDMA and P3HT or higher crosslinking degree in the stiffer areas.
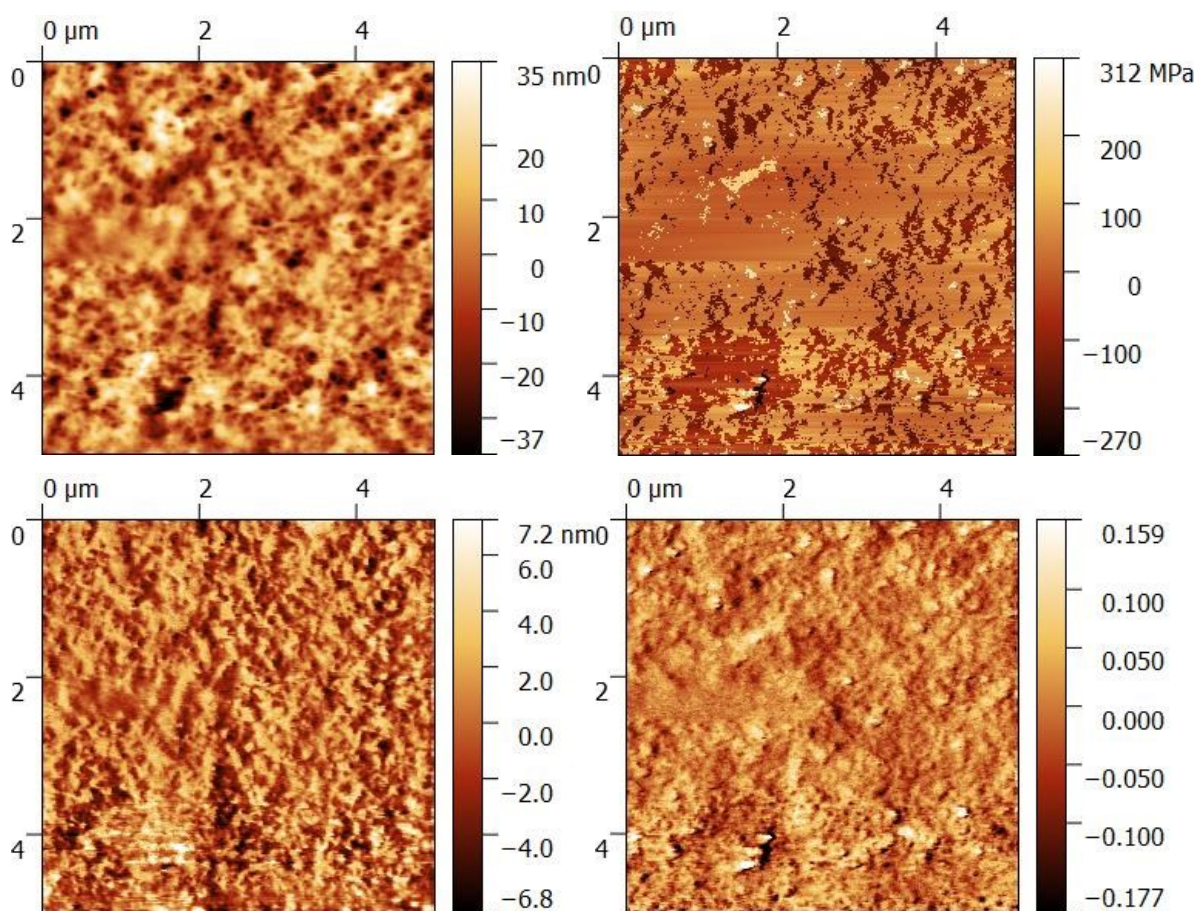
Figure 84: Peak force QNM measurement of a cMIP blend containing 13 wt. % P3HT. Top left: height, top right: stiffness, bottom left: deformation, bottom right: log DMT modulus.

Figure 85 shows the results of the same analysis of samples containing 31 wt. % P3HT. In this case, the stiffness is homogeneous over the probed area. The deformation image shows some pattern. On close observation, it is noticeable that it matches the pattern of the large pores in the height image. This might stem from the tip being unable to probe the deeper valleys in the same manner as the smooth area surrounding them.
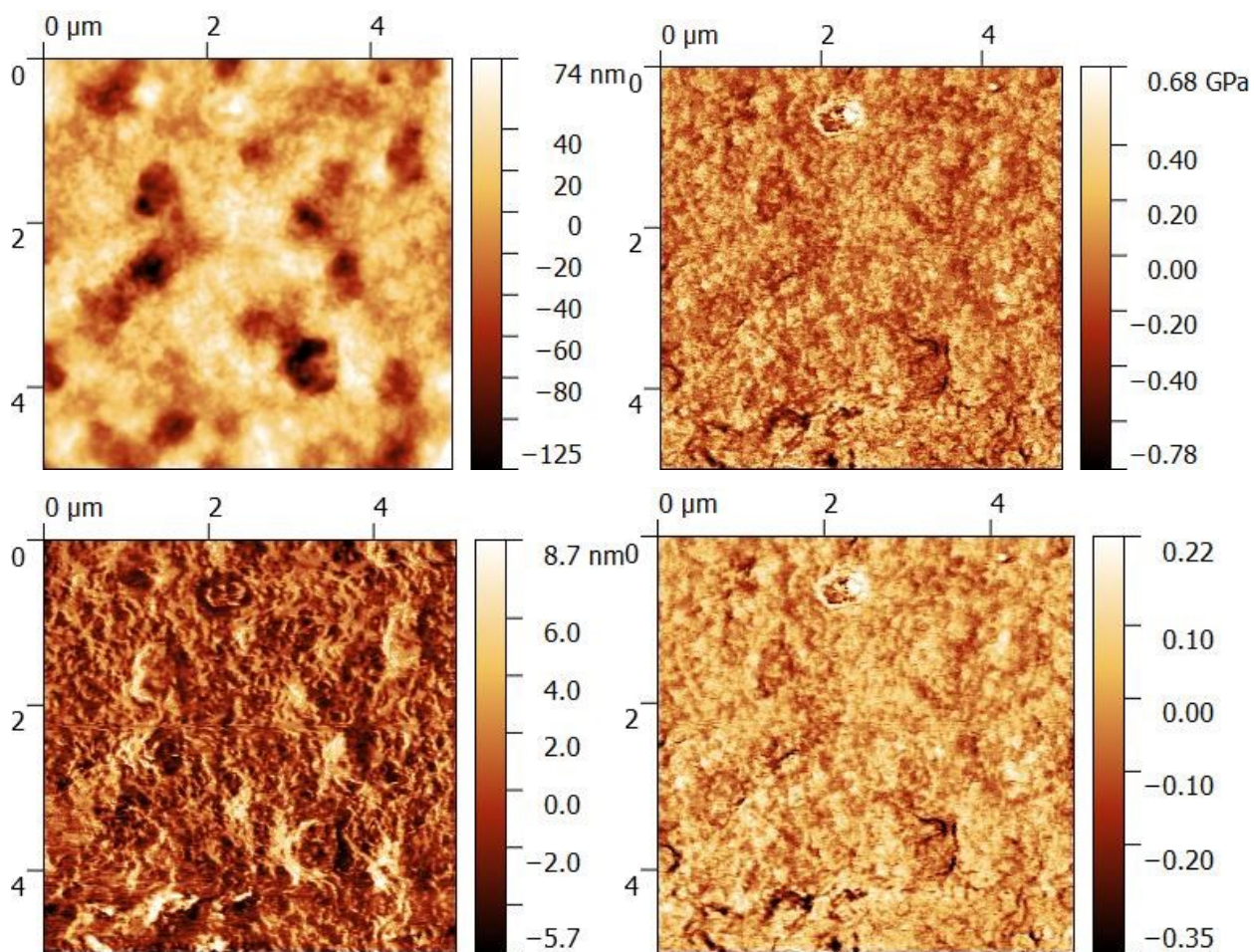
Figure 85: Peak force QNM measurement of a cMIP blend containing 31 wt. % P3HT. Top left: height, top right: stiffness, bottom left: deformation, bottom right: log DMT modulus.

SEM and EDX

The samples containing 13 wt. % P3HT were also analysed with SEM. Figure 86 and Figure 87 show images of cMIP and cNIP respectively. Like the samples of 2-propanol cMIPs, small particulate structures can be seen protruding from the polymer layer in the images taken at 1.00 KX magnification. The cMIP seems a

little rougher than the cNIP. Upon zooming in on the smooth areas, the surface appears to have fine cracks; the cNIP shows signs of pores.
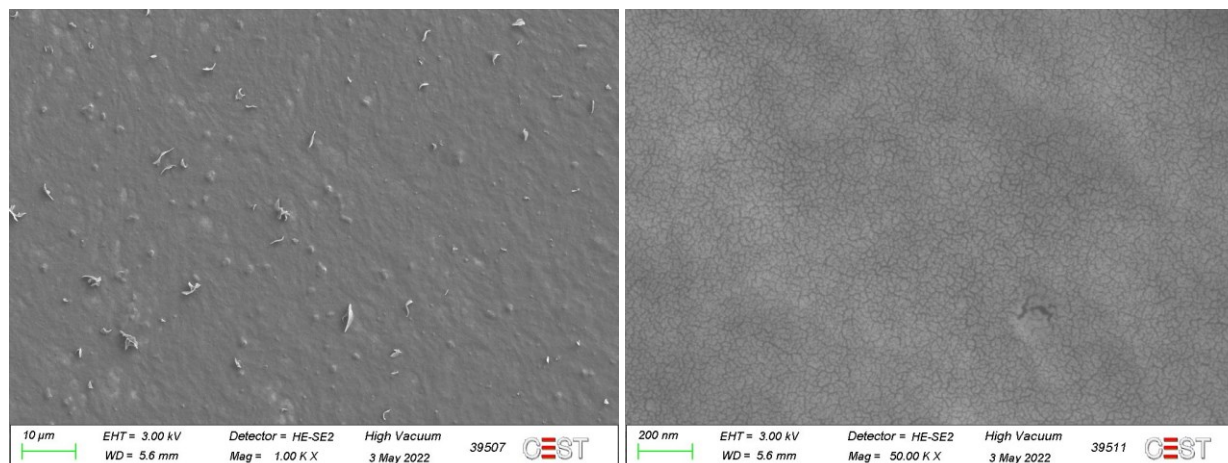
Figure 86: SEM images of cMIP blend containing 13 wt. % P3HT.
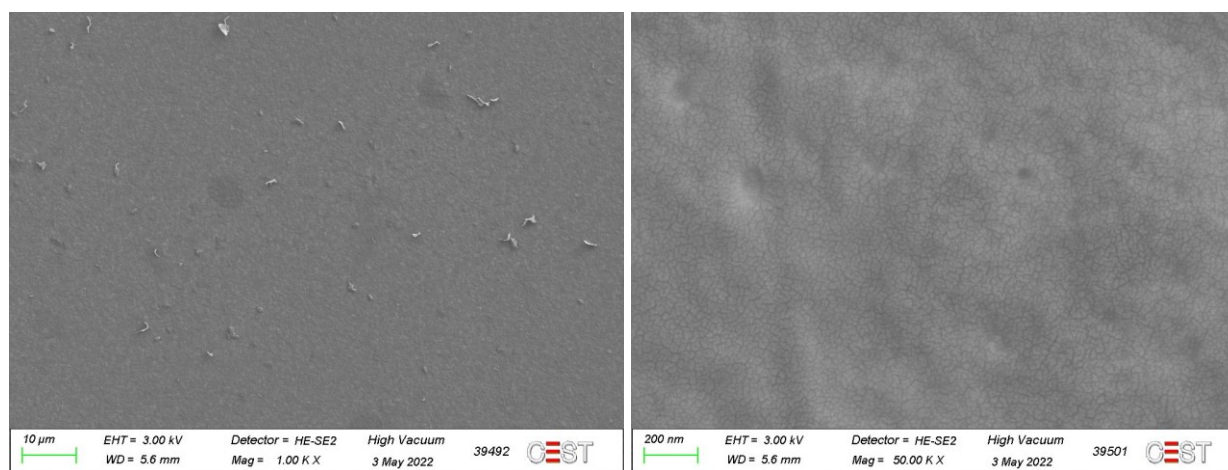
Figure 87: SEM images of cNIP blend containing 13 wt. % P3HT.

On the cMIPs, additional analysis with EDX is performed. Figure 88 shows the probed area (rectangle) and an additional spot (red circle) outside of this area. Table 30 summarises the results of the analysis. As expected, mainly carbon signal is present since the surface consists mainly of organic polymers. The second largest signal results from sulphur originating from the thiophene part of P3HT. Oxygen signals can again be attributed to the polymer, which comprises carboxylic acid groups. Other elements detected are gold and silicon. The gold signal comes from the underlying electrode and the silicon from the quartz substrate.
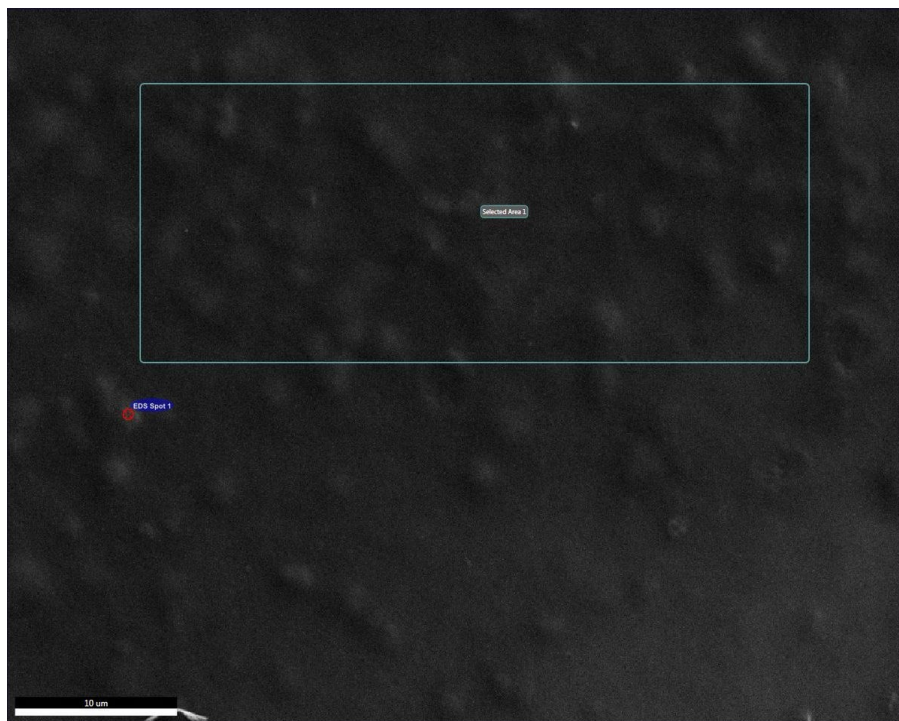
Figure 88: SEM image showing the probed area (rectangle) and an additional spot (red circle) outside of this area. Scale bar: 10 μm.

Table 30: Results of the EDX measurement.

	Element	Weight %	Atomic %
	C K	65.7	92.5
	O K	0.2	0.2
Area 1	Si K	0.8	0.5
	Au M	24.4	2.1
	S K	8.9	4.7
	C K	82.8	95.7
	O K	0.6	0.5
Spot 1	Au M	9.3	0.7
	S K	7.3	3.2

4.3. Acetophenone

4.3.1. Original Procedure

This synthesis procedure originates from a publication for imprinting terpenes and is described in the experimental section. Due to the lack of MIPs specific for acetophenone in literature, this polymer was adapted since the terpenes show some structural similarities to the ketone. As a starting point the MIP and corresponding NIP were reproduced as stated in the publication with the template acetophenone. Table 31 shows the average layer heights of the thin films on QCM.

Table 31: Average layer height of MIP and NIP on QCM obtained with the original procedure. n=4.

	average height [nm]	standard deviation [nm]
NIP	21	6
MIP	23	18

The layer heights are in a range of about 20 nm, which is too thin for the application. For some of the electrodes the resonance frequency is the same as before coating. This means that there is most likely no polymer deposited. Figure 89 shows the results of the only measurement of this first batch. The QCM was exposed three times to 150 ppm acetophenone for ten minutes followed by flushing with clean air for ten minutes, respectively. Even though the polymer layers are very thin, there is a clear difference in affinity between MIP and NIP. This is reflected in the four times stronger frequency shift of the MIP-coated electrode in response to the analyte.
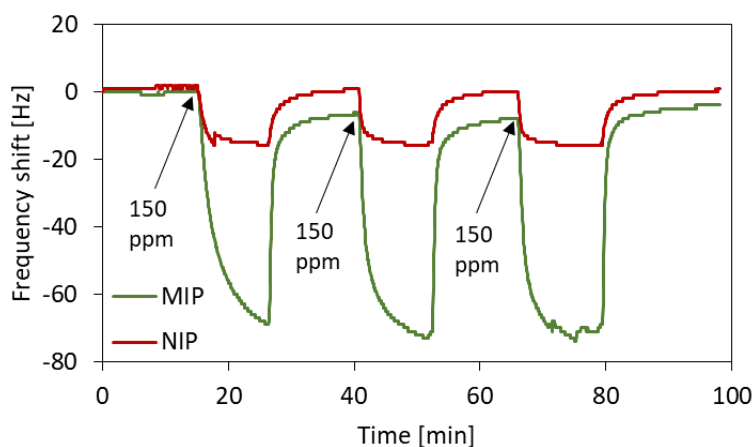
Figure 89: QCM measurement with MIP and NIP obtained by following the original procedure.

4.3.2. Optimisation of Layer Height

As the original procedure for MIP synthesis did not yield polymer layers of sufficient thickness and electrode coverage, several parameters were changed subsequently to improve this. Simply increasing the amount of oligomer solution spin-coated did not have a significant effect. Reducing the amount of solvent from 1197 (2 mL total) to 697 (1.5 mL), or 197 µL (1 mL) did not change the layer height either. Additionally, the 1 mL batch showed worse imprinting effect with the NIP showing up to four times higher affinity than the MIP. The following experiments were continued with a total volume of 1.5 mL. The amount of AIBN was increased to 1 wt. % which means 10x increase. Pre-polymerisation time at 60°C while stirring under argon atmosphere was increased to reach a visible gel-point, which happened after about 1h. Drop coating was conducted instead of spin-coating. The undiluted gel-like oligomer solution turned out too viscous and did not spread over the electrode. Therefore, the solution was diluted before coating. 1:10 dilution was established as optimal, because it yielded smaller differences between MIP and NIP layer thickness, respectively. Figure 90 compares the layer thickness of MIP and NIP layers on QCM. It is apparent that only drastically increasing pre-polymerisation time leads to sufficiently thick layers.
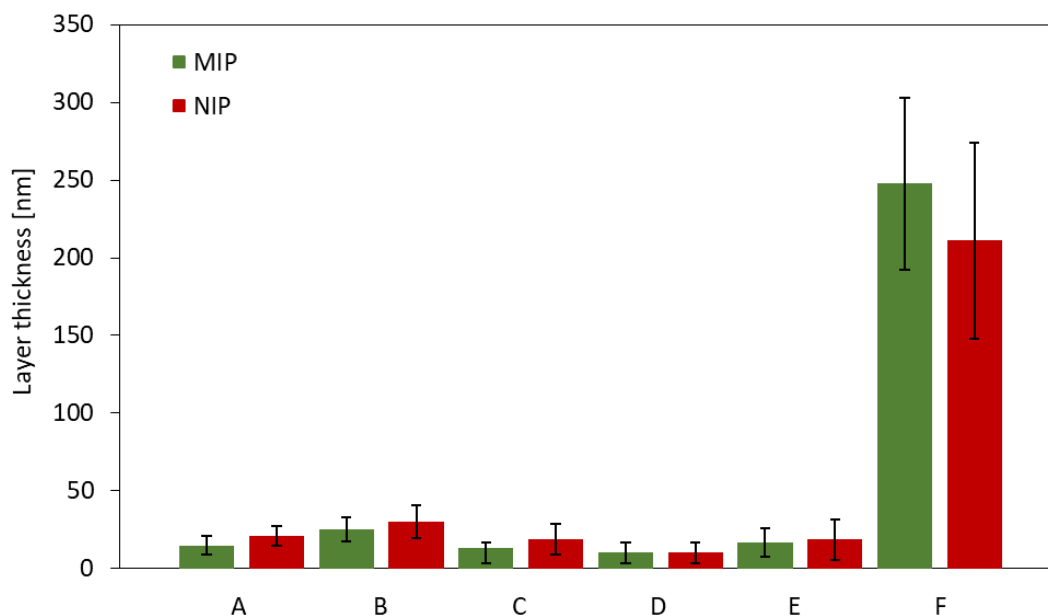
Figure 90: Average layer thickness and standard deviation of selected batches of MIP and NIP on QCM. A: Original procedure. B: Reduction of the solvent to 1.5 mL of total volume. C: 20 min pre-polymerisation time. D: Increase of AIBN to 1 wt. %. E: Drop-coating instead of spin-coating. F: Final procedure as stated above. n=3-5.

Figure 91 shows an example of a QCM measurement. After exposing the sensors to a series of 50-100-150-200 ppm acetophenone in air for ten minutes each, the responses were compared. In between the acetophenone concentrations, the cell was flushed with clean air. It is clearly visible that the frequency decreases on both channels as soon as acetophenone vapour is injected into the measuring cell. However, the signal on the MIP-coated channel being twice as strong as on the NIP indicates stronger affinity of the analyte towards the imprinted material. Furthermore, signals depend on acetophenone concentration.

It is visible that MIP-coated electrodes on average cause 1.6 times higher frequency shifts which indicates stronger interaction of the analyte with the imprinted polymer. However, it is not possible to observe a connection between layer height and sensor response.
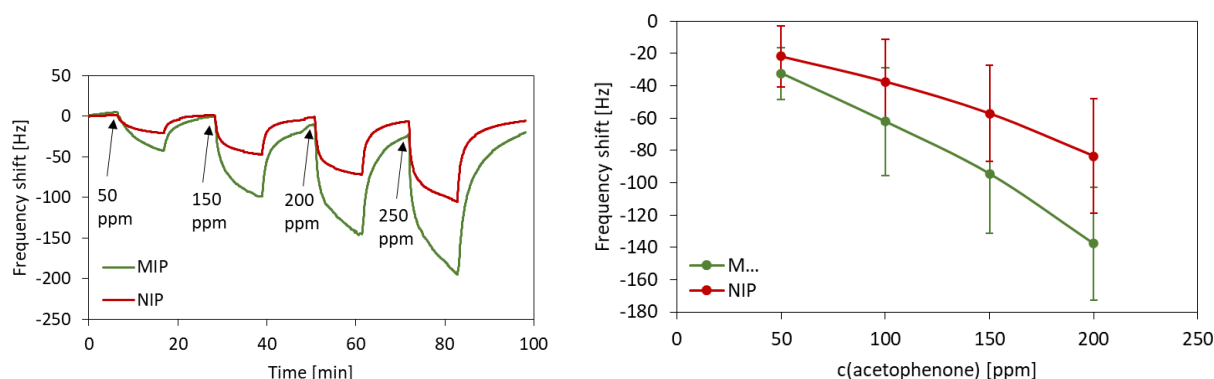
Figure 91: Left: QCM measurement acetophenone on air. 50, 100, 150, 100 ppm. Cell is flushed with air in between. Right: Average and standard deviation of shifts on MIP- and NIP-coated electrodes respectively. n=3.

4.3.3. P3HT Blends (First Series of Experiments)

Chemiresistor

In contrast to the experiments for 2-propanol and heptanal, where the conductive blends were tested first on QCM and then transferred to chemiresistors, the opposite approach was chosen for the acetophenone cMIPs. In this case, the blends are developed on chemiresistors directly to find the optimum composition. This allows for developing and testing the blends directly on the sensor for which they are meant instead of developing on QCM and later transferring to chemiresistors. Furthermore, this approach allows for screening a larger number of compositions faster, because the chemiresistor setup allows for measuring up to six sensors simultaneously instead of one at a time, as it is the case for QCM. Like in the case of previous cMIPs, different volumes of the MIP and a 10 mg/mL P3HT solution in THF

were mixed and applied on the chemiresistor electrodes by drop-coating (3 µL). Table 32 shows the compositions of the resulting blends.

Table 32: Compositions of the P3HT blends.

MIP/NIP solution [µL]	P3HT solution (10 mg/mL) [µL]	P3HT [wt. %]	Electric resistance [MΩ]
75	25	0.8	7.122 ± 1.013
50	50	2.4	1.283 ± 0.152
25	75	6.8	0.707 ± 0.153

All sensors were tested with following acetophenone concentrations: 50-100-150-200 ppm. Each acetophenone flow lasted for 10 min followed by 10 min flushing with clean air. Compared to the other blends in this project, the amount of P3HT in these layers is very low, since the oligomer solutions are more concentrated. Nevertheless, all exhibited sufficient conductivity. Figure 92 shows an example of a chemiresistor measurement. This sensor is coated with cMIP blend containing 2.4 wt. % P3HT. It is remarkable that the sensor responds visibly to concentrations as low as 50 ppm. It shows concentration-dependent, reversible signals.
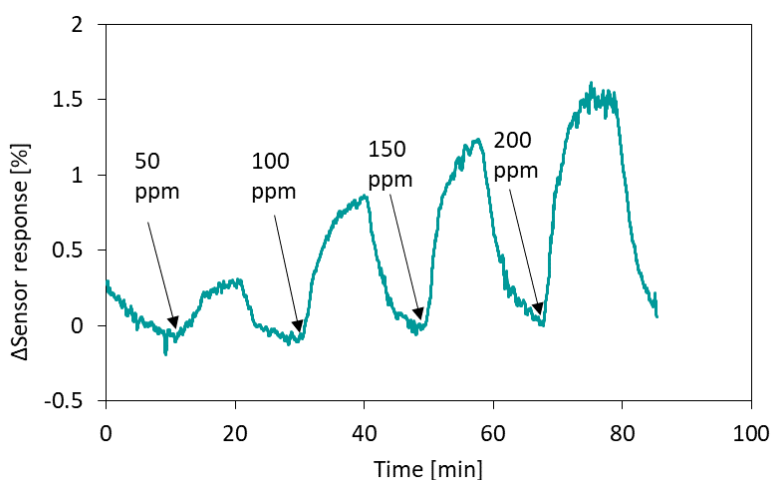
Figure 92: Example of a chemiresistor measurement coated with blend containing 2.4 wt. % P3HT.

Figure 93 summarises all performed measurements. It can be seen that the blends containing 0.8 wt. % P3HT saturate, and their signal does not increase when exposed to vapour concentrations above 100 ppm. The performances of the blends containing 2.4 and 6.8 wt. % P3HT are almost identical. However, the 6.8 wt. % blend shows higher deviation for the signal at 400 ppm. This is due to some sensors showing almost no signal increase from 150 to 200 ppm, i.e. saturation. Hence, the cMIP containing 2.4 wt. % P3HT was chosen for further experiments.
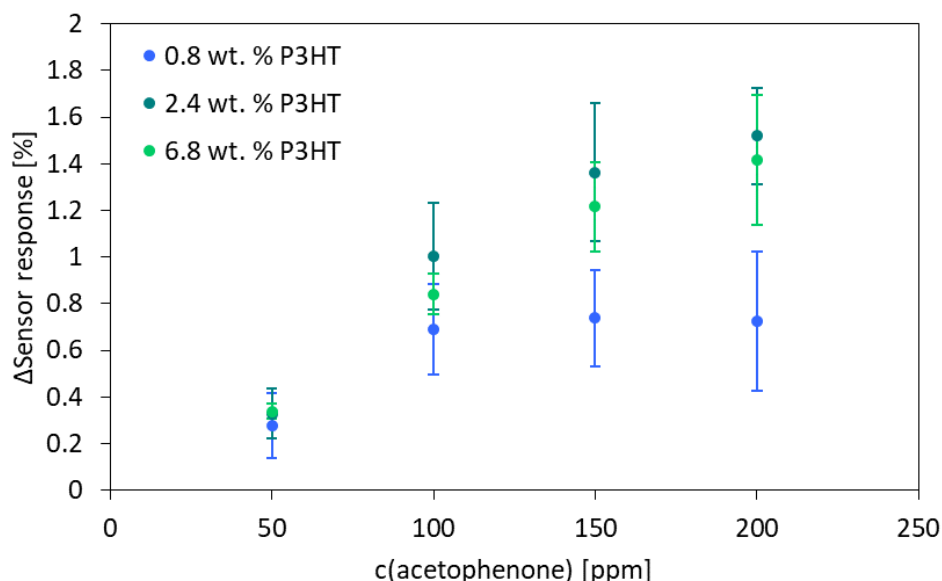
Figure 93: Average sensor signals of chemiresistors coated with cMIP blends. n=3.

To assess the influence of the MIP on the sensor signals, sensors coated with cMIP and cNIP (both 2.4 wt. % P3HT) as well as pristine P3HT (coated with the 10 mg/mL stock solution) were compared. *Figure 94* shows a superimposition of one measurement each. In this particular measurement, the cMIP-coated sensor shows higher responses to the analyte, than the cNIP coated sensor. Also, it seems to respond in a linear manner until the highest concentration. While the P3HT sensor shows a similar response as the ones coated with blends to 50 ppm, the sensor response does not increase for higher concentrations, suggesting early saturation.
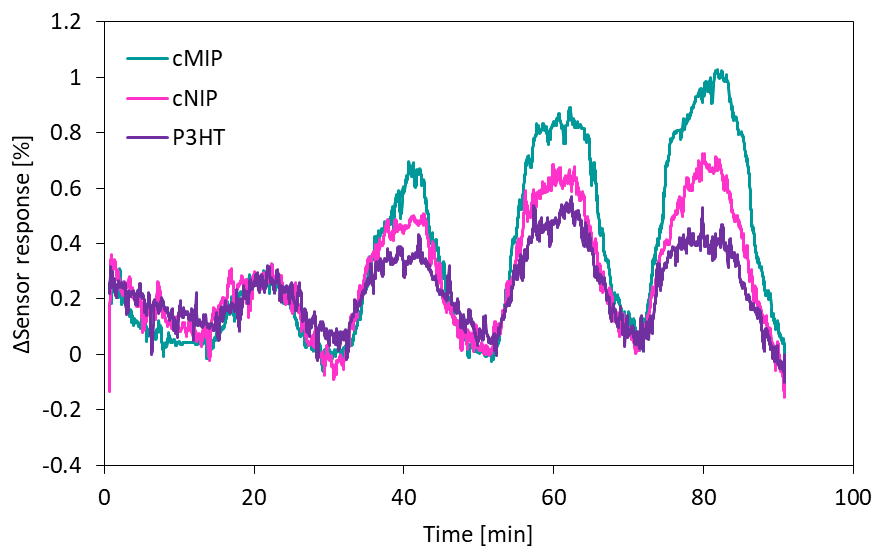
Figure 94: Comparison of the performance of chemiresistors coated with cMIP and cNIP containing 2.4 wt. % P3HT as well as with pristine P3HT.

Figure 95 summarises the data. The sensor signals were normalised to the signal for 50 ppm. Compared to the blends, the sensors coated with pristine P3HT show smaller responses; in fact they decreased again above 150 ppm. The sensors coated with cMIP and cNIP show stronger response and more linear behaviour. On average, they show similar sensor responses, which suggests that imprinting may not strongly influence sensor performance. It seems that blending P3HT with a MAA-*co*-EGDMA alone enhances the sensor response and linear range. However, it must be noted that the cNIP sensors showed a higher standard deviation between the measurements together with the onset of saturation between 150 and 200 ppm for some measurements. In that regard, the cMIP sensors perform better. It is possible that the imprints are beneficial for measuring higher concentrations since they could increase the uptake capacity of the material.
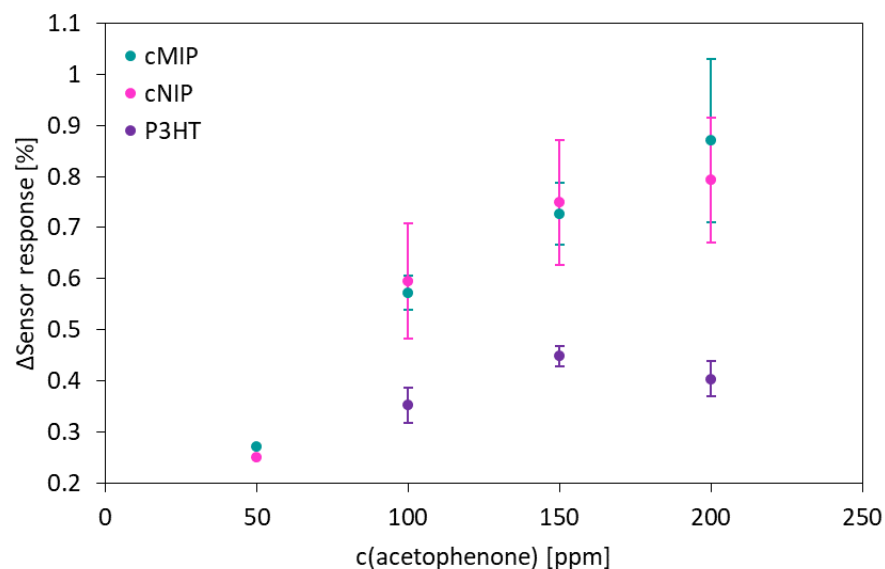
Figure 95: Average sensor signals of chemiresistors coated with cMIP and cNIP blends (2.4 wt. % P3HT) and pristine P3HT. n=3, normalised data.

QCM Measurements

To check, if the imprinting effect was retained in the blends, cMIP and cNIP containing 2.4 wt. % were coated onto QCM electrodes. To avoid thick layers this was done with undiluted blends and 1:10 dilutions of the blends. Table 33 shows the layer heights of the polymers. It comprises data of two batches. The layers of the diluted polymers of the second batch turned out much thicker than the ones of the first batch which results in a large standard deviation.

Table 33: Average layer height of cMIP and cNIP blends containing 2.4 wt. % P3HT on QCM. n=7-8.

		Average height [nm]	Standard deviation [nm]
Undiluted	**cNIP**	766	374
	cMIP	703	330
1:10 diluted	**cMIP**	388	366
	cNIP	410	378

All QCMs were tested with the same acetophenone concentrations as the chemiresistors. Figure 96 shows examples of QCM measurements with sensors coated with undiluted and diluted blends.
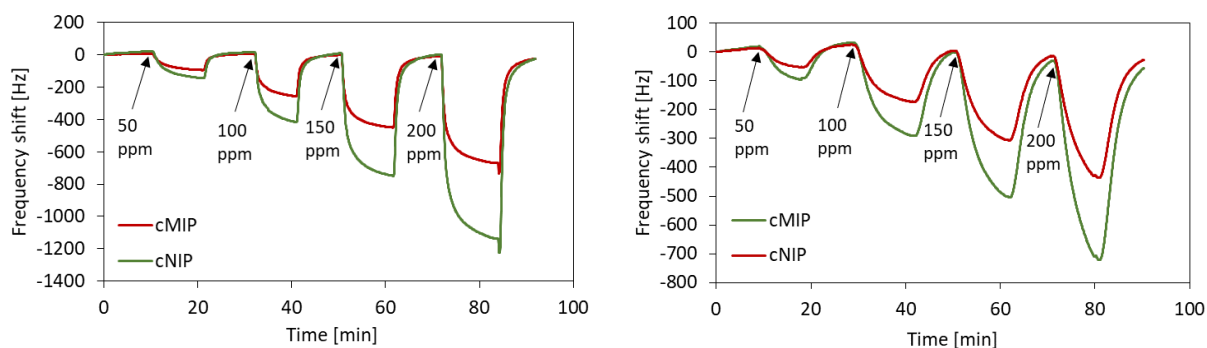
Figure 96: QCM measurements with QCMs coated with cMIP and cNIP blends containing 2.4 wt. % P3HT. Left: undiluted polymer, right: 1:10 diluted polymer.

In both cases the frequency shift on the cMIP-coated electrode is larger than the one coated with cNIP. Figure 97 shows the average sensor responses to 150 ppm in absolute values and normalised to 100 nm layer height. The average cMIP signals are larger than the average cNIP signals by a factor of 1.6 for undiluted blends and 1.4 for the 1:10 diluted polymers. This indicates higher affinity of the imprinted material to the analyte compared to the non-imprinted blends. This trend is still visible for the diluted blends when the signals are normalised to 100 nm layer height. In this case it makes sense to normalise the signals, since the layer heights of the two batches strongly differ from one another. Hence, the signals vary strongly. When normalising the signals of the sensors coated with the undiluted blends, imprinted and non-imprinted channel lead to very similar responses. However, it must be considered that the layers are close to the micrometre range. In this case, linear normalisation to the layer height is probably not useful since the gas molecules will most likely not diffuse through the whole layer. Since the layers are substantially thicker than is useful for sensing, the results obtained with the undiluted blends should be regarded cautiously anyway.
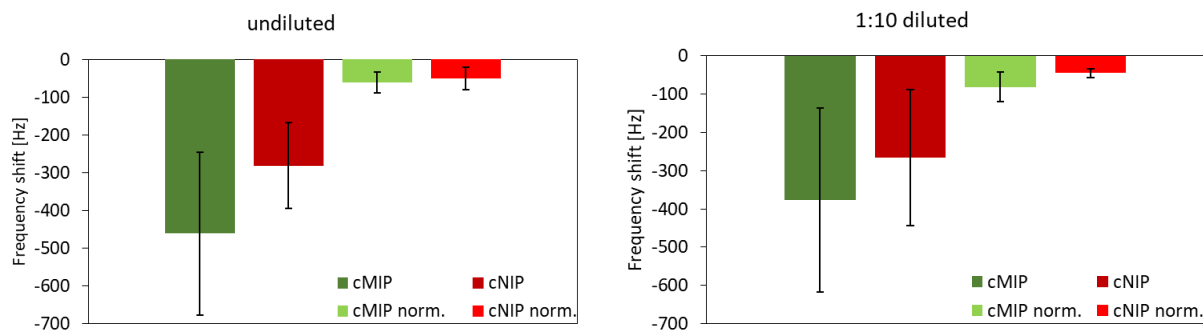
Figure 97: Average frequency shifts of QCMs coated with cMIP and cNIP blends containing 2.4 wt. % P3HT. Left: undiluted polymer, right: 1:10 diluted polymer. Signals for 150 ppm acetophenone. n=5.

Selectivity Tests

Both chemiresistors and QCMs were tested for selectivity. Figure 98 shows selectivity tests with toluene on chemiresistors coated with cMIP and cNIP containing 2.4 wt. % P3HT respectively. Even though the toluene is structurally similar to the analyte acetophenone and was applied at higher concentrations, there is only a very weak shift visible in the sensor response.
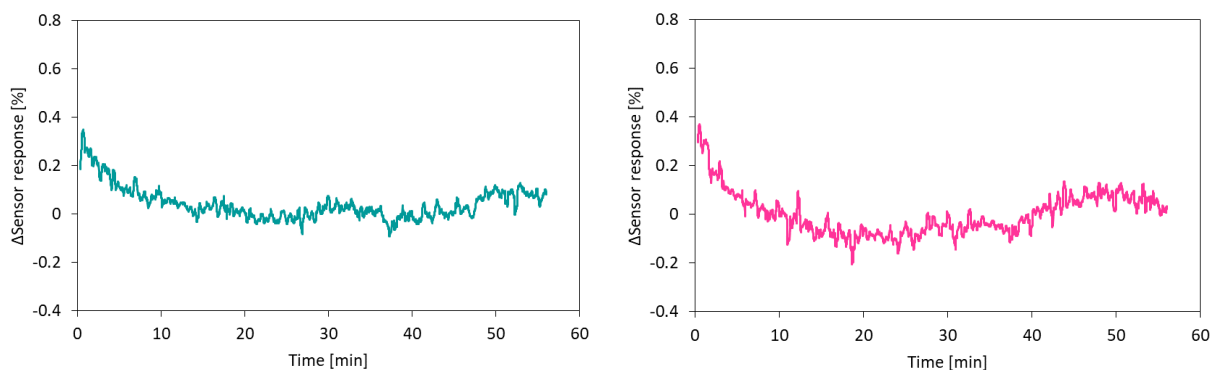
Figure 98: Selectivity test with toluene on chemiresistors coated with cMIP and cNIP containing 2.4 wt. % respectively. 200-500-1000 ppm.

Heptanal, which like the target analyte has a carbonyl group, shows a greater influence on the sensors. As can be seen in Figure 99, heptanal causes concentration-dependent responses of the chemiresistors, which are more pronounced on the cMIP-coated sensor. However, the tested concentrations are larger than the ones applied for acetophenone and cause smaller shifts than the target analyte. The selectivity

tests suggest that the rebinding of acetophenone is driven by the carbonyl function rather than by the aromatic ring.
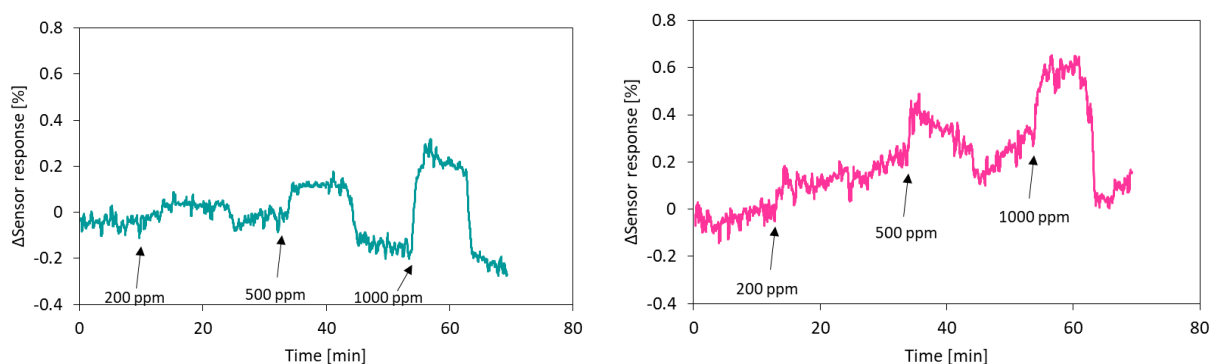
Figure 99: Selectivity test with heptanal on chemiresistors coated with cMIP and cNIP containing 2.4 wt. % respectively.

Figure 100 shows examples of selectivity tests on QCMs. The test with 1-butanol leads to smaller frequency shifts than acetophenone, even though higher concentrations are used. The frequency shifts are approximately the same on cMIP- and cNIP-coated channel, which indicates only unspecific binding and no specific interactions with the imprints. Tests with toluene show similar results. However, at higher concentration, one can see some interaction with the binding sites on the cMIP, as the frequency shift on this channel is larger than the cNIP by 20 Hz.
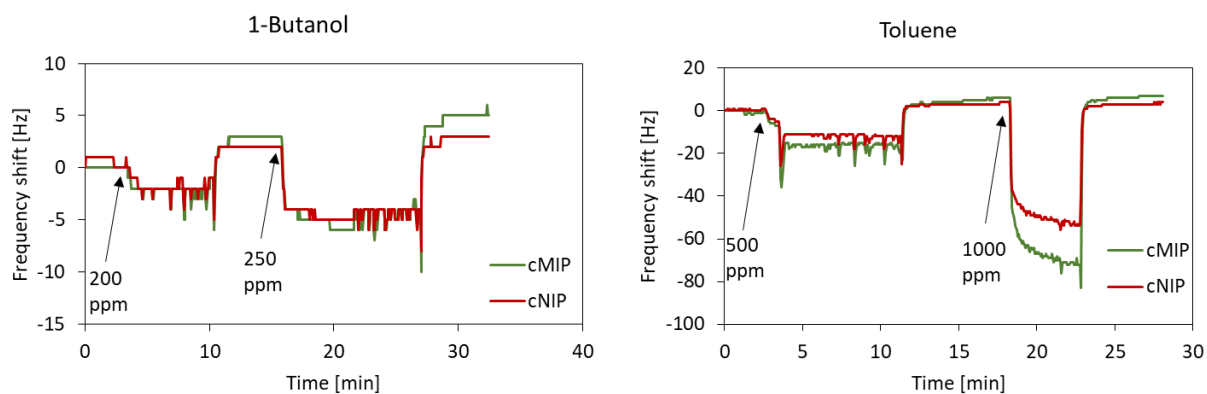
Figure 100: Selectivity tests with 1-butanol (left) and toluene (right).

4.3.4. P3HT Blends (Second Series of Experiments)

To further study the performance of different blends for acetophenone sensing, more sensors covering a broader range of P3HT amounts were prepared. Table 34 shows the composition and the resulting P3HT amounts of the blends as well as their electric resistances.

Table 34: Composition and the resulting P3HT amount of the blends as well as their electric resistance. n=8-10.

MIP/NIP solution [µL]	P3HT solution (10 mg/mL) [µL]	P3HT [wt. %]	Electric resistance [MΩ]
140	60	1	4.611 ± 3.290
98	102	2.5	3.229 ± 2.135
63	137	5	2.293 ± 1.842
46	154	7.5	0.531 ± 0.221
36	164	10	0.480 ± 0.205
14	186	25	0.374 ± 0.113

To gain more information about the sensing range of the chemiresistors, a wider span of concentrations was measured: 25-50-100-150-200-300-400 ppm. Figure 101 shows an example response of a chemiresistor measurement with a sensor coated with cMIP blend containing 10 wt. % P3HT. This sensor responds well in the range 50-300 ppm. At 25 ppm a small shift is noticeable. At 400 ppm the signal drops again.
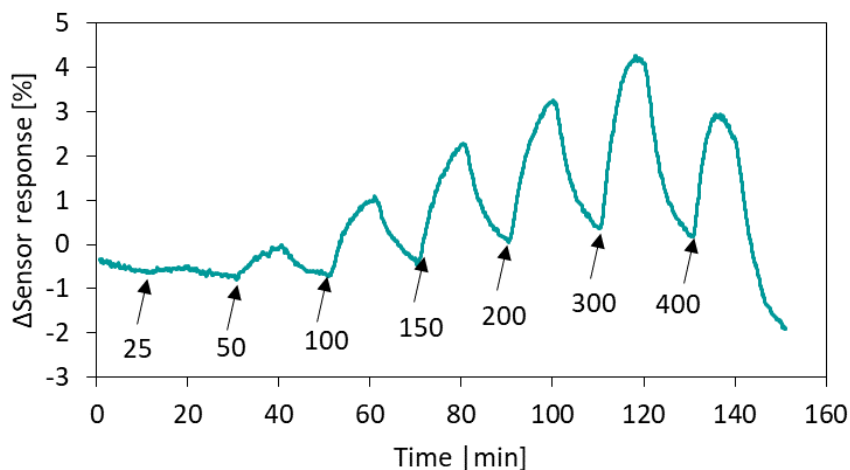
Figure 101: Example of a chemiresistor measurement of a sensor coated with cMIP blend containing 10 wt. % P3HT.

Figure 102 shows the average sensor responses of chemiresistors coated with blends containing different amounts of P3HT. It is evident that blends containing lower amounts of P3HT saturate at about 100 ppm acetophenone. The blend with 1 wt. % however, does not follow that trend. It shows linear increase of the sensor signal until the highest concentration without any signs of saturation. Blends above 5 wt. % have distinctly higher responses with the 10 wt. % blend exhibiting the highest absolute responses and almost linear behavior until 300 ppm. Interestingly, with the blend containing 25 wt. % P3HT, the response decreases and shows a similar behavior as the 7.5 wt. % blend with a flattening slope above 100 ppm. For 7.5, 10 and 25 wt. % blends, the signal increases until 300 ppm and afterwards drops at 400 ppm. For reference also measurements with sensors coated with pristine P3HT are included.
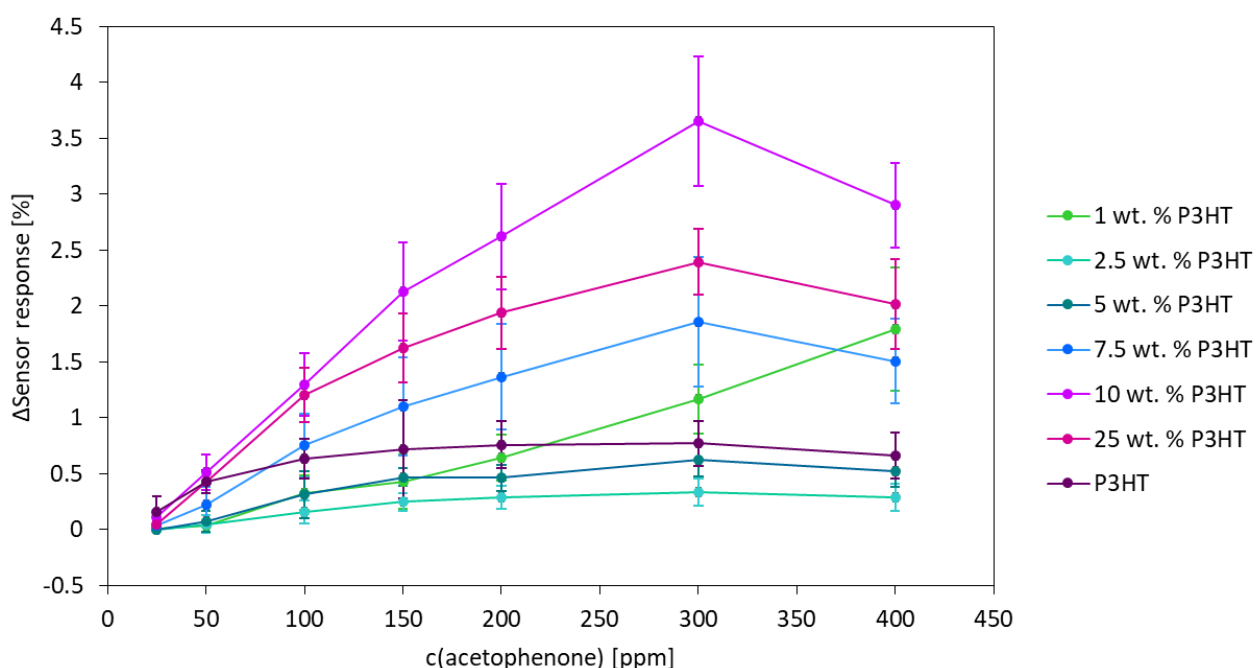
Figure 102: Sensor responses of chemiresistors coated with P3HT blends. n=4-5.

4.3.5. Selectivity Tests

Selectivity tests were performed with sensors coated with 10 wt. % P3HT cMIP blends. Heptanal and acetophenenone (Figure 103) were tested, because they share the presence of a carbonyl function with acetophenone. The sensors were also exposed to the alcohols 2-propanol and ethanol (Figure 104). Toluene was tested because of its aromatic character and n-heptane as a structurally unrelated compound (Figure 105). In most measurements, one can only see noise. Heptanal causes small shifts which do not

depend on concentration. Toluene at high concentrations leads to negative shifts. This sets them apart from the sensors comprising 2.4 wt. % P3HT blends, which showed almost no response to toluene.
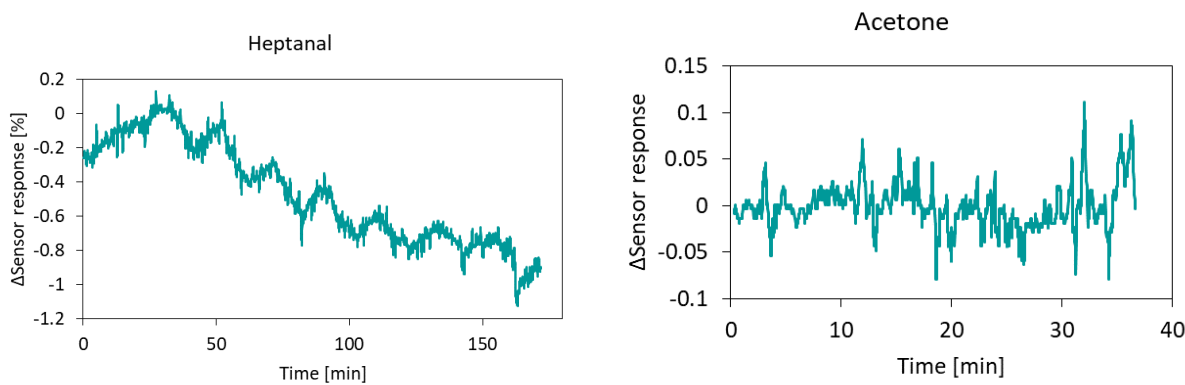
Figure 103: Selectivity tests with VOCs containing carbonyl functionalities. Left: Heptanal (100-150-200-300-400-500-750-1000 ppm). Right: Acetone (5000 ppm).
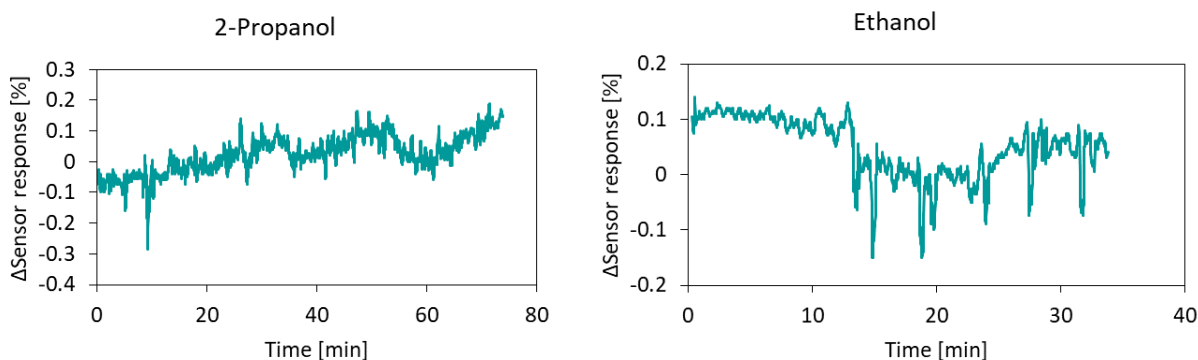
Figure 104: Selectivity tests with alcohols. Left: 2-propanol (100-1500-200 ppm). Right: Ethanol (1000 ppm).
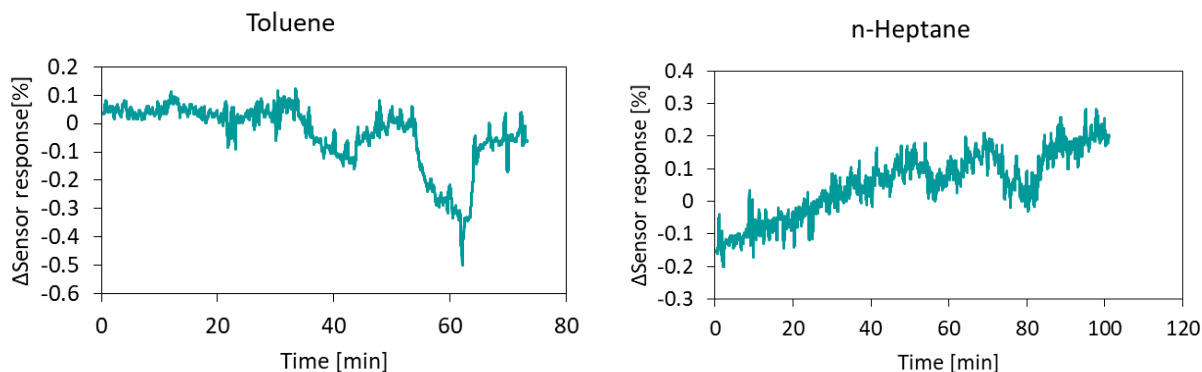
Figure 105: Selectivity tests. Left: Toluene (500-750-1000 ppm). Right: n-Heptane (750-1000 ppm).

To test the reproducibility and robustness of the chemiresistors coated with 10 wt. % P3HT, the acetophenone calibration curve was measured with those sensors three times: first after preparation of the sensors, then again after all abovementioned selectivity tests, and again after exposing the sensors to 65 % relative humidity (RH) for a prolonged time. Figure 106 shows the results. After the selectivity measurements, the sensor responses are lower than in the initial measurement with the average response for 300 ppm dropping from 3.6 to 2.1 % and the slope flatter from 0.0086 to 0.0064. Interestingly, the magnitude of the shifts increases again in the measurement performed after exposing the sensors to humid air, reaching almost the same values as in the first measurement with an average response of 3.0 % for 300 pm acetophenone. The slope of 0.0083 is similar to the one obtained in the measurements with the newly prepared sensors.
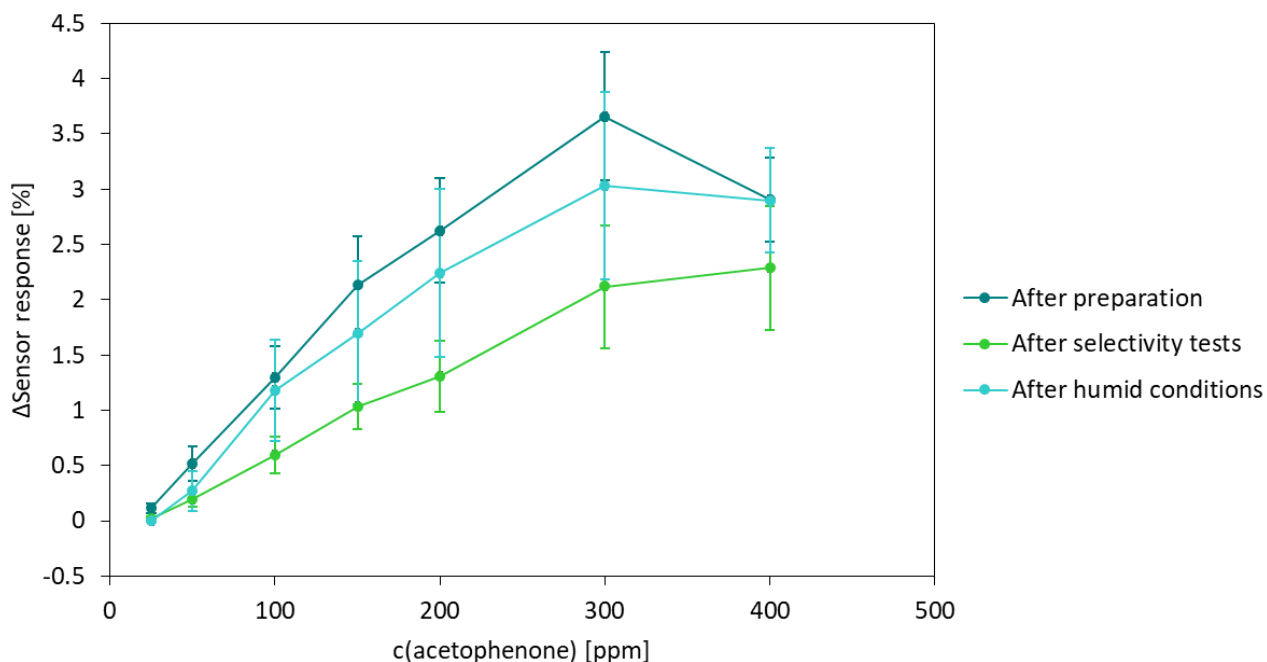
Figure 106: Calibration curves of chemiresistors measured directly after preparation, after selectivity tests and after exposition to humidity. n=5.

4.3.6. Surface Characterisation

Light Microscope

Both the non-conductive polymers and the blends were examined in a light microscope. Figure 107 shows the non-conductive MIP and NIP layers on QCM electrodes. There is no visible difference between MIP and NIP. Both polymers form smooth layers over the whole electrode surface.
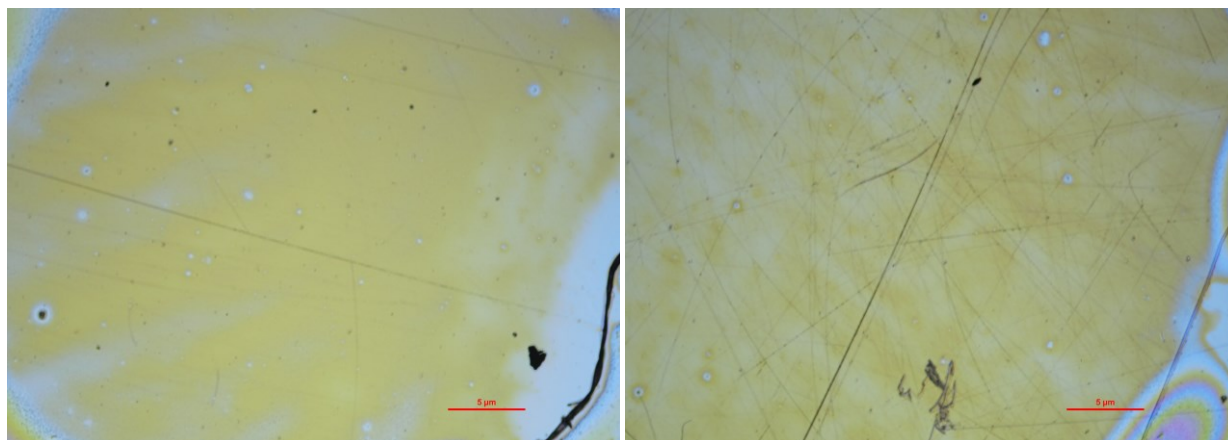
Figure 107: Microscope images of MAA-co-EGDMA MIP (left) and NIP (right). Scale bar: 200 μm.

P3HT tends to clump together in the undiluted blends. Figure 108 shows images of cMIP and cNIP containing 2.4 wt. % P3HT on QCM electrodes. This aggregation causes high average layer thickness, which is not beneficial for QCM sensing. Rough surface leads to increased unspecific adsorption and can distort the results. Additionally, it can cause high damping.
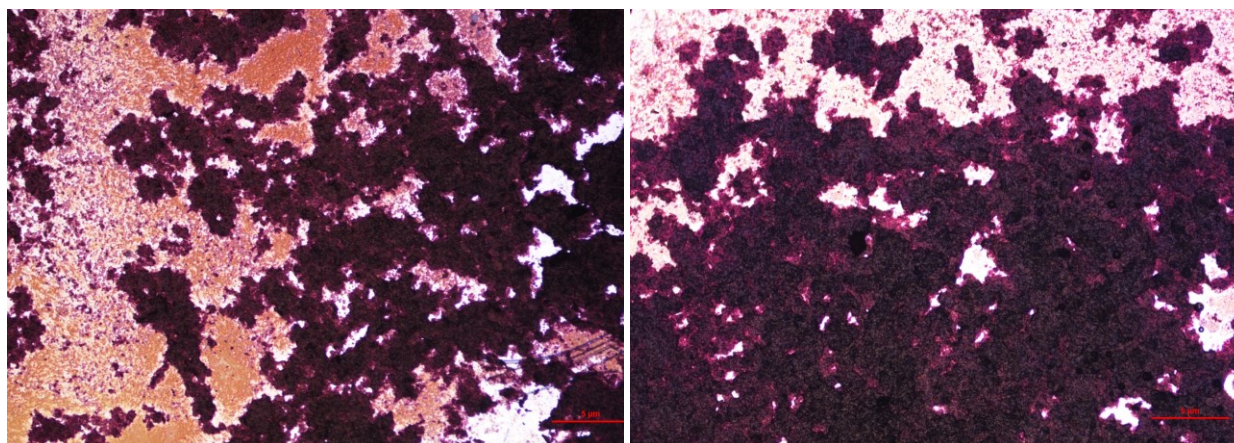
Figure 108: Microscope images of undiluted cMIP (left) and cNIP (right) blends containing 2.4 wt. % P3HT. Scale bar: 200 μm.

Diluted blends (Figure 109) form smoother, more homogeneous coatings, which is also reflected in thinner layers. No large aggregates of P3HT are visible in the images MIP and NIP look similar. The non-conductive oligomer solutions are very concentrated with only a small amount of solvent. Diluting with additional THF enhances solubility of P3HT in the blends.
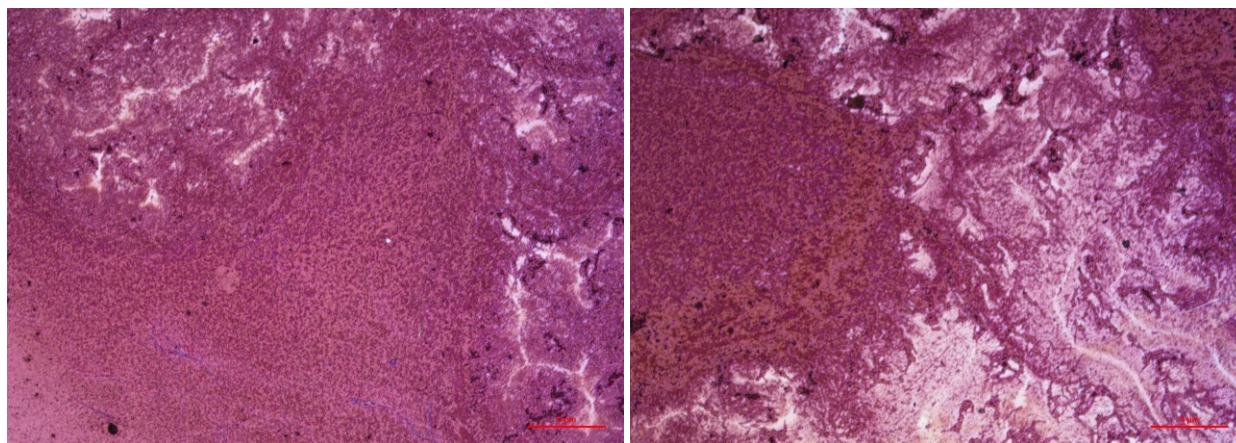
Figure 109: Microscope images of diluted cMIP (left) and cNIP (right) blends containing 2.4 wt. % P3HT. Scale bar: 200 µm.

AFM

AFM analysis of the non-conductive polymers (Figure 110) in contact mode reveals small pores on otherwise smooth surfaces. There is no observable difference between MIP and NIP.
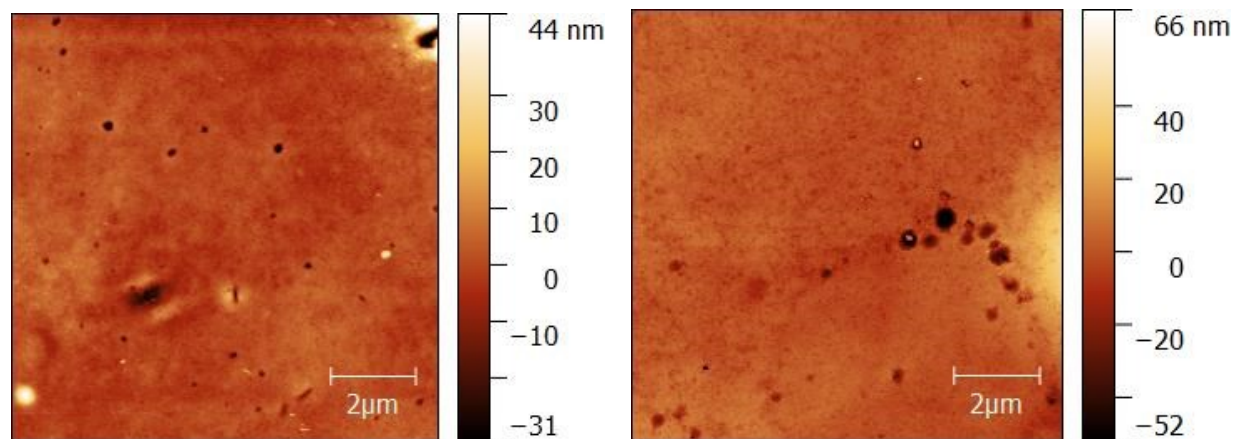
Figure 110: AFM images of MAA-co-EGDMA MIP (left) and NIP (right).

SEM analysis of the blends on chemiresistors reveals the structure of the underlying sensor. Figure 111 shows a chemiresistor coated with cMIP containing 10 wt. % P3HT with different magnifications. Screen printed gold electrodes with round structures appear elevated. In between, one can see the porous resin support. The polymer blend forms a thin layer over the whole surface that allows for seeing the features underneath. The SEM images show that the sensors are homogeneously coated.
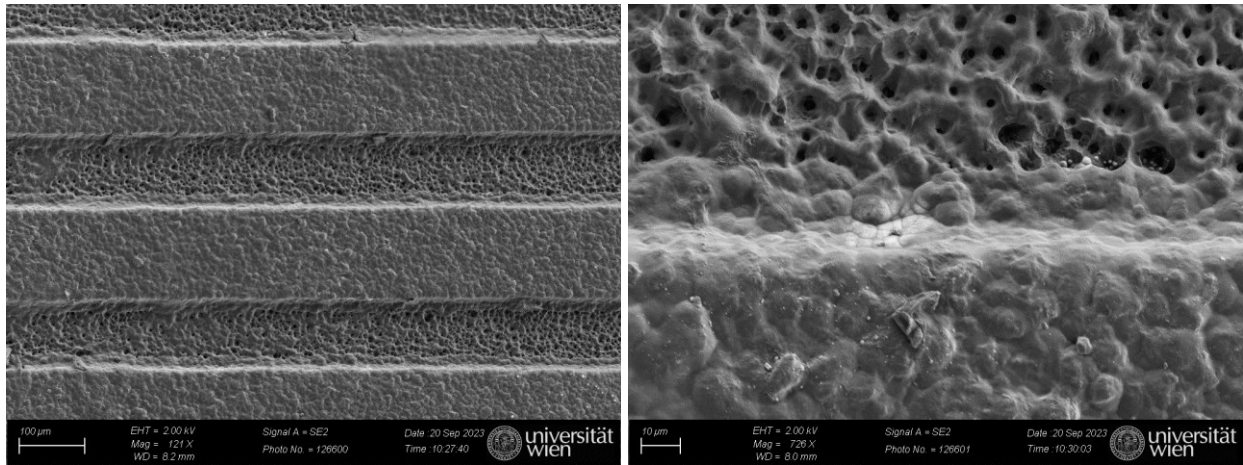
Figure 111: SEM images of cMIP blend containing 10 wt. % P3HT on chemiresistor.

5. Conclusion and Outlook

Within this project MIP-based sensors for the three VOCs 2-propanol, heptanal and acetophenone were developed. For this purpose, MIPs for the detection of the analytes on QCM were synthesised and optimised. Furthermore, blends were developed that can detect the VOCs on QCM as well as chemiresistors.

For the 2-propanol sensors, the PU synthesis protocol was initially optimised in terms of layer thickness. Then, adding a porogen to MIP and NIP and reducing the amount of template to one third of the total solvent volume used for MIP preparation further enhanced the QCM signals. Developing conductive blends proved challenging since the conductive polymer P3HT is insoluble in 2-propanol, which makes up a large amount of the solvent. Thus, it partly precipitates during cMIP synthesis. Nevertheless, the blends can be coated on both types of sensors, where rebinding of the analyte was tested in the range 1000 to 2500 ppm. On QCM the cMIPs show higher affinity to the analyte in this concentration range than the corresponding cNIPs with the imprinting effect increasing with increasing P3HT content. However, selectivity tests revealed that the same sensor responded to similar concentrations of different VOCs with larger frequency shifts than for 2-propanol. Since the selectivity studies for this particular chapter are very limited, it would make sense to explore this further. The developed sensors can detect 2-propanol with concentration-dependent responses but will most likely fail if tested in VOC mixtures. Chemiresistors coated with the PU/P3HT blends proved suitable for detecting higher concentrations of 2-propanol, but struggled to detect concentrations below 1500 ppm. Selectivity tests with 1-butanol resulted in irreversible baseline drift of the sensors. This will most likely reduce the lifetime of the sensors since it permanently alters the conductivity of the material. However, the impact of the presence of other VOC during 2-propanol detection with the chemiresistors was not assessed. In general, it would be recommendable to try preparing P3HT blends containing a lower amount of the conductive polymer than the one used in this thesis. This could also reduce the issue of P3HT precipitation which in turn would allow for more homogeneous coating. Alternatively, other conductive polymers which may be more soluble in 2-propanol could be tested. Given that the aim was preparing sensors which ultimately should be able to detect breast cancer biomarkers in exhaled breath which are present at low ppm to ppb levels, it is evident that the developed sensors cannot detect the analyte in a useful concentration range for this task. To be used for this application, the (c)MIPs require optimisation in terms of signal enhancement and selectivity. Preconcentration and purification of the sample could help bringing the 2-propanol to higher contents to detect it with the sensors.

The heptanal sensors relied on adapting a polymer based on MAA-*co*-EGDMA for synthesising MIP. After comparing several monomers, MAA was replaced by DMAA which offers interaction sites for the aldehyde via its amine group. Furthermore, the solvent was switched from DMSO to the more volatile THF. Like the 2-propanol sensors, blends with P3HT were prepared and tested on QCM as well as chemiresistors. Both types of sensors are able to detect the analyte in a range between 500 to 1000 ppm. However, like during 2-propanol measurements, the chemiresistors were better suited to detect the higher concentration, whereas the QCMs could detect the whole range. Selectivity tests with the conductive blends suggested good selectivity for heptanal with both types of sensors. Both QCM and chemiresistor showed lower responses to other VOCs compared to heptanal measurements. However, reproducing the heptanal MIPs proved difficult. Often the sensor responses varied among sensors of the same batch. Other issues include unclear results, where some sensors showed larger responses on the MIP-coated channels and the rest showed the opposite behaviour. Due to time limitations the origin of the inconsistency in sensor responses was not yet found and should be further explored before a reliable sensor can be developed with this composition. Furthermore, to apply the sensors in breath testing, lower concentration ranges must be targeted. Optimisation in terms of reaching lower concentrations is especially necessary for the chemiresistors, which so far only reliably detect 500 ppm and above.

The MAA-*co*-EGDMA MIP for acetophenone was optimised to obtain sufficiently thick layers on QCM. The P3HT blends were directly developed on the chemiresistors which allows for faster screening. With the broader spectrum of tested compositions, insights on the effect of the P3HT content in the blends was gained. Most sensors responded well in the tested range of 50-300 ppm. Some sensors could even detect the smallest measured concentration, which was 25 ppm. In comparison to the chemiresistors for the other two analytes, the acetophenone sensors responded surprisingly well in the lower concentration range. Sensors coated with low P3HT content saturated earlier than blends with higher content. However, except for the blend containing 1 wt. % P3HT all sensors showed signs of saturation above 300 ppm. Selectivity tests showed selectivity for acetophenone over other VOCs even at high concentrations of the interfering VOCs. Out of the three developed sensors, the acetophenone sensor has the best potential to be applied for breath analysis due to its detecting concentrations in the lower ppm range. Ideally, the detection limit should be lowered further. To increase affinity for the analyte, one can consider incorporating aromatic moieties such as styrene into the polymer to promote π-π stacking. Furthermore, the sensors must be tested in mixtures with other VOCs which given the results of the selectivity tests, should not be a challenge.

Abstract

Molecularly imprinted polymers (MIPs) are synthetic materials that contain binding sites for selectively rebinding a specific target analyte. In this work, MIPs and conductive MIP blends serve as receptor layers on quartz crystal microbalances (QCMs) and chemiresistors. QCMs are mass-sensitive sensors based on the piezoelectric properties of quartz. Chemiresistors can detect volatile organic compounds (VOCs) in the gas phase through thin conductive polymeric films. The analytes 2-propanol, heptanal and acetophenone are VOCs that are known breath biomarkers of breast cancer patients.

Rebinding experiments were conducted in gas flow containing different concentrations of the respective analytes as well as other VOCs to determine the selectivity of the material towards the target. QCM cMIP sensors can detect 2-propanol in a range of 1000 to 2500 ppm, heptanal from 250 to 1000 ppm. QCM sensors for acetophenone were successfully tested in a range of 50 to 200 ppm. The corresponding chemiresistors respond to 2-propanol and heptanal in the same range as the QCMs. However, reliable responses can only be obtained at higher concentrations, starting at 1500 ppm 2-propanol and 750 ppm heptanal, respectively. Chemiresistors for acetophenone can detect the analyte in a broad range of 25 to 400 ppm with a linear range between 50 and 300 ppm. All described systems lead to concentration-dependent signals when exposed to the desired analyte. Selectivity tests suggest good selectivity for the heptanal and acetophenone sensors. The 2-propanol sensors also respond to other analytes, especially other alcohols, which is expected due to the small size and lack of functional groups of the target analyte.

Zusammenfassung

Molekular geprägte Polymere (MIPs) sind synthetische Materialien, die Bindungsstellen zur selektiven Erkennung eines Zielanalyten enthalten. In dieser Arbeit dienen MIPs und leitfähige MIP-Verblendungen als Rezeptorschichten auf Quarzkristall-Mikrowaagen (QCMs) und Chemiresistoren. QCMs sind massensensitive Sensoren, die auf den piezoelektrischen Eigenschaften von Quarz basieren. Chemiresistoren können flüchtige organische Verbindungen (VOCs) in der Gasphase durch dünne leitfähige Polymerfilme detektieren. Die Analyten 2-Propanol, Heptanal und Acetophenon sind VOCs, die bekannte Biomarker in der Atemluft von Brustkrebspatientinnen sind.

Um die Selektivität der Materialien gegenüber der Zielanalyten zu bestimmen, wurden Sensormessungen im Gasstrom, mit unterschiedlichen Konzentrationen der jeweiligen Analyten sowie anderer VOCs durchgeführt. QCM cMIP-Sensoren können 2-Propanol in einem Bereich von 1000 bis 2500 ppm und Heptanal von 250 bis 1000 ppm nachweisen. QCM-Sensoren für Acetophenon wurden im Bereich von 50 bis 200 ppm erfolgreich getestet. Die entsprechenden Chemiresistoren reagieren auf 2-Propanol und Heptanal im gleichen Bereich wie die QCMs. Zuverlässige Ergebnisse können jedoch ab 1500 ppm 2-Propanol bzw. ab 750 ppm Heptanal erhalten werden. Chemiresistoren für Acetophenon können den Analyten in einem breiten Bereich von 25 bis 400 ppm mit einem linearen Bereich zwischen 50 und 300 ppm nachweisen. Alle beschriebenen Systeme reagieren konzentrationsabhängig auf den gewünschten Analyten. Selektivitätstests deuten auf eine gute Selektivität der Heptanal- und Acetophenon-Sensoren hin. Die 2-Propanol-Sensoren reagieren auch auf andere Analyte, insbesondere auf andere Alkohole, was aufgrund der geringen Größe und des Fehlens funktioneller Gruppen des Zielanalyten zu erwarten ist.

References

1.   Haupt, K.; Medina Rangel, P.X.; Bui, B.T.S. Molecularly Imprinted Polymers: Antibody Mimics for Bioimaging and Therapy. *Chem. Rev.* **2020**, *120*, 9554–9582, doi:10.1021/acs.chemrev.0c00428.

2.   Ávila, M.; Zougagh, M.; Ríos, Á.; Escarpa, A. Molecularly Imprinted Polymers for Selective Piezoelectric Sensing of Small Molecules. *TrAC - Trends Anal. Chem.* **2008**, *27*, 54–65, doi:10.1016/j.trac.2007.10.009.

3.   Diltemiz, S.E.; Keçili, R.; Ersöz, A.; Say, R. Molecular Imprinting Technology in Quartz Crystal Microbalance (QCM) Sensors. *Sensors (Switzerland)* **2017**, *17*, doi:10.3390/s17030454.

4.   Buensuceso, C.E.; Tiu, B.D.B.; Lee, L.P.; Sabido, P.M.G.; Nuesca, G.M.; Caldona, E.B.; del Mundo, F.R.; Advincula, R.C. Electropolymerized-Molecularly Imprinted Polymers (E-MIPS) as Sensing Elements for the Detection of Dengue Infection. *Anal. Bioanal. Chem.* **2022**, *414*, 1347–1357, doi:10.1007/s00216-021-03757-y.

5.   Çiçek, Ç.; Yilmaz, F.; Özgür, E.; Yavuz, H.; Denizli, A. Molecularly Imprinted Quartz Crystal Microbalance Sensor (QCM) for Bilirubin Detection. *Chemosensors* **2016**, *4*, doi:10.3390/chemosensors4040021.

6.   Uludağ, Y.; Piletsky, S.A.; Turner, A.P.F.; Cooper, M.A. Piezoelectric Sensors Based on Molecular Imprinted Polymers for Detection of Low Molecular Mass Analytes. *FEBS J.* **2007**, *274*, 5471–5480, doi:10.1111/j.1742-4658.2007.06079.x.

7.   Kumpf, K.; Trattner, S.; Aspermair, P.; Bintinger, J.; Fruhmann, P. P3HT and PEDOT:PSS Printed Thin Films on Chemiresistors: An Economic and Versatile Tool for Ammonia and Humidity Monitoring Applications. *J. Appl. Polym. Sci.* **2023**, *140*, doi:10.1002/app.53733.

8.   Feldner, A.; Völkle, J.; Lieberzeit, P.; Fruhmann, P. Conductive Molecularly Imprinted Polymers (CMIPs): Rising and Versatile Key Elements in Chemical Sensing. *Chemosensors* **2023**, *11*, 1–26, doi:10.3390/chemosensors11050299.

9.   Shirasu, M.; Touhara, K. The Scent of Disease: Volatile Organic Compounds of the Human Body Related to Disease and Disorder. *J. Biochem.* **2011**, *150*, 257–266, doi:10.1093/jb/mvr090.

10. Hanna, G.B.; Boshier, P.R.; Markar, S.R.; Romano, A. Accuracy and Methodologic Challenges of Volatile Organic Compound-Based Exhaled Breath Tests for Cancer Diagnosis: A Systematic Review and Meta-Analysis. *JAMA Oncol.* **2019**, *5*, 1–11, doi:10.1001/jamaoncol.2018.2815.

11. Phillips, M.; Cataneo, R.N.; Ditkoff, B.A.; Fisher, P.; Greenberg, J.; Gunawardena, R.; Kwon, C.S.; Tietje, O.; Wong, C. Prediction of Breast Cancer Using Volatile Biomarkers in the Breath. *Breast Cancer Res. Treat.* **2006**, *99*, 19–21, doi:10.1007/s10549-006-9176-1.

12. Hulanicki, A.; Glab, S.; Ingman, F. Chemical Sensors Definitions and Classification. *Pure Appl. Chem.* **1991**, *63*, 1247–1250, doi:10.1351/pac199163091247.

13. Lowdon, J.W.; Diliën, H.; Singla, P.; Peeters, M.; Cleij, T.J.; van Grinsven, B.; Eersels, K. MIPs for Commercial Application in Low-Cost Sensors and Assays – An Overview of the Current Status Quo. *Sensors Actuators, B Chem.* **2020**, *325*, doi:10.1016/j.snb.2020.128973.

14. Mujahid, A.; Dickert, F.L. Surface Acousticwave (SAW) for Chemical Sensing Applications of Recognition Layers. *Sensors (Switzerland)* **2017**, *17*, 1–26, doi:10.3390/s17122716.

15. MUJAHID, A.; AFZAL, A.; DICKERT, F.L. An Overview of High Frequency Acoustic—QCMs, SAWs and FBARs—Chemical and Biochemical Applications. *Sensors* **2019**, *19*, 4395.

16. Sauerbrey, G. Verwendung von Schwingquarzen Zur Wägung Dünner Schichten Und Zur Mikrowägung. *Zeitschrift für Phys.* **1959**, *155*, 206–222, doi:https://doi.org/10.1007/BF01337937.

17. Keiji Kanazawa, K.; Gordon, J.G. The Oscillation Frequency of a Quartz Resonator in Contact with Liquid. *Anal. Chim. Acta* **1985**, *175*, 99–105, doi:10.1016/S0003-2670(00)82721-X.

18. Chen, Q.; Xu, S.; Liu, Q.; Masliyah, J.; Xu, Z. QCM-D Study of Nanoparticle Interactions. *Adv. Colloid Interface Sci.* 2016, *233*, 94–114.

19. Lieberzeit, P.A.; Glanznig, G.; Jenik, M.; Gazda-Miarecka, S.; Dickert, F.L.; Leidl, A. Softlithography in Chemical Sensing - Analytes from Molecules to Cells. *Sensors* **2005**, *5*, 509–518, doi:10.3390/s5120509.

20. Lange, U.; Roznyatovskaya, N. V.; Mirsky, V.M. Conducting Polymers in Chemical Sensors and Arrays. *Anal. Chim. Acta* 2008, *614*, 1–26.

21.   Yang, S.; Bintinger, J.; Park, S.; Jain, S.; Alexandrou, K.; Fruhmann, P.; Besar, K.; Katz, H.; Kymissis, I. Inexpensive, Versatile, and Robust USB-Driven Sensor Platform. *IEEE Sensors Lett.* **2017**, *1*, 17–20, doi:10.1109/LSENS.2017.2763989.

22.   Cowen, T.; Cheffena, M. Template Imprinting Versus Porogen Imprinting of Small Molecules: A Review of Molecularly Imprinted Polymers in Gas Sensing. *Int. J. Mol. Sci.* **2022**, *23*, doi:10.3390/ijms23179642.

23.   Kadhem, A.J.; Gentile, G.J.; de Cortalezzi, M.M.F. *Molecularly Imprinted Polymers (Mips) in Sensors for Environmental and Biomedical Applications: A Review*; 2021; Vol. 26; ISBN 1573884677.

24.   Polyakov, M. V; Kuleshina, L.; Neimark, I. On the Dependence of Silica Gel Adsorption Properties on the Character of Its Porosity. *Zhurnal Fizieskoj Khimii/Akademiya SSSR* **1937**, 100–112.

25.   Dickey, F.H. The Preparation of Specific Adsorbents. *Proc. Natl. Acad. Sci. U. S. A.* **1949**, *35*, 227–229, doi:10.1073/pnas.35.5.227.

26.   Wulff, G. Fourty Years of Molecular Imprinting in Synthetic Polymers: Origin, Features and Perspectives. *Microchim. Acta* **2013**, *180*, 1359–1370, doi:10.1007/s00604-013-0992-9.

27.   Chen, L.; Wang, X.; Lu, W.; Wu, X.; Li, J. Molecular Imprinting: Perspectives and Applications. *Chem. Soc. Rev.* **2016**, *45*, 2137–2211, doi:10.1039/c6cs00061d.

28.   Haghdoust, S.; Arshad, U.; Mujahid, A.; Schranzhofer, L.; Lieberzeit, P.A. Development of a MIP-Based QCM Sensor for Selective Detection of Penicillins in Aqueous Media. *Chemosensors* **2021**, *9*, doi:10.3390/chemosensors9120362.

29.   Rebelo, T.S.C.R.; Costa, R.; Brandão, A.T.S.C.; Silva, A.F.; Sales, M.G.F.; Pereira, C.M. Molecularly Imprinted Polymer SPE Sensor for Analysis of CA-125 on Serum. *Anal. Chim. Acta* **2019**, *1082*, 126–135, doi:10.1016/j.aca.2019.07.050.

30.   Alizadeh, T.; Rezaloo, F. Toluene Chemiresistor Sensor Based on Nano-Porous Toluene-Imprinted Polymer. *Int. J. Environ. Anal. Chem.* **2013**, *93*, 919–934, doi:10.1080/03067319.2012.708744.

31.   Liu, Y.; Hoshina, K.; Haginaka, J. Monodispersed, Molecularly Imprinted Polymers for Cinchonidine by Precipitation Polymerization. *Talanta* **2010**, *80*, 1713–1718, doi:10.1016/j.talanta.2009.10.011.

32. Shen, X.; Zhou, T.; Ye, L. Molecular Imprinting of Protein in Pickering Emulsion. *Chem. Commun.* **2012**, *48*, 8198–8200, doi:10.1039/c2cc33572g.

33. Canfarotta, F.; Poma, A.; Guerreiro, A.; Piletsky, S. Solid-Phase Synthesis of Molecularly Imprinted Nanoparticles. *Nat. Protoc.* **2016**, *11*, 443–455, doi:10.1038/nprot.2016.030.

34. Metilda, P.; Prasad, K.; Kala, R.; Gladis, J.M.; Rao, T.P.; Naidu, G.R.K. Ion Imprinted Polymer Based Sensor for Monitoring Toxic Uranium in Environmental Samples. *Anal. Chim. Acta* **2007**, *582*, 147–153, doi:10.1016/j.aca.2006.08.052.

35. Wang, H.; Shang, H.; Sun, X.; Hou, L.; Wen, M.; Qiao, Y. Preparation of Thermo-Sensitive Surface Ion-Imprinted Polymers Based on Multi-Walled Carbon Nanotube Composites for Selective Adsorption of Lead(II) Ion. *Colloids Surfaces A Physicochem. Eng. Asp.* **2020**, *585*, doi:10.1016/j.colsurfa.2019.124139.

36. Bajwa, S.Z.; Mustafa, G.; Samardzic, R.; Wangchareansak, T.; Lieberzeit, P.A. Nanostructured Materials with Biomimetic Recognition Abilities for Chemical Sensing. *Nanoscale Res. Lett.* **2012**, *7*, 1–7, doi:10.1186/1556-276X-7-328.

37. Li, T.H.; Wang, D.; Lan, H.Z.; Gan, N. Determination of 17β-Estradiol Based on Electropolymerized-Molecularly Imprinted Polymer on Gold Nanoparticles-Graphene Modified Electrode. In Proceedings of the Advanced Materials Research; 2014; Vol. 881–883, pp. 93–97.

38. Völkle, J.; Kumpf, K.; Feldner, A.; Lieberzeit, P.; Fruhmann, P. Development of Conductive Molecularly Imprinted Polymers (CMIPs) for Limonene to Improve and Interconnect QCM and Chemiresistor Sensing. *Sensors Actuators B Chem.* **2022**, *356*, doi:10.1016/j.snb.2021.131293.

39. Cai, D.; Ren, L.; Zhao, H.; Xu, C.; Zhang, L.; Yu, Y.; Wang, H.; Lan, Y.; Roberts, M.F.; Chuang, J.H.; et al. A Molecular-Imprint Nanosensor for Ultrasensitive Detection of Proteins. *Nat. Nanotechnol.* **2010**, *5*, 597–601, doi:10.1038/nnano.2010.114.

40. Ferreira, N.S.; Moreira, A.P.T.; de Sá, M.H.M.; Sales, M.G.F. New Electrochemically-Derived Plastic Antibody on a Simple Conductive Paper Support for Protein Detection: Application to BSA. *Sensors Actuators, B Chem.* **2017**, *243*, 1127–1136, doi:10.1016/j.snb.2016.12.074.

41. Sasaki, S.; Ooya, T.; Kitayama, Y.; Takeuchi, T. Molecularly Imprinted Protein Recognition Thin Films

Constructed by Controlled/Living Radical Polymerization. *J. Biosci. Bioeng.* **2015**, *119*, 200–205, doi:10.1016/j.jbiosc.2014.06.019.

42.   Seidler, K.; Polreichová, M.; Lieberzeit, P.A.; Dickert, F.L. Biomimetic Yeast Cell Typing - Application of QCMs. *Sensors* **2009**, *9*, 8146–8157, doi:10.3390/s91008146.

43.   Jamieson, O.; Betlem, K.; Mansouri, N.; Crapnell, R.D.; Vieira, F.S.; Hudson, A.; Banks, C.E.; Liauw, C.M.; Gruber, J.; Zubko, M.; et al. Electropolymerised Molecularly Imprinted Polymers for the Heat-Transfer Based Detection of Microorganisms: A Proof-of-Concept Study Using Yeast. *Therm. Sci. Eng. Prog.* **2021**, *24*, doi:10.1016/j.tsep.2021.100956.

44.   Spieker, E.; Lieberzeit, P.A. Molecular Imprinting Studies for Developing QCM-Sensors for Bacillus Cereus. *Procedia Eng.* **2016**, *168*, 561–564, doi:10.1016/j.proeng.2016.11.525.

45.   Bräuer, B.; Werner, M.; Baurecht, D.; Lieberzeit, P.A. Raman and Scanning Probe Microscopy for Differentiating Surface Imprints of E. Coli and B. Cereus. *J. Mater. Chem. B* **2022**, 6758–6767, doi:10.1039/d2tb00283c.

46.   Bräuer, B.; Thier, F.; Bittermann, M.; Baurecht, D.; Lieberzeit, P.A. Raman Studies on Surface-Imprinted Polymers to Distinguish the Polymer Surface, Imprints, and Different Bacteria. *ACS Appl. Bio Mater.* **2022**, *5*, 160–171, doi:10.1021/acsabm.1c01020.

47.   Unger, C.; Lieberzeit, P.A. Molecularly Imprinted Thin Film Surfaces in Sensing: Chances and Challenges. *React. Funct. Polym.* **2021**, *161*, 104855, doi:10.1016/j.reactfunctpolym.2021.104855.

48.   Khumsap, T.; Corpuz, A.; Nguyen, L.T. Epitope-Imprinted Polymers: Applications in Protein Recognition and Separation. *RSC Adv.* **2021**, *11*, 11403–11414, doi:10.1039/d0ra10742e.

49.   Pardeshi, S.; Dhodapkar, R.; Kumar, A. Influence of Porogens on the Specific Recognition of Molecularly Imprinted Poly(Acrylamide-Co-Ethylene Glycol Dimethacrylate). *Compos. Interfaces* **2014**, *21*, 13–30, doi:10.1080/15685543.2013.830515.

50.   Janfaza, S.; Kim, E.; O'Brien, A.; Najjaran, H.; Nikkhah, M.; Alizadeh, T.; Hoorfar, M. A Nanostructured Microfluidic Artificial Olfaction for Organic Vapors Recognition. *Sci. Rep.* **2019**, *9*, 1–8, doi:10.1038/s41598-019-55672-z.

51.   Chen, B.; Liu, C.; Hayashi, K. Selective Terpene Vapor Detection Using Molecularly Imprinted Polymer Coated Au Nanoparticle LSPR Sensor. *IEEE Sens. J.* **2014**, *14*, 3458–3464, doi:10.1109/JSEN.2014.2346187.

52.   Shim, D.Y.; Chang, S.M.; Kim, J.M. Development of Fast Resettable Gravimetric Aromatic Gas Sensors Using Quartz Crystal Microbalance. *Sensors Actuators, B Chem.* **2021**, *329*, 129143, doi:10.1016/j.snb.2020.129143.

53.   Sakale, G.; Knite, M.; Teteris, V.; Tupureina, V.; Stepina, S.; Liepa, E. The Investigation of Sensing Mechanism of Ethanol Vapour in Polymer-Nanostructured Carbon Composite. *Cent. Eur. J. Phys.* **2011**, *9*, 307–312, doi:10.2478/s11534-010-0110-0.

54.   Grate, J.W.; Abraham, M.H. Solubility Interactions and the Design of Chemically Selective Sorbent Coatings for Chemical Sensors and Arrays. *Sensors Actuators B. Chem.* **1991**, *3*, 85–111, doi:10.1016/0925-4005(91)80202-U.

55.   Joly, C.; Le Cerf, D.; Chappey, C.; Langevin, D.; Muller, G. Residual Solvent Effect on the Permeation Properties of Fluorinated Polyimide Films. *Sep. Purif. Technol.* **1999**, *16*, 47–54, doi:10.1016/S1383-5866(98)00118-X.

56.   Tsuchiizu, A.; Hasegawa, T.; Katsumoto, Y. Water Sorption on a Thin Film of Stereocontrolled Poly(N -Ethylacrylamide) and Poly(N,N -Diethylacrylamide). *MATEC Web Conf.* **2013**, *4*, 2–5, doi:10.1051/matecconf/20130403001.

57.   Tominaga, Y.; Kubo, T.; Yasuda, K.; Kato, K.; Hosoya, K. Development of Molecularly Imprinted Porous Polymers for Selective Adsorption of Gaseous Compounds. *Microporous Mesoporous Mater.* **2012**, *156*, 161–165, doi:10.1016/j.micromeso.2012.02.020.

58.   Charello, M.; Anfossi, L.; Cavalera, S.; Di Nardo, F.; Artusio, F.; Pisano, R.; Baggiani, C. Effect of Polymerization Time on the Binding Properties of Ciprofloxacin-Imprinted Nanomips Prepared by Solid-Phase Synthesis. *Polymers (Basel).* **2021**, *13*, doi:10.3390/polym13162656.

59.   Pratama, K.F.; Manik, M.E.R.; Rahayu, D.; Hasanah, A.N. Effect of the Molecularly Imprinted Polymer Component Ratio on Analytical Performance. *Chem. Pharm. Bull.* **2020**, *68*, 1013–1024, doi:10.1248/cpb.c20-00551.

60. Chen, B.; Liu, C.; Sun, X.; Hayashi, K. Molecularly Imprinted Polymer Coated Au Nanoparticle Sensor for α-Pinene Vapor Detection. *Proc. IEEE Sensors* **2013**, 1–4, doi:10.1109/ICSENS.2013.6688152.

61. Hasanah, A.N.; Safitri, N.; Zulfa, A.; Neli, N.; Rahayu, D. Factors Affecting Preparation of Molecularly Imprinted Polymer and Methods on Finding Template-Monomer Interaction as the Key of Selective Properties of the Materials. *Molecules* **2021**, *26*, doi:10.3390/molecules26185612.

62. Han, Z.; Xu, Y.; Wang, H.; Tian, H.; Qiu, B.; Sun, D. Synthesis of Ammonia Molecularly Imprinted Adsorbents and Ammonia Adsorption Separation during Sludge Aerobic Composting. *Bioresour. Technol.* **2020**, *300*, 122670, doi:10.1016/j.biortech.2019.122670.

63. Percival, C.J.; Stanley, S.; Galle, M.; Braithwaite, A.; Newton, M.I.; McHale, G.; Hayes, W. Molecular-Imprinted, Polymer-Coated Quartz Crystal Microbalances for the Detection of Terpenes. *Anal. Chem.* **2001**, *73*, 4225–4228, doi:10.1021/ac0155198.

64. Ghatak, B.; Ali, S.B.; Naskar, H.; Tudu, B.; Pramanik, P.; Mukherji, S.; Bandyopadhyay, R. Selective and Sensitive Detection of Limonene in Mango Using Molecularly Imprinted Polymer Based Quartz Crystal Microbalance Sensor. *ISOEN 2019 - 18th Int. Symp. Olfaction Electron. Nose, Proc.* **2019**, 19–21, doi:10.1109/ISOEN.2019.8823318.

65. Wen, T.; Nie, Q.; Han, L.; Gong, Z.; Li, D.; Ma, Q.; Wang, Z.; He, W.; Wen, L.; Peng, H. Molecularly Imprinted Polymers-Based Piezoelectric Coupling Sensor for the Rapid and Nondestructive Detection of Infested Citrus. *Food Chem.* **2022**, *387*, 132905, doi:10.1016/j.foodchem.2022.132905.

66. Chul Yang, J.; Won Hong, S.; Jeon, S.; Ik Park, W.; Byun, M.; Park, J. Molecular Imprinting of Hemispherical Pore-Structured Thin Films via Colloidal Lithography for Gaseous Formaldehyde Gravimetric Sensing. *Appl. Surf. Sci.* **2021**, *570*, 151161, doi:10.1016/j.apsusc.2021.151161.

67. Alizadeh, T.; Hamedsoltani, L. Graphene/Graphite/Molecularly Imprinted Polymer Nanocomposite as the Highly Selective Gas Sensor for Nitrobenzene Vapor Recognition. *J. Environ. Chem. Eng.* **2014**, *2*, 1514–1526, doi:10.1016/j.jece.2014.07.007.

68. Marx, S.; Zaltsman, A.; Turyan, I.; Mandler, D. Parathion Sensor Based on Molecularly Imprinted

Sol-Gel Films. *Anal. Chem.* **2004**, *76*, 120–126, doi:10.1021/ac034531s.

69. Chen, M.; Zhang, Y.; Zhang, J.; Li, K.; Lv, T.; Shen, K.; Zhu, Z.; Liu, Q. Facile Lotus-Leaf-Templated Synthesis and Enhanced Xylene Gas Sensing Properties of Ag-LaFeO3 Nanoparticles. *J. Mater. Chem. C* **2018**, *6*, 6138–6145, doi:10.1039/c8tc01402g.

70. Hussain, M.; Kotova, K.; Lieberzeit, P.A. Molecularly Imprinted Polymer Nanoparticles for Formaldehyde Sensing with QCM. *Sensors (Switzerland)* **2016**, *16*, doi:10.3390/s16071011.

71. Palaprat, G.; Mingotaud, A.F.; Langevin, D.; Mauzac, M.; Marty, J.D. Molecularly Imprinted Cholesteric Materials for Enhanced Enantiomeric Separation. *Polymer (Guildf).* **2022**, *243*, 124654, doi:10.1016/j.polymer.2022.124654.

72. Anfossi, L.; Cavalera, S.; Di Nardo, F.; Spano, G.; Giovannoli, C.; Baggiani, C. Delayed Addition of Template Molecules Enhances the Binding Properties of Diclofenac-Imprinted Polymers. *Polymers (Basel).* **2020**, *12*, doi:10.3390/POLYM12051178.

73. Koudehi, M.F.; Pourmortazavi, S.M.; Zibaseresht, R.; Mirsadeghi, S. << MEMS-Based PVA/PPy/MIP Polymeric- Nanofiber Sensor Fabricated by LIFT-OFF Process for Detection 2,4-Dinitrotoluene Vapor. *IEEE Sens. J.* **2021**, *21*, 9492–9499, doi:10.1109/JSEN.2021.3055797.

74. Huang, Y.; Wang, R. Highly Selective Separation of H2S and CO2 Using a H2S-Imprinted Polymers Loaded on a Polyoxometalate@Zr-Based Metal-Organic Framework with a Core-Shell Structure at Ambient Temperature. *J. Mater. Chem. A* **2019**, *7*, 12105–12114, doi:10.1039/c9ta01749f.

75. Haupt, K.; Linares, A.V.; Bompart, M.; Bui, B.T.S. *Molecular Imprinting. Topics in Current Chemistry, Vol 325*; 2011; ISBN 9783642284205.

76. Otto, B. Das Di-Isocyanat-Polyadditionsverfahren (Polyurethane). *Angew. Chemie* **1947**, *59*, 257–272, doi:https://doi.org/10.1002/ange.19470590901.

77. Akindoyo, J.O.; Beg, M.D.H.; Ghazali, S.; Islam, M.R.; Jeyaratnam, N.; Yuvaraj, A.R. Polyurethane Types, Synthesis and Applications-a Review. *RSC Adv.* **2016**, *6*, 114453–114482, doi:10.1039/c6ra14525f.

78. Dickert, F.L.; Lieberzeit, P.A.; Achatz, P.; Palfinger, C.; Fassnauer, M.; Schmid, E.; Werther, W.;

Horner, G. QCM Array for On-Line-Monitoring of Composting Procedures. *Analyst* **2004**, *129*, 432–437, doi:10.1039/b315356h.

79.   Jenik, M.; Seifner, A.; Lieberzeit, P.; Dickert, F.L. Pollen-Imprinted Polyurethanes for QCM Allergen Sensors. *Anal. Bioanal. Chem.* **2009**, *394*, 523–528, doi:10.1007/s00216-009-2718-8.

80.   Findeisen, A.; Wackerlig, J.; Samardzic, R.; Pitkänen, J.; Anttalainen, O.; Dickert, F.L.; Lieberzeit, P.A. Artificial Receptor Layers for Detecting Chemical and Biological Agent Mimics. *Sensors Actuators, B Chem.* **2012**, *170*, 196–200, doi:10.1016/j.snb.2011.08.025.

81.   Sajini, T.; Mathew, B. A Brief Overview of Molecularly Imprinted Polymers: Highlighting Computational Design, Nano and Photo-Responsive Imprinting. *Talanta Open* **2021**, *4*, 100072, doi:10.1016/j.talo.2021.100072.

82.   Bolto, B.A.; Weiss Electronic Conduction in Polymers. II. The Electrochemical Reduction of Polypyrrole at Controlled Potential. *Aust. J. Chem.* **1963**, *16*, 1076–1089, doi:10.1071/CH9631076.

83.   Shirakawa, H.; Louis, E.J.; MacDiarmid, A.G.; Chiang, C.K.; Heeger, A.J. Synthesis of Electrically Conducting Organic Polymers: Halogen Derivatives of Polyacetylene{,} (CH). *J. Chem. Soc.{,} Chem. Commun.* **1977**, 578–580, doi:10.1039/C39770000578.

84.   Rasmussen, S.C. Early History of Polypyrrole : The First Conducting Organic Polymer. *Bull. Hist. Chem.* **2015**, *40*, 45–55.

85.   Gangopadhyay, R.; De, A. Conducting Polymer Nanocomposites: A Brief Overview. *Chem. Mater.* **2000**, *12*, 608–622, doi:10.1021/cm990537f.

86.   Schadler, L.S.; Brinson, L.C.; Sawyer, W.G. Polymer Nanocomposites: A Small Part of the Story. *Jom* **2007**, *59*, 53–60, doi:10.1007/s11837-007-0040-5.

87.   Anantha-Iyengar, G.; Shanmugasundaram, K.; Nallal, M.; Lee, K.P.; Whitcombe, M.J.; Lakshmi, D.; Sai-Anand, G. Functionalized Conjugated Polymers for Sensing and Molecular Imprinting Applications. *Prog. Polym. Sci.* 2019, *88*, 1–129.

88.   Blanco-López, M.C.; Gutiérrez-Fernández, S.; Lobo-Castañón, M.J.; Miranda-Ordieres, A.J.; Tuñón-Blanco, P. Electrochemical Sensing with Electrodes Modified with Molecularly Imprinted Polymer

Films. *Anal. Bioanal. Chem.* **2004**, *378*, 1922–1928, doi:10.1007/s00216-003-2330-2.

89.   Sharma, P.S.; Pietrzyk-Le, A.; D'Souza, F.; Kutner, W. Electrochemically Synthesized Polymers in Molecular Imprinting for Chemical Sensing. *Anal. Bioanal. Chem.* **2012**, *402*, 3177–3204, doi:10.1007/s00216-011-5696-6.

90.   Martins, G. V.; Marques, A.C.; Fortunato, E.; Sales, M.G.F. Paper-Based (Bio)Sensor for Label-Free Detection of 3-Nitrotyrosine in Human Urine Samples Using Molecular Imprinted Polymer. *Sens. Bio-Sensing Res.* **2020**, *28*, doi:10.1016/j.sbsr.2020.100333.

91.   Yin, F.; Mo, Y.; Liu, X.; Yang, H.; Zhou, D.; Cao, H.; Ye, T.; Xu, F. An Ultra-Sensitive and Selective Electrochemical Sensor Based on GOCS Composite and Ion Imprinted Polymer for the Rapid Detection of Cd2+ in Food Samples. *Food Chem.* **2023**, *410*, doi:10.1016/j.foodchem.2022.135293.

92.   Bai, X.; Zhang, B.; Liu, M.; Hu, X.; Fang, G.; Wang, S. Molecularly Imprinted Electrochemical Sensor Based on Polypyrrole/Dopamine@graphene Incorporated with Surface Molecularly Imprinted Polymers Thin Film for Recognition of Olaquindox. *Bioelectrochemistry* **2020**, *132*, doi:10.1016/j.bioelechem.2019.107398.

93.   Ma, X.; Gao, F.; Dai, R.; Liu, G.; Zhang, Y.; Lu, L.; Yu, Y. Novel Electrochemical Sensing Platform Based on a Molecularly Imprinted Polymer-Decorated 3D-Multi-Walled Carbon Nanotube Intercalated Graphene Aerogel for Selective and Sensitive Detection of Dopamine. *Anal. Methods* **2020**, *12*, 1845–1851, doi:10.1039/d0ay00033g.

94.   Ma, X.; Tu, X.; Gao, F.; Xie, Y.; Huang, X.; Fernandez, C.; Qu, F.; Liu, G.; Lu, L.; Yu, Y. Hierarchical Porous MXene/Amino Carbon Nanotubes-Based Molecular Imprinting Sensor for Highly Sensitive and Selective Sensing of Fisetin. *Sensors Actuators, B Chem.* **2020**, *309*, doi:10.1016/j.snb.2020.127815.

95.   Wang, Z.; Li, H.; Chen, J.; Xue, Z.; Wu, B.; Lu, X. Acetylsalicylic Acid Electrochemical Sensor Based on PATP-AuNPs Modified Molecularly Imprinted Polymer Film. *Talanta* **2011**, *85*, 1672–1679, doi:10.1016/j.talanta.2011.06.067.

96.   Essousi, H.; Barhoumi, H.; Bibani, M.; Ktari, N.; Wendler, F.; Al-Hamry, A.; Kanoun, O. Ion-Imprinted Electrochemical Sensor Based on Copper Nanoparticles-Polyaniline Matrix for Nitrate Detection. *J.*

Sensors **2019**, *2019*, doi:10.1155/2019/4257125.

97.   Mahmoud, A.M.; El-Wekil, M.M.; Mahnashi, M.H.; Ali, M.F.B.; Alkahtani, S.A. Modification of N,S Co-Doped Graphene Quantum Dots with p-Aminothiophenol-Functionalized Gold Nanoparticles for Molecular Imprint-Based Voltammetric Determination of the Antiviral Drug Sofosbuvir. *Microchim. Acta* **2019**, *186*, doi:10.1007/s00604-019-3647-7.

98.   Blinova, N. V.; Stejskal, J.; Trchová, M.; Prokeš, J.; Omastová, M. Polyaniline and Polypyrrole: A Comparative Study of the Preparation. *Eur. Polym. J.* **2007**, *43*, 2331–2341, doi:10.1016/j.eurpolymj.2007.03.045.

99.   Hassan, S.S.M.; Kamel, A.H.; Fathy, M.A. A Novel Screen-Printed Potentiometric Electrode with Carbon Nanotubes/Polyaniline Transducer and Molecularly Imprinted Polymer for the Determination of Nalbuphine in Pharmaceuticals and Biological Fluids. *Anal. Chim. Acta* **2022**, *1227*, doi:10.1016/j.aca.2022.340239.

100.   Lee, S.P. Terpene Sensor Array with Bridge-Type Resistors by CMOS Technology. In Proceedings of the IOP Conference Series: Materials Science and Engineering; Institute of Physics Publishing, July 16 2015; Vol. 87.

101.   Koudehi, M.F.; Pourmortazavi, S.M. Polyvinyl Alcohol/Polypyrrole/Molecularly Imprinted Polymer Nanocomposite as Highly Selective Chemiresistor Sensor for 2,4-DNT Vapor Recognition. *Electroanalysis* **2018**, *30*, 2302–2310, doi:10.1002/elan.201700751.

102.   Tremel, K.; Ludwigs, S. *P3HT Revisited – From Molecular Scale to Solar Cell Devices*; Ludwigs, S., Ed.; Springer, 2014; Vol. 265; ISBN 978-3-662-45144-1.

103.   Meresa, A.A.; Kim, F.S. Selective Ammonia-Sensing Platforms Based on a Solution-Processed Film of Poly(3-Hexylthiophene) and p-Doping Tris(Pentafluorophenyl)Borane. *Polymers (Basel).* **2020**, *12*, doi:10.3390/polym12010128.

104.   Han, S.; Zhuang, X.; Shi, W.; Yang, X.; Li, L.; Yu, J. Poly(3-Hexylthiophene)/Polystyrene (P3HT/PS) Blends Based Organic Field-Effect Transistor Ammonia Gas Sensor. *Sensors Actuators, B Chem.* **2016**, *225*, 10–15, doi:10.1016/j.snb.2015.11.005.

105.   Mun, S.; Park, Y.; Lee, Y.-E.K.; Sung, M.M. Highly Sensitive Ammonia Gas Sensor Based on Single-

Crystal Poly(3-Hexylthiophene) (P3HT) Organic Field Effect Transistor. *Langmuir* **2017**, *33*, 13554–13560, doi:10.1021/acs.langmuir.7b02466.

106. Tiwari, S.; Singh, A.K.; Joshi, L.; Chakrabarti, P.; Takashima, W.; Kaneto, K.; Prakash, R. Poly-3-Hexylthiophene Based Organic Field-Effect Transistor: Detection of Low Concentration of Ammonia. *Sensors Actuators, B Chem.* **2012**, *171–172*, 962–968, doi:10.1016/j.snb.2012.06.010.

107. Ayankojo, A.G.; Reut, J.; Öpik, A.; Syritski, V. Sulfamethizole-Imprinted Polymer on Screen-Printed Electrodes: Towards the Design of a Portable Environmental Sensor. *Sensors Actuators, B Chem.* **2020**, *320*, doi:10.1016/j.snb.2020.128600.

108. Leibl, N.; Haupt, K.; Gonzato, C.; Duma, L. Molecularly Imprinted Polymers for Chemical Sensing: A Tutorial Review. *Chemosensors* **2021**, *9*, 1–19, doi:10.3390/chemosensors9060123.

109. Ratautaite, V.; Brazys, E.; Ramanaviciene, A.; Ramanavicius, A. Electrochemical Sensors Based on L-Tryptophan Molecularly Imprinted Polypyrrole and Polyaniline. *J. Electroanal. Chem.* **2022**, *917*, doi:10.1016/j.jelechem.2022.116389.

110. Silva, B.V.M.; Rodríguez, B.A.G.; Sales, G.F.; Sotomayor, M.D.P.T.; Dutra, R.F. An Ultrasensitive Human Cardiac Troponin T Graphene Screen-Printed Electrode Based on Electropolymerized-Molecularly Imprinted Conducting Polymer. *Biosens. Bioelectron.* **2016**, *77*, 978–985, doi:10.1016/j.bios.2015.10.068.

111. Ayerdurai, V.; Cieplak, M.; Noworyta, K.R.; Gajda, M.; Ziminska, A.; Sosnowska, M.; Piechowska, J.; Borowicz, P.; Lisowski, W.; Shao, S.; et al. Electrochemical Sensor for Selective Tyramine Determination, Amplified by a Molecularly Imprinted Polymer Film. *Bioelectrochemistry* **2021**, *138*, doi:10.1016/j.bioelechem.2020.107695.

112. Lee, M.H.; Thomas, J.L.; Liu, W.C.; Zhang, Z.X.; Liu, B. Da; Yang, C.H.; Lin, H.Y. A Multichannel System Integrating Molecularly Imprinted Conductive Polymers for Ultrasensitive Voltammetric Determination of Four Steroid Hormones in Urine. *Microchim. Acta* **2019**, *186*, doi:10.1007/s00604-019-3797-7.

113. Lee, M.H.; Thomas, J.L.; Su, Z.L.; Zhang, Z.X.; Lin, C.Y.; Huang, Y. Sen; Yang, C.H.; Lin, H.Y. Doping of Transition Metal Dichalcogenides in Molecularly Imprinted Conductive Polymers for the

Ultrasensitive Determination of 17β-Estradiol in Eel Serum. *Biosens. Bioelectron.* **2020**, *150*, doi:10.1016/j.bios.2019.111901.

114.   Lee, M.H.; Lin, C.C.; Kutner, W.; Thomas, J.L.; Lin, C.Y.; Iskierko, Z.; Ku, Y.S.; Lin, C.Y.; Borowicz, P.; Sharma, P.S.; et al. Peptide-Imprinted Conductive Polymer on Continuous Monolayer Molybdenum Disulfide Transferred Electrodes for Electrochemical Sensing of Matrix Metalloproteinase-1 in Lung Cancer Culture Medium. *Biosens. Bioelectron. X* **2023**, *13*, doi:10.1016/j.biosx.2022.100258.

115.   Costa, R.; Costa, J.; Moreira, P.; Brandão, A.T.S.C.; Mafra, I.; Silva, A.F.; Pereira, C.M. Molecularly Imprinted Polymer as a Synthetic Antibody for the Biorecognition of Hazelnut Cor a 14-Allergen. *Anal. Chim. Acta* **2022**, *1191*, doi:10.1016/j.aca.2021.339310.

116.   Moro, G.; Bottari, F.; Sleegers, N.; Florea, A.; Cowen, T.; Moretto, L.M.; Piletsky, S.; De Wael, K. Conductive Imprinted Polymers for the Direct Electrochemical Detection of B-Lactam Antibiotics: The Case of Cefquinome. *Sensors Actuators, B Chem.* **2019**, *297*, 126786, doi:10.1016/j.snb.2019.126786.

117.   Wardani, N.I.; Kangkamano, T.; Wannapob, R.; Kanatharana, P.; Thavarungkul, P.; Limbut, W. Electrochemical Sensor Based on Molecularly Imprinted Polymer Cryogel and Multiwalled Carbon Nanotubes for Direct Insulin Detection. *Talanta* **2023**, *254*, doi:10.1016/j.talanta.2022.124137.

118.   Mazzotta, E.; Malitesta, C.; Surdo, S.; Barillaro, G. Microstructuring Conducting Polymers and Molecularly Imprinted Polymers by Light-Activated Electropolymerization on Micromachined Silicon. Applications in Electrochemical Sensing. *Proc. IEEE Sensors* **2013**, doi:10.1109/ICSENS.2013.6688482.

119.   Turco, A.; Corvaglia, S.; Mazzotta, E. Electrochemical Sensor for Sulfadimethoxine Based on Molecularly Imprinted Polypyrrole: Study of Imprinting Parameters. *Biosens. Bioelectron.* **2015**, *63*, 240–247, doi:10.1016/j.bios.2014.07.045.

120.   Ramanaviciene, A.; Ramanavicius, A. Molecularly Imprinted Polypyrrole-Based Synthetic Receptor for Direct Detection of Bovine Leukemia Virus Glycoproteins. *Biosens. Bioelectron.* **2004**, *20*, 1076–1082, doi:10.1016/j.bios.2004.05.014.

121. Lowdon, J.W.; Diliën, H.; Singla, P.; Peeters, M.; Cleij, T.J.; van Grinsven, B.; Eersels, K. MIPs for Commercial Application in Low-Cost Sensors and Assays – An Overview of the Current Status Quo. *Sensors Actuators, B Chem.* **2020**, *325*, doi:10.1016/j.snb.2020.128973.

122. Chuang, S.W.; Rick, J.; Chou, T.C. Electrochemical Characterisation of a Conductive Polymer Molecularly Imprinted with an Amadori Compound. *Biosens. Bioelectron.* **2009**, *24*, 3170–3173, doi:10.1016/j.bios.2009.02.033.

123. Cieplak, M.; Szwabinska, K.; Sosnowska, M.; Chandra, B.K.C.; Borowicz, P.; Noworyta, K.; D'Souza, F.; Kutner, W. Selective Electrochemical Sensing of Human Serum Albumin by Semi-Covalent Molecular Imprinting. *Biosens. Bioelectron.* **2015**, *74*, 960–966, doi:10.1016/j.bios.2015.07.061.

124. Lach, P.; Cieplak, M.; Majewska, M.; Noworyta, K.R.; Sharma, P.S.; Kutner, W. "gate Effect" in p-Synephrine Electrochemical Sensing with a Molecularly Imprinted Polymer and Redox Probes. *Anal. Chem.* **2019**, *91*, 7546–7553, doi:10.1021/acs.analchem.8b05512.

125. Sharma, P.S.; Iskierko, Z.; Noworyta, K.; Cieplak, M.; Borowicz, P.; Lisowski, W.; D'Souza, F.; Kutner, W. Synthesis and Application of a "Plastic Antibody" in Electrochemical Microfluidic Platform for Oxytocin Determination. *Biosens. Bioelectron.* **2018**, *100*, 251–258, doi:10.1016/j.bios.2017.09.009.

126. Jahangiri-Manesh, A.; Mousazadeh, M.; Nikkhah, M. Fabrication of Chemiresistive Nanosensor Using Molecularly Imprinted Polymers for Acetone Detection in Gaseous State. *Iran. Polym. J. (English Ed.* **2022**, *31*, 883–891, doi:10.1007/s13726-022-01044-w.

127. Matsuguchi, M.; Uno, T. Molecular Imprinting Strategy for Solvent Molecules and Its Application for QCM-Based VOC Vapor Sensing. *Sensors Actuators, B Chem.* **2006**, *113*, 94–99, doi:10.1016/j.snb.2005.02.028.

128. Jahangiri-Manesh, A.; Mousazadeh, M.; Nikkhah, M.; Abbasian, S.; Moshaii, A.; Masroor, M.J.; Norouzi, P. Molecularly Imprinted Polymer-Based Chemiresistive Sensor for Detection of Nonanal as a Cancer Related Biomarker. *Microchem. J.* **2022**, *173*, doi:10.1016/j.microc.2021.106988.

129. Hua, Y.; Ahmadi, Y.; Kim, K.H. Molecularly Imprinted Polymers for Sensing Gaseous Volatile Organic Compounds: Opportunities and Challenges. *Environ. Pollut.* **2022**, *311*, 119931,

doi:10.1016/j.envpol.2022.119931.

130. Vale, A. Isopropanol. *Medicine (Baltimore).* **2007**, *35*, 626, doi:10.1016/j.mpmed.2007.09.002.

131. Deng, C.; Li, N.; Zhang, X. Development of Headspace Solid-Phase Microextraction with on-Fiber Derivatization for Determination of Hexanal and Heptanal in Human Blood. *J. Chromatogr. B Anal. Technol. Biomed. Life Sci.* **2004**, *813*, 47–52, doi:10.1016/j.jchromb.2004.09.007.

132. Li, N.; Deng, C.; Yin, X.; Yao, N.; Shen, X.; Zhang, X. Gas Chromatography-Mass Spectrometric Analysis of Hexanal and Heptanal in Human Blood by Headspace Single-Drop Microextraction with Droplet Derivatization. *Anal. Biochem.* **2005**, *342*, 318–326, doi:10.1016/j.ab.2005.04.024.

133. Api, A.M.; Belsito, D.; Botelho, D.; Bruze, M.; Burton, G.A.; Buschmann, J.; Dagli, M.L.; Date, M.; Dekant, W.; Deodhar, C.; et al. RIFM Fragrance Ingredient Safety Assessment, Acetophenone, CAS Registry Number 98-86-2. *Food Chem. Toxicol.* **2018**, *118*, S162–S169, doi:10.1016/j.fct.2018.06.050.

134. Merckel, C.; Pragst, F.; Ratzinger, A.; Aebi, B.; Bernhard, W.; Sporkert, F. Application of Headspace Solid Phase Microextraction to Qualitative and Quantitative Analysis of Tobacco Additives in Cigarettes. *J. Chromatogr. A* **2006**, *1116*, 10–19, doi:10.1016/j.chroma.2006.03.010.

135. Kharlampidi, K.E.; Nurmurodov, T.S.; Ulitin, N. V.; Tereshchenko, A.; Miroshkin, N.P.; Shiyan, D.A.; Novikov, N.A.; Stoyanov, O. V.; Ziyatdinov, N.N.; Lapteva, T. V.; et al. Design of Cumene Oxidation Process. *Chem. Eng. Process. - Process Intensif.* **2021**, *161*, 108314, doi:10.1016/j.cep.2021.108314.

136. Qi, J.; Ma, H.; Li, X.; Zhou, Z.; Choi, M.C.K.; C, A.S. Synthesis and Characterization of Cobalt (III) Complexes Containing 2-Pyridinecarboxamide Ligands and Their Application in Catalytic Oxidation of Ethylbenzene with Dioxygen † Four Novel Cobalt (III) Complexes Were Found to Have High Catalytic Activiti. *Change* **2003**, 1294–1295.

137. Li, G.; Li, Y.; Mu, R.; Xu, Y.; Dong, P. Direct Side-Chain Oxidation of Ethylbenzene over Supported Co 4HP2Mo15V3O62 Catalysts as a Clean and Highly Efficient Approach to Producing Acetophenone. *React. Kinet. Mech. Catal.* **2013**, *109*, 199–212, doi:10.1007/s11144-013-0555-4.

138. Liu, T.; Cheng, H.; Sun, L.; Liang, F.; Zhang, C.; Ying, Z.; Lin, W.; Zhao, F. Synthesis of Acetophenone

from Aerobic Catalytic Oxidation of Ethylbenzene over Ti-Zr-Co Alloy Catalyst: Influence of Annealing Conditions. *Appl. Catal. A Gen.* **2016**, *512*, 9–14, doi:10.1016/j.apcata.2015.12.008.

139. Klzllcan, N.; Akar, A. Modification of Acetophenone-Formaldehyde and Cyclohexanone-Formaldehyde Resins.

140. Siddiqi, I.; Pitre, K.S. Determination of Phenones in a Perfume Composition. *Rev. Anal. Chem.* **2003**, *22*, 9–17, doi:10.1515/REVAC.2003.22.1.9.

141. Hałdys, K.; Goldeman, W.; Anger-Góra, N.; Rossowska, J.; Latajka, R. Monosubstituted Acetophenone Thiosemicarbazones as Potent Inhibitors of Tyrosinase: Synthesis, Inhibitory Studies, and Molecular Docking. *Pharmaceuticals* **2021**, *14*, 1–17, doi:10.3390/ph14010074.

142. Climent, M.J.; Corma, A.; Iborra, S.; Velty, A. Activated Hydrotalcites as Catalysts for the Synthesis of Chalcones of Pharmaceutical Interest. *J. Catal.* **2004**, *221*, 474–482, doi:10.1016/j.jcat.2003.09.012.

143. Copeland, C.L.; Kitching, E.H. Cases Illustrating the Sedative Effects of Aceto-Phenone (Hypnone.). *J. Ment. Sci.* **1887**, *32*, 519–525, doi:doi:10.1192/bjp.32.140.519.

144. Corradi, M.; Gergelova, P.; Mutti, A. Exhaled Volatile Organic Compounds in Nonrespiratory Diseases. *Exhaled Biomarkers* **2010**, 140–151, doi:10.1183/1025448x.00018809.

145. Li, J.; Peng, Y.; Duan, Y. Diagnosis of Breast Cancer Based on Breath Analysis: An Emerging Method. *Crit. Rev. Oncol. Hematol.* **2013**, *87*, 28–40, doi:10.1016/j.critrevonc.2012.11.007.

146. Berg, W.A.; Gutierrez, L.; NessAiver, M.S.; Carter, W.B.; Bhargavan, M.; Lewis, R.S.; Ioffe, O.B. Diagnostic Accuracy of Mammography, Clinical Examination, US, and MR Imaging in Preoperative Assessment of Breast Cancer. *Radiology* **2004**, *233*, 830–849, doi:10.1148/radiol.2333031484.

147. Maruvada, P.; Wang, W.; Wagner, P.D.; Srivastava, S. Biomarkers in Molecular Medicine: Cancer Detection and Diagnosis. *Biotechniques* **2005**, *38*, 7–32.

148. Hietanen, E.; Bartsch, H.; Béréziat, J.C.; Camus, A.M.; McClinton, S.; Eremin, O.; Davidson, L.; Boyle, P. Diet and Oxidative Stress in Breast, Colon and Prostate Cancer Patients: A Case-Control Study. *Eur. J. Clin. Nutr.* **1994**, *48*, 575–586.

149. Phillips, M.; Cataneo, R.N.; Ditkoff, B.A.; Fisher, P.; Greenberg, J.; Gunawardena, R.; Kwon, C.S.; Rahbari-Oskoui, F.; Wong, C. Volatile Markers of Breast Cancer in the Breath. *Breast J.* **2003**, *9*, 184–191, doi:10.1046/j.1524-4741.2003.09309.x.

150. Sun, X.; Shao, K.; Wang, T. Detection of Volatile Organic Compounds (VOCs) from Exhaled Breath as Noninvasive Methods for Cancer Diagnosis Young Investigators in Analytical and Bioanalytical Science. *Anal. Bioanal. Chem.* **2016**, *408*, 2759–2780, doi:10.1007/s00216-015-9200-6.

151. Sroysee, W.; Chunta, S.; Amatatongchai, M.; Lieberzeit, P.A. Molecularly Imprinted Polymers to Detect Profenofos and Carbofuran Selectively with QCM Sensors. *Phys. Med.* **2019**, *7*, 100016, doi:10.1016/j.phmed.2019.100016.

152. Hawari, H.F.; Samsudin, N.M.; Ahmad, M.N.; Shakaff, A.Y.M.; Ghani, S.A.; Wahab, Y.; Za'aba, S.K.; Akitsu, T. Array of MIP-Based Sensor for Fruit Maturity Assessment. *Procedia Chem.* **2012**, *6*, 100–109, doi:10.1016/j.proche.2012.10.135.

Scientific Contributions

Publications related to molecular imprinting:

Julia Völkle, Katarina Kumpf, <u>Adriana Feldner</u>, Peter Lieberzeit and Philipp Fruhmann, Development of conductive molecularly imprinted polymers (cMIPs) for limonene to improve and interconnect QCM and chemiresistor sensing, *Sensors and Actuators B: Chemical*, **2022**

DOI: https://doi.org/10.1016/j.snb.2021.131293

<u>Adriana Feldner</u>, Julia Völkle, Peter Lieberzeit and Philipp Fruhmann, Conductive Molecularly Imprinted Polymers (cMIPs): Rising and Versatile Key Elements in Chemical Sensing, *Chemosensors*, **2023**

DOI: https://doi.org/10.3390/chemosensors11050299

<u>Adriana Feldner</u>, Julia Völkle, Felix Thier and Peter Lieberzeit, Biological, Bio-Derived, and Biomimetic Receptors in Mass-Sensitive Sensing. In: Springer Series on Chemical Sensors and Biosensors, *Springer Series on Chemical Sensors and Biosensors*, **2023**

DOI: https://doi.org/10.1007/5346

Parts of the thesis were presented at the following conferences:

<u>Adriana Feldner</u>, Peter Lieberzeit and Philipp Fruhmann, Development of conductive MIP blends for heptanal vapour detection, 1st Conference of Applied Surface Chemistry, **2022**, Wiener Neustadt, Austria

<u>Adriana Feldner</u>, Peter Lieberzeit and Philipp Fruhmann, Development of conductive MIP blends for heptanal vapour detection, Retreat of the Doctoral School in Chemistry (Panel A), **2022**, Bad Waltersdorf, Austria

<u>Adriana Feldner</u>, Peter Lieberzeit and Philipp Fruhmann, Development of conductive MIP blends for heptanal vapour detection, Matrafured – International Meeting on Chemical Sensors, **2022**, Visegrad, Hungary

Adriana Feldner, Vincent Nussbaumer, Gregor Zimmermann, Peter Lieberzeit and Philipp Fruhmann, Conductive Molecularly Imprinted Polymer (cMIP) Blends for VOC Sensing, Retreat of the Doctoral School in Chemistry (Panel A), **2023**, Zeillern, Austria

Adriana Feldner, Vincent Nussbaumer, Peter Lieberzeit and Philipp Fruhmann, Development of Conductive Molecularly Imprinted Polymer (cMIP) Blends for VOC Sensing, ANAKON, **2023**, Vienna, Austria

Adriana Feldner, Vincent Nussbaumer, Peter Lieberzeit and Philipp Fruhmann, cMIPs-based sensors for isopropanol and heptanal detection, 2nd Conference of Applied Surface Chemistry, **2023**, Vienna, Austria

Adriana Feldner, Vincent Nussbaumer, Peter Lieberzeit and Philipp Fruhmann, Development of Conductive Molecularly Imprinted Polymer Blends for VOC Sensing, Sensor and Measurement Science International Conference, **2023**, Nürnberg, Germany

Adriana Feldner, Marco Berchtel, Peter Lieberzeit and Philipp Fruhmann, Acetophenone Sensing via Conductive Molecularly Imprinted Polymer (cMIP) Blends, Symposium of the Doctoral School in Chemistry, **2023**, Vienna, Austria

Adriana Feldner, Vincent Nussbaumer, Gregor Zimmermann, Peter Lieberzeit and Philipp Fruhmann, Gas Sensing via Conductive Molecularly Imprinted Polymers (cMIPs) , AVS69, **2023**, Portland, Oregon, USA